AFRL-VA-WP-TR-2002-3049

PREDICTION AND CONTROL OF TWIN-TAIL BUFFET OF FIGHTER AIRCRAFT

Essam F. Sheta

CFD Research Corporation
215 Wynn Drive
Huntsville, AL 35805

MARCH 2002

Final Report for 01 June 2000 – 01 March 2002

This is a Small Business Innovation Research (SBIR) Phase II Report.

AIR VEHICLES DIRECTORATE
AIR FORCE MATERIEL COMMAND
AIR FORCE RESEARCH LABORATORY
WRIGHT-PATTERSON AIR FORCE BASE, OH 45433-7542

NOTICE

USING GOVERNMENT DRAWINGS, SPECIFICATIONS, OR OTHER DATA INCLUDED IN THIS DOCUMENT FOR ANY PURPOSE OTHER THAN GOVERNMENT PROCUREMENT DOES NOT IN ANY WAY OBLIGATE THE U.S. GOVERNMENT. THE FACT THAT THE GOVERNMENT FORMULATED OR SUPPLIED THE DRAWINGS, SPECIFICATIONS, OR OTHER DATA DOES NOT LICENSE THE HOLDER OR ANY OTHER PERSON OR CORPORATION; OR CONVEY ANY RIGHTS OR PERMISSION TO MANUFACTURE, USE, OR SELL ANY PATENTED INVENTION THAT MAY RELATE TO THEM.

THIS REPORT IS RELEASABLE TO THE NATIONAL TECHNICAL INFORMATION SERVICE (NTIS). AT NTIS, IT WILL BE AVAILABLE TO THE GENERAL PUBLIC, INCLUDING FOREIGN NATIONS.

THIS TECHNICAL REPORT HAS BEEN REVIEWED AND IS APPROVED FOR PUBLICATION.

L J Huttsell

L.J. HUTTSELL
Senior Aerospace Engineer
Structural Design & Development Branch

Terry M. Harris

TERRY M. HARRIS, Chief
Structural Design and Development Branch
Structures Division

for 2

DAVID M. PRATT, Technical Advisor
Structures Division
Air Vehicles Directorate

Do not return copies of this report unless contractual obligations or notice on a specific document require its return.

REPORT DOCUMENTATION PAGE

Form Approved
OMB No. 0704-0188

1. REPORT DATE *(DD-MM-YY)*	2. REPORT TYPE	3. DATES COVERED *(From - To)*
March 2002	Final	06/01/2000 – 03/01/2002

4. TITLE AND SUBTITLE
Prediction and Control of Twin-Tail Buffet of Fighter Aircraft

5a. CONTRACT NUMBER
F33615-00-C-3010

5b. GRANT NUMBER

5c. PROGRAM ELEMENT NUMBER
65502F

6. AUTHOR(S)
Essam F. Sheta

5d. PROJECT NUMBER
3005

5e. TASK NUMBER
41

5f. WORK UNIT NUMBER
AB

7. PERFORMING ORGANIZATION NAME(S) AND ADDRESS(ES)
CFD Research Corporation
215 Wynn Drive
Huntsville, AL 35805

8. PERFORMING ORGANIZATION REPORT NUMBER
8212/7

9. SPONSORING/MONITORING AGENCY NAME(S) AND ADDRESS(ES)
Air Vehicles Directorate
Air Force Research Laboratory
Air Force Materiel Command
Wright-Patterson Air Force Base, OH 45433-7542

10. SPONSORING/MONITORING AGENCY ACRONYM(S)
AFRL/VASD

11. SPONSORING/MONITORING AGENCY REPORT NUMBER(S)
AFRL-VA-WP-TR-2002-3049

12. DISTRIBUTION/AVAILABILITY STATEMENT
Approved for public release; distribution is unlimited.

13. SUPPLEMENTARY NOTES
This is a Small Business Innovation Research (SBIR) Phase II Report. Report contains color.

14. ABSTRACT

High-fidelity multidisciplinary analysis capabilities for the prediction and control of tail buffeting of fighter aircraft have been developed and extensively validated for the F/A-18 aircraft. The computational results compared very well with flight and several experimental data. The results indicated that the vertical tail is subject to both bending and torsional responses, mainly in the first mode. The buffet excitation peaks shift to lower frequency as the angle of attack increases. Capabilities for buffet alleviation have been demonstrated using LEX fences and vortical blowing. A parametric study for both the active and passive flow control has been conducted. Capabilities for actively controlling the vertical tail structure have been demonstrated by strengthening the F/A-18 vertical tail using piezoelectric actuators.

15. SUBJECT TERMS
tail buffeting, fluid-structure interaction, flow control, structure control, smart materials, multidisciplinary analysis, MDICE, unsteady aerodynamics, aeroelasticity, SBIR Report

16. SECURITY CLASSIFICATION OF:			17. LIMITATION OF ABSTRACT:	18. NUMBER OF PAGES	19a. NAME OF RESPONSIBLE PERSON (Monitor)
a. REPORT	b. ABSTRACT	c. THIS PAGE			Larry Huttsell
Unclassified	Unclassified	Unclassified	SAR	80	19b. TELEPHONE NUMBER *(Include Area Code)* (937) 255-8456

HES&S 31-15093-1

Standard Form 298 (Rev. 8-98)
Prescribed by ANSI Std. Z39-18

TABLE OF CONTENTS

Section **Page**

TABLE OF CONTENT S (concluded)

Section **Page**

LIST OF FIGURES

Figure **Page**

LIST OF FIGURES (concluded)

Figure **Page**

LIST OF TABLES

PREFACE

This is the final report for the Air Force Research Laboratory (AFRL) SBIR Phase II study entitled, "Prediction and Control of Twin-Tail Buffet of Fighter Aircraft." This project was sponsored by AFRL/VASD (Contract Number: F33615-00-C-3010) and conducted by CFD Research Corporation (CFDRC). The AFRL technical monitor for this contract was Mr. Lawrence J. Huttsell. The project manager was Dr. Vincent J. Harrand of CFD Research Corporation. The principal investigator was Dr. Essam F. Sheta of CFD Research Corporation.

ACKNOWLEDGEMENTS

The author of this report would like to thank the technical monitor Mr. Lawrence J. Huttsell for his valuable participation and discussions regarding the content and direction of the Phase II effort. The author would like to thank Dr. Robert W. Moses of NASA Langley Research Center for his valuable input and feedback regarding the control law for the buffet alleviation. The author would like also to thank Dr. Vincent J. Harrand for his understanding, support and enthusiastic participation during the course of this project. The efforts of Dr. Viji Parthasarathy and Dr. Mark Underwood were very valuable. The author would like also to thank Ms. Denise Rynders for her efforts in preparing various manuscripts, including this report, during the course of this project.

NOMENCLATURE

A_t	Reference area of vertical tail, 4.842 m^2.
$\overline{C}$	Mean aerodynamic chord of the wing, 3.5 *m*.
C_P	Coefficient of pressure, $(P - P_\infty)/q_\infty$
$\overline{C_P}$	Mean pressure coefficient, $\left[\frac{1}{N}\sum_1^N C_P\right]$
$\hat{C}_P$	RMS pressure coefficient, $\left[\frac{1}{N}\sum_1^N \left(C_P - \overline{C}_P\right)^2\right]^{1/2}$
C_{rbm}	Root bending moment coefficient, $\frac{M_B}{q_\infty A_t \overline{C}}$
F(n)	Dimensionless buffet pressure power spectral density
FS	Fuselage station
f	Frequency, *Hz*
M_B	Vertical tail root bending moment
N	Number of sample points
n	Nondimensional frequency, $f \times \overline{C} / U_\infty$
P_i	Pressure on inboard tail surface
P_o	Pressure on outboard tail surface
ΔP	Differential pressure, P_i - P_o
q_∞	Freestream dynamic pressure, $\frac{1}{2} r_\infty U_\infty^2$
U_∞	Freestream velocity
α	Angle of attack

LIST OF ACRONYMS

ACRONYM	DESCRIPTION
ACROBAT	Active Control Responses of Buffet Affected Tails
AFC	Active Fiber Composites
AFRL	Air Force Research Laboratory
ALPHA	Angle of Attack
CCW	Counter Clockwise
CFD	Computational Fluid Dynamics
CFDRC	CFD Research Corporation
CSD	Computational Structure Dynamics
FS	Fuselage Station
GUI	Graphical User Interface
HARV	High Alpha Research Vehicle
JSF	Joint Strike Fighter
LEX	Leading-edge Extension
MDICE	MultiDIsciplinary Computing Environment
PSD	Power Spectral Density
PZT	Piezoelectric
RBM	Root Bending Moment
RMS	Root-Mean-Square
TCB	Tangential Centerline Blowing
TFI	Transfinite Interpolation
TSB	Tangential Spanwise Blowing
TVB	Tangential Vortex Blowing

1. SUMMARY

The overall objective of this project was to develop multidisciplinary analysis capabilities for the prediction and control of twin-tail buffet and related aeroelastic problems of fighter aircraft. The Phase I study demonstrated the feasibility of the multidisciplinary computing environment (MDICE) approach for the prediction of twin-tail buffet of generic fighter aircraft.

In Phase II, the high-fidelity multidisciplinary capabilities, including MDICE-compliant modules for the aerodynamics, structure dynamics, electrodynamics of smart materials, and control characteristics for buffet alleviation of fighter aircraft have been successfully developed. The basic (uncontrolled) multidisciplinary aeroelastic problem is solved using four sets of analysis modules. The aerodynamic flow field around the F/A-18 aircraft is computed using the Reynolds-averaged full Navier-Stokes equations. The structure dynamics response of the vertical tail is predicted using direct finite-element analysis. The interface between the fluid and structure is applied using conservative/consistent interfacing methodology. The motion of the computational grid due to the deflection of the vertical tail is computed using a transfinite interpolation (TFI) module. Prediction and validation of the vertical tail buffet responses of full F/A-18 aircraft are conducted at typical flight conditions. The F/A-18 aircraft is pitched at wide range of high angles of attack at a Mach number of 0.243 and a Reynolds number of 11×10^6. The computational results of several aeroelastic parameters compared well with flight and experimental data. The results indicated that the vertical tail is subject to both bending and torsional responses, mainly in the first mode. The pressure on the outboard surface of the vertical tail is less sensitive to the angle of attack than the pressure on the inboard surface. On the other hand, the inboard surface of the vertical tail has more significant contribution in the unsteadiness and severity of the buffet problem than the outboard surface. The buffet excitation peaks shift to lower frequency as the angle of attack increases.

Capabilities for vertical tail buffeting alleviation of fighter aircraft have been demonstrated using several flow control methods. Passive flow control using streamwise LEX fences and active flow control using vortical blowing have been applied to alleviate vertical tail buffeting of full F/A-18 aircraft. Flow control methods restructured the vortical flow over the aircraft and balanced the unsteady differential pressure across the vertical tail. A parametric study for both the active and passive flow control has been conducted, and is documented in this report.

Capabilities for actively controlling the vertical tail structure for buffeting alleviation have been developed and demonstrated by strengthening the F/A-18 vertical tail using piezoelectric actuators. Direct finite-element analysis of the piezoelectric actuators has been developed and integrated with MDICE. In addition, several control laws were developed and integrated with MDICE to drive the piezoelectric actuators. The control laws are based on a control law used at NASA Langley for F/A-18 buffet alleviation during the Active Control Responses of Buffet Affected Tails (ACROBAT) program. The piezoelectric actuators reduced the acceleration peaks by up to 12 percent in the first bending mode and up to 44 percent in the first torsion mode.

The results of this study are summarized in this report. The findings of the investigation and the lessons learned during this project are all discussed. A recommendation for future research toward a better design of high-performance fighter aircraft is outlined at the end of this report.

2. INTRODUCTION

2.1 Background Review

The strong vortical flow of fighter aircraft at high angles of attack contributes significantly to the aerodynamic and aeroelastic characteristics and maneuver capabilities of these aircraft. In fighter aircraft such as the F/A-18, the leading-edge extension (LEX) of the wing maintains lift at high angles of attack by generating a pair of vortices that trails downstream over the aircraft. The vortices entrain air over the vertical tails to maintain stability of the aircraft. However, at some flight conditions, the aircraft suffers severe aeroelastic problem when the leading-edge vortices break down ahead of the vertical tails. In these cases, the breakdown flow impinges upon the vertical tail surfaces, causing severe structural fatigue and premature failure. The buffet characteristics impose limits in addition to those defined by structural strength and stability requirements. The limiting factors may include vibration levels and frequencies at critical airframe locations where items like tracking radar antenna or a gyro might be located.

The vertical tail buffeting of fighter aircraft was the subject of numerous research works. A detailed overview of the buffet research work is given in the final report of Phase I of this project (Sheta, 2000a). The F/A-18 aircraft, in particular, was the subject of the most interesting buffet research (Wentz, 1987; Sellers et al., 1988; Lee and Brown, 1990; Cole et al., 1990; Bean and Lee, 1994;, and Moses and Pendleton, 1996). These experiments showed that the vortical flow breaks down ahead of the vertical tail at angles of attack of 25° and higher. At high angles of attack, the buffet pressure concentrates in a narrow, low frequency band. The buffet response occurs in the first bending mode, increases with increasing dynamic pressure and is larger at $M = 0.3$ than at higher Mach numbers. Buffet in the torsional mode occurred at lower angles of attack and at larger levels compared to the fundamental bending mode. Moses and Huttsell (2000) have shown that buffet characteristics of an early F-22 aircraft model are similar to what have been seen on the F/A-18 aircraft.

Computationally, there have been limited attempts to analyze the buffet problem successfully. Rizk et al. (1992a, 1992b) solved the Reynolds-averaged, thin-layer Navier-Stokes equations around the F/A-18 aircraft at $\alpha = 30^{o}$. A Chimera embedded grid consisting of 0.9 million cells was used to model the symmetric half of the aircraft. The aerodynamic results were qualitatively similar to some experimental data. Later, Gee et al. (1995) used 1.7 million cells to capture more robust vortices. A weak coupling between the aerodynamics and structures was considered by assuming rigid tails. Thus, the inertial effects of the acceleration of the tail points on the flow field were neglected. They concluded that the dominant frequency is very close to the first natural frequency of the tail. The time history shows a pattern of near periodic fluctuations of the loads. Kandil et al. (1996, 1997) analyzed the twin-tail buffet of a delta-wing/twin-tail model over wide range of angles of attack and spanwise locations of the tails. The results showed that the tail motion altered the vortex breakdown location and altered the unsteady buffet loads on the tails. The loads, deflections, and root bending moments were reduced as the twin tails moved laterally toward the vortex core. Sheta and Kandil (1998, 1999) studied the effects of pitching motion and rolling oscillations on the twin-tail buffet responses. The buffet loads and responses were shown to increase when the breakdown location moved upstream crossing the wing trailing

edge. Increasing the reduced frequency of rolling has led to higher loads and excitation peaks. However, the bending and torsion deflections were reduced.

A temporary solution to the buffet problem was achieved using passive streamwise LEX fences. The fences were fitted over the upper surface of the wing LEX to reconstruct the vortical flow over the aircraft (Shah, 1991). The fences, although developed through trial and error wind-tunnel experiments, reduces the buffet loads experienced by the vertical tails. In flight tests by Lee et al. (1994), the acceleration peaks at a point close to the tip of the vertical tail were reduced from 450 to 200 g with the addition of the LEX fence. However, a loss of 3 percent of maximum lift was monitored, since the fence disrupts the basic vortical flow. The fences were also less effective at high angles of attack. Rao et al. (1989) proposed an alternative method for passive control of tail buffeting. They used dorsal fin extension at the root of vertical tails. The dorsal fin had a highly swept leading edge for generating counter-rotating vortex in the outflow induced below LEX vortices. They observed a reconstructing of the post-breakdown flow before its encounter with the tail surface, resulting in alleviation in the tail buffet loads. However, the magnitude of lift loss due to the fin extension outweighs the effect of delayed vortex breakdown.

Other flow control methods focus on controlling the evolution of the vortical flow, onset of vortex breakdown, or the path of the vortices over the aircraft. Miller and Gile (1993) introduced a blowing jet at the 10 percent chord station over 60° and 76° sweep delta wings. Two blowing positions and directions were examined, tangential centerline blowing (TCB) and tangential vortex line blowing (TVB). In the centerline position, the jet blew tangentially along the model centerline. In the vortex position, the jet blew tangentially in a direction parallel to the leading-edge vortex. The investigation revealed that blowing parallel to the vortex core of the 60° sweep wing and blowing along the centerline of the 76° sweep wing at the highest rate provided the greatest improvement in the vortical flow and onset of vortex breakdown. Other experimental work, including Anglin and Satran (1980) and Seginer and Salomon (1986), has shown that blowing a discrete tangential spanwise jet (TSB) over the upper surface of a delta wing in a direction essentially parallel to the leading edge enhances the leading-edge vortex and delays vortex breakdown to higher angles of attack with substantial increase in lift. Anglin and Satran (1980) have investigated three positions of jet ports at 20, 30, and 40 percent chord stations. The investigation showed enhancement in vortex lift and increase in the maximum lift coefficient due to blowing. Sheta et al. (2000b) conducted numerical investigation on the effects of TCB, TVB, and TSB methods on the twin-tail buffet responses of generic fighter aircraft. The results of this work are also documented in the Phase I final report of this project. The results indicated that the TVB and TSB methods, that blow directly into the leading-edge vortices, have more potential than any other direction in controlling the buffet responses and in reformation of unburst vortices with larger length.

Since the buffet is a structural problem at its core, another way to control the problem is via structure control. Structure control can be accomplished in several ways: engineering a structure or material that is less susceptible to fatigue, using composites to create strain hardening tail, or using active structural control that uses piezoelectric patches for active stiffening or the use of active rudder. Although, the first two methods are simpler in the long run, initial tests of active buffet damping through the use of piezoelectrics have produced favorable results (Hauch et al. 1995). As part of the Actively Controlled Response of Buffet-Affected Tails (ACROBAT)

program, Moses (1998) conducted wind tunnel experiments on 1/6-scale F18 model. The starboard vertical tail was equipped with active rudder, and the port tail was equipped with piezoelectric actuators. The power spectral density (PSD) of the root bending moment at the frequency of the first bending mode was reduced by up to 60 percent.

2.2 Significance of the Current Research

The twin-tail buffet of fighter aircraft is one of the most persistent aeroelastic problems. The vertical tail-buffeting problem occurs with some of the most sophisticated and expensive aircraft in the U.S. arsenal. Millions of dollars are spent every year for inspection and repairs. For example, for the F/A-18 aircraft, some 200 special flight hours are needed for buffet checkup on the aircraft. A methodology that controls the twin-tail buffet problem and thereby reduces or eliminates premature fatigue failure in these aircraft will achieve a high level of commercial benefit. The capability to quickly and effectively demonstrate and compare proposed control methodologies is of vital importance to the design of new generation of fighter aircraft. The main objective of this proposal is to develop such a simulation capability and to validate the technology on the F/A-18 aircraft. With the successful completion of this effort, the aircraft wing/tails designs on a wide variety of existing and future air and space aircraft can be analyzed and optimized before the actual wind tunnel and flight tests occur. This may result in better designs and reduce testing costs.

2.3 Phase II Research Objectives

The overall objective of the project is to design and validate a computational analysis capability for the prediction and control of twin-tail buffet responses of modern fighter aircraft with application to the F/A-18 aircraft. The specific objectives of Phase II research effort are as follows:

1. Development and integration of an MDICE-compliant nonlinear finite-element module for the structure dynamics of flexible structures.
2. Prediction of F/A-18 vertical tail buffet responses over wide range of flight conditions.
3. Validation of the buffet results using flight and experimental data.
4. Passive flow control for F/A-18 tail buffet alleviation using streamwise LEX fences.
5. Active flow control for F/A-18 tail buffet alleviation using vortical blowing.
6. Development of direct finite-element implementation of the electrodynamic responses of the piezoelectric actuators.
7. Integration of the piezoelectric finite-element modeling into the MDICE environment.
8. Active structure control of the vertical tail buffeting using piezoelectric actuators.

The successful completion of the project should achieve the following three results:

1. Development of state-of-the-art multidisciplinary aeroelastic capability for the prediction of twin-tail buffet of fighter aircraft.
2. Provide capabilities for buffeting alleviation using active and passive flow control methods.
3. Provide capabilities for buffeting alleviation using active structure control and smart materials.

3. TECHNICAL APPROACH

3.1 Introduction

The buffet problem of fighter aircraft is a complex multidisciplinary aeroelastic phenomenon that involves strong interaction between several physical and numerical disciplines. The physical disciplines are the fluid dynamics of the massive vortical flow over the aircraft and the structure dynamics of the flexible bodies. The Reynolds-averaged full Navier-Stokes equation is solved for the aerodynamic flow field. The structure dynamics response of the vertical tail is solved using direct finite-element analysis. The numerical disciplines are the numerical interpolation between the fluid and structure interfaces and the grid motion due to the flexibility of the structure. The fluid-structure interfacing is modeled using conservative/consistent interfacing module. A transfinite interpolation (TFI) algorithm is used to deform the computational grid to accommodate the deformed shape of the vertical tail. The multidisciplinary modules used in the current study are integrated into the Multidisciplinary Computing Environment (MDICE). MDICE was developed by CFDRC in collaboration with the AFRL (Harrand et al., 2000). MDICE enables the analysis modules to run concurrently and cooperatively on a distributed network of computers to perform the multidisciplinary analysis. The particular sets of analysis modules used in the current investigation are outlined in the next few sections.

3.2 Computational Fluid Dynamics Module

The buffet problem of vertical tails occurs at high angles of attack where the flow field is characterized by strong vortical flow and massive three-dimensional flow separation. Therefore, the problem mandates the solution of the full Navier-Stokes equations to account for vorticity evolution, convection, shedding, vortex breakdown, and strong fluid-structure interactions. Euler and thin-layer Navier-Stokes equations can give an approximate solution in the region of primary vortices, but they cannot model the three-dimensional viscous effects or predict the accurate location and strength of the secondary and tertiary vortices.

In the current study, the flow field is solved using the conservation form of the unsteady, compressible, Reynolds-averaged full Navier-Stokes equations in time-dependent, body-conformed coordinates, x^I

$$\frac{\partial \hat{Q}}{\partial t} + \frac{\partial}{\partial x^i}\left[\hat{F}_i - (\hat{F}_v)_i\right] = 0, \qquad i = 1,2,3 \tag{1}$$

where $\hat{Q}$ is the vector of conservative variables, $\hat{F}$ and $\hat{F}_v$ are the inviscid flux and viscous flux vectors, respectively, and they are given by

$$\hat{Q} = \frac{1}{J}\begin{Bmatrix} r \\ ru_1 \\ ru_2 \\ ru_3 \\ re_t \end{Bmatrix} \tag{2}$$

$$\hat{F}_i = \frac{1}{J}\begin{Bmatrix} rU_i \\ ru_1U_i + \dfrac{\partial x^i}{\partial x_1}p \\ ru_2U_i + \dfrac{\partial x^i}{\partial x_2}p \\ ru_3U_i + \dfrac{\partial x^i}{\partial x_3}p \\ U_i(re_t + p) - \dfrac{\partial x^i}{\partial t}p \end{Bmatrix} \tag{3}$$

$$(\hat{F}_v)_i = \frac{1}{J}\begin{Bmatrix} 0 \\ \dfrac{\partial x^i}{\partial x_j}t_{1j} \\ \dfrac{\partial x^i}{\partial x_j}t_{2j} \\ \dfrac{\partial x^i}{\partial x_j}t_{3j} \\ \dfrac{\partial x^i}{\partial x_j}(u_k t_{kj} - q_j) \end{Bmatrix}, \tag{4}$$

where the density, pressure, energy per unit mass, velocity components, and Jacobean are denoted by r, p, e_t, u_i, and *J*, respectively. The contravariant velocity components are given by

$$U_i = \frac{\partial x^i}{\partial t} + \frac{\partial x^i}{\partial x_j}u_j \tag{5}$$

The shear stress components are given by

$$t_{mj} = \frac{mM_\infty}{\mathrm{Re}_\infty}\left[\frac{\partial x^i}{\partial x_j}\frac{\partial u_m}{\partial x^i} + \frac{\partial x^i}{\partial x_m}\frac{\partial u_j}{\partial x^i} - \frac{2}{3}d_{mj}\frac{\partial x^i}{\partial x_k}\frac{\partial u_k}{\partial x^i}\right] \tag{6}$$

The heat conduction components are given by

$$q_j = -\frac{mM_\infty}{\mathrm{Re}_\infty \mathrm{Pr}(g-1)}\frac{\partial x^i}{\partial x_j}\frac{\partial T}{\partial x^i}, \tag{7}$$

where m, T, Pr, and Re are the coefficient of dynamic viscosity, temperature, Prandtl number, and Reynolds number, respectively. The fluid dynamics governing equations are solved using an implicit finite-volume upwind scheme with Roe's flux-difference splitting for spatial differencing and fully implicit upwind scheme for temporal differencing.

In the finite-volume discretization, equation (1) is integrated in a control volume resulting in the integral form of the governing equations

$$\iiint_V \frac{\partial \hat{Q}}{\partial t} dV + \oiint_S (\hat{F} - \hat{F}_v) \cdot \hat{n} dS = 0 \tag{8}$$

The integral form of the equations is modified to account for the effect of moving volume (due to the flexibility of the vertical tails) as follows;

$$\iiint_V \frac{\partial \hat{Q}}{\partial t} dV + \oiint_S (\hat{F} - \hat{F}_v - \hat{Q}\vec{v}_g) \cdot \hat{n} dS = 0, \tag{9}$$

where $\vec{v}_g$ is the volume surface velocity, $\hat{n}$ is the normal to the volume surface, and *S* is the surface area. If the control volume *V* is fixed is space, then $\vec{v}_g = 0$. The solution method is integrated into the fluid dynamic module CFD-FASTRAN. CFD-FASTRAN has been validated for several complex moving body problems (Hall 1998).

3.3 Initial and Boundary Conditions

Initially, freestream conditions are assumed everywhere. The flow field characteristics are then computed assuming rigid configuration. The computations continue until the changes in the flow field become insignificant. The final solution is then used as the initial conditions for the flexible buffet problem.

The physical boundary conditions assume Riemann's inflow/outflow boundary conditions at the far field boundaries in all directions. On the aircraft surfaces, the no-slip and no-penetration conditions are enforced, that is, the relative velocity equals to zero. The normal pressure gradient equals to zero on stationary surfaces. On the accelerating tail surfaces, the normal pressure gradient is no longer zero due to the inertia of the moving tail. The pressure gradient on the accelerating surfaces becomes $\partial p / \partial \hat{n} = - r(\vec{a} \bullet \hat{n})$, where $\vec{a}$ is the acceleration of a point on the accelerating surface and $\hat{n}$ is the unit normal. This formula can be verified from the normal momentum equation. At the grid interface boundaries, the solution is interpolated across the boundaries using conservative interpolation. Conservative interpolation seeks to conserve the forces and moments between two adjacent cells. Because of the symmetry of the F/A-18 aircraft, only half of the aircraft is considered and a symmetry boundary condition is assumed at the symmetry boundary.

3.4 Computational Structure Dynamics Module

The structure dynamics response of the vertical tail is analyzed using direct finite-element analysis. The aeroelastic equations of motion of the vertical tail under the influence of the vortex breakdown flow are given by

$$[M]\{\ddot{Y}\}+[C]\{\dot{Y}\}+[K]\{Y\}=\{F\}, \tag{10}$$

where $\{Y\}$ is the displacement vector, $[M]$ is the mass matrix, $[C]$ is the damping matrix, $[K]$ is the stiffness matrix, and $\{F\}$ is the force vector due to the aerodynamic loads and shear stresses. The equations of motion of the vertical tails are solved using the finite-element stress code FEMSTRESS (CFD Research Corporation 1998). The vertical tail of the F/A-18 aircraft is modeled using second order quad shell elements and second-order hexahedral solid elements. The shell module uses the degenerated shell type element with eight nodal points to discretize the structure system. This element geometry is interpolated using the midsurface nodal point and midsurface nodal point normal. It is assumed that lines that are originally normal to the midsurface of the shell remain straight during the element deformation and that no transverse normal stress is developed. No structural damping is assumed in this study.

3.5 Fluid-Structure Interfacing Module

The fluid-structure interfacing algorithm is used to project the forces and moments from the fluid interface to the structure interface of the flexible body, and to feed back the aeroelastic deflections of the structure to the flow field. The interfacing is formulated in the most general sense for maximum flexibility. There are no inherent assumptions that the fluids grid is matched with the structure grid, either through different mesh densities, mesh architecture, or through physical separation between the interfaces as seen with thick shell finite-element models. The current simulation uses a conservative and consistent interface, adapted from Brown (1997). Conservative interfaces aim to conserve the forces and moments in the interpolation process between two grids. In this case, the sum of all forces and moments on the fluid interface is equivalent to the sum of all forces and moments on the structure interface:

$$\sum_{\substack{\text{fluid}\\ \text{faces}}} \vec{F}_{\text{fluid}} = \sum_{\substack{\text{solid}\\ \text{nodes}}} \vec{F}_{\text{solid}} \tag{11}$$

$$\sum_{\substack{\text{fluid}\\ \text{faces}}} \vec{M}_{\text{fluid}} = \sum_{\substack{\text{solid}\\ \text{nodes}}} \vec{M}_{\text{solid}} \quad . \tag{12}$$

Consistency (virtual work conservation) is also provided by requiring that the virtual work performed by the solid interface is equivalent to the virtual work performed by the fluid interface:

$$\sum_{\substack{\text{fluid}\\ \text{faces}}} W_{\text{fluid}} = \sum_{\substack{\text{solid}\\ \text{nodes}}} W_{\text{solid}} \tag{13}$$

$$W_{\text{fluid}} = \vec{F}_{\text{fluid}} \bullet \Delta\vec{r}_{\text{center}} \tag{14}$$

$$W_{\text{solid}} = \vec{F}_{\text{solid}} \bullet \Delta\vec{x} + \vec{M}_{\text{solid}} \bullet \vec{\omega}_{\text{solid}} \quad . \tag{15}$$

The above equations apply only to the degrees of freedom of the structure dynamics equations. MDICE environment contains many types of function-matching interfaces and conservative interfaces techniques. For more details, see Siegel et al. (1998).

3.6 Grid Motion Module

The computational grid is deformed every fluid-structure data transfer to accommodate the deformed shape of the tail. The six outer boundary surfaces of the deformed grid block are kept fixed. The grid is deformed using a transfinite interpolation (TFI) algorithm (Thompson 1998). The advantages of using TFI are that TFI is an interpolation procedure that deforms grids conforming to specified boundaries and it is very computationally efficient. The spacing between points in the physical domain is controlled by blending functions that specify how far into the original grid the effect of the new position of the flexible body surfaces is carried. The grid points on the surface of the tail are moving with the deflections of the tail. The deformation of the grid points decreases as you go far from the boundary in all directions, and vanishes at the outer boundary of the deformed block. The TFI routine is invoked automatically when a fluid-structure interface is exchanged between application modules.

3.7 Multidisciplinary Computing Environment

The multidisciplinary modules used in the current investigation are integrated into the Multidisciplinary Computing Environment (MDICE) (Kingsley et al. 1998). MDICE is a distributed, object-oriented environment for parallel execution of multidisciplinary modules. There are many advantages to the MDICE approach. Using MDICE, one can avoid giant monolithic codes that attempt to provide all modules in a single large computer program. Such large programs are difficult to develop and maintain, and by their nature, cannot contain up-to-date technology. The MDICE allows the reuse of existing, state-of-the-art codes that have been validated. The flexibility of exchanging application programs enables the selection of technology best suited to the task at hand. Efficiency is achieved by utilizing a parallel-distributed network of computers. Extensibility is provided by allowing additional engineering programs and disciplines to be added without modifying or breaking the modules or disciplines already in the environment.

The first component in MDICE is a central controlling process that provides network and application control, serves as an object repository, carries out remote procedure calls, and coordinates the execution of the several application programs via MDICE-specific script language. The second component is a collection of libraries, each containing a set of functions callable by the application programs. These libraries provide low-level communication and control functions that are hidden from the application programs, as well as more visible functionality, such as object creation and manipulation, interpolation of flow data along interfaces, and safe dynamic memory allocation services. Finally, the environment also encompasses a comprehensive set of MDICE compliant application programs. MDICE provides capabilities for parallel execution of participating application programs and has a full interface for those codes written in Fortran 77 or 90, C, or C++.

The MDICE graphical user interface (GUI) includes facilities for controlling the execution of a multidisciplinary application. A module for each discipline is selected; for each module, the computer on which the program is to be run is chosen. Other information is provided, such as specifying a directory to run each module and any command line arguments that the module might require. Once the simulation has been set up, the user then executes a short script in the GUI that explicitly specifies the synchronization between the modules. The MDICE script contains all of the conveniences found in most common script languages. In addition, MDICE script supports remote procedure calls and parallel execution of the application modules. These remote procedure calls are the mechanism by which MDICE controls the execution and synchronization of the participating applications. Each application posts a set of available functions and subroutines. These functions are invoked from MDICE script but are executed by the application program that posted the function. A typical script file, used in the current project for the prediction of tail buffeting, is shown in Figure 1.

In the specific simulation of vertical tail buffet prediction that is controlled by the script shown in Figure 1, the environment invokes four modules of the fluid dynamics module (CFD-FASTRAN), and one module of the finite-element structure dynamics module, CFD-ACEU (FEMSTRESS). In the first iteration, all modules of the fluid dynamics solver and structure dynamics solver start up and create MDICE objects. The next step is to assemble all fluid-structure and fluid-fluid interfaces. The assembly of the fluid-structure interfaces ensures the aligning of the computational fluid dynamics (CFD) and computational structure dynamics (CSD) patches. In the fourth block of the script, the main loop of the analysis starts by projecting the forces and moments from the fluid interfaces into the structural interfaces. The structural model is then solving for deflections. The deflections are then transferred to the fluid interfaces via fluid-structure patches. The fluid-flow solver is then solving for the new pressures on the solid surfaces.

The simulation panel of the MDICE is shown in Figure 2 for the aeroelastic tail buffeting simulation of F/A-18 fighter aircraft. The MDICE script is shown in the background of the figure. In addition to the multidisciplinary modules used to solve this complex problem, a dynamic snapshot of the total pressure iso-surfaces over the configuration model is displayed over the simulation panel using the CFDRC's flow visualization code (CFD-VIEW). Also shown are histories of the right tail tip bending and torsional deflections and right tail root bending moment. Both x-y images are displayed using the public domain module (XMGR). These images are graphically displayed in conjunction with MDICE GUI and are invoked from MDICE as separate display modules.

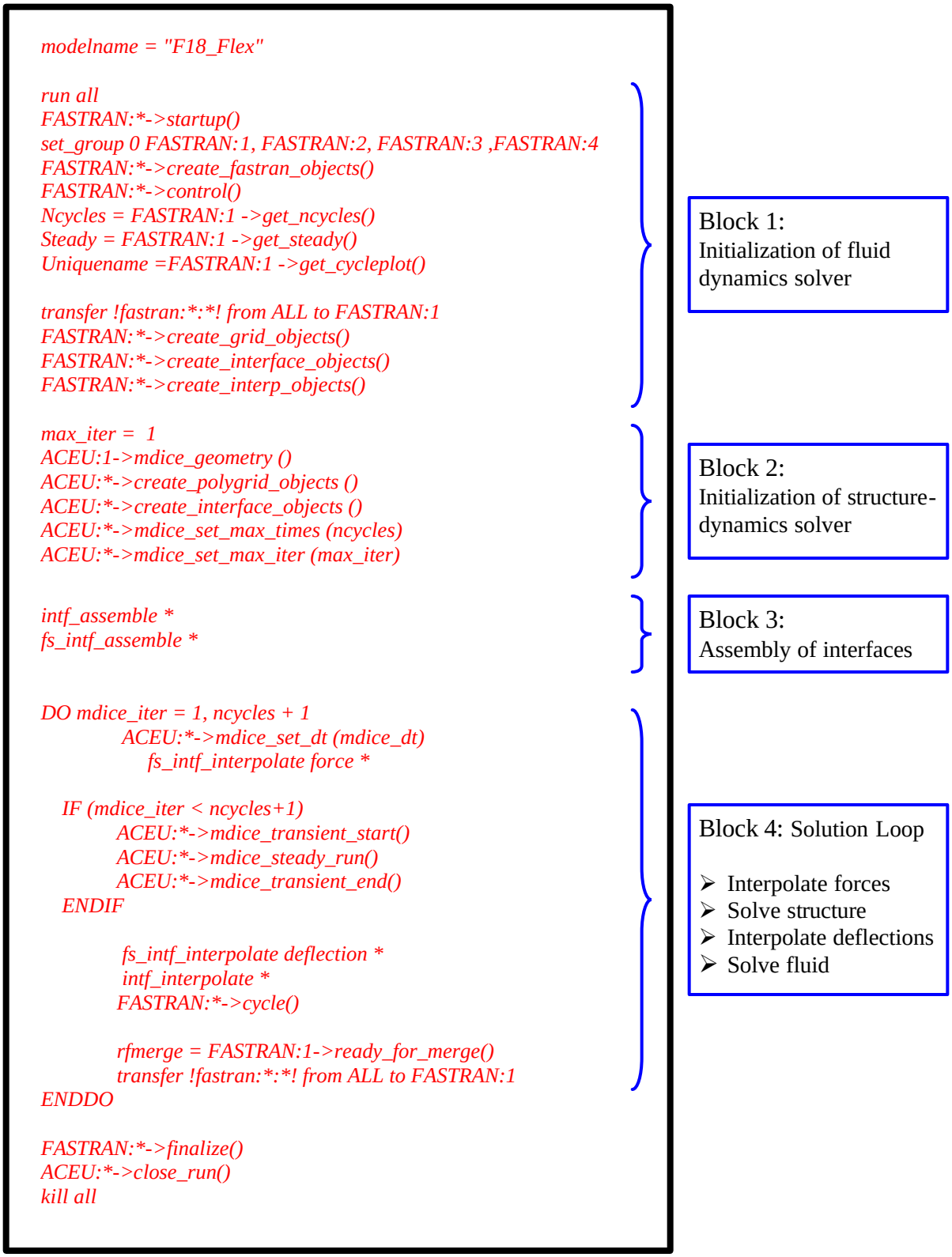

Figure 1. A Typical Script File Used for the Prediction of F/A-18 Tail Buffeting

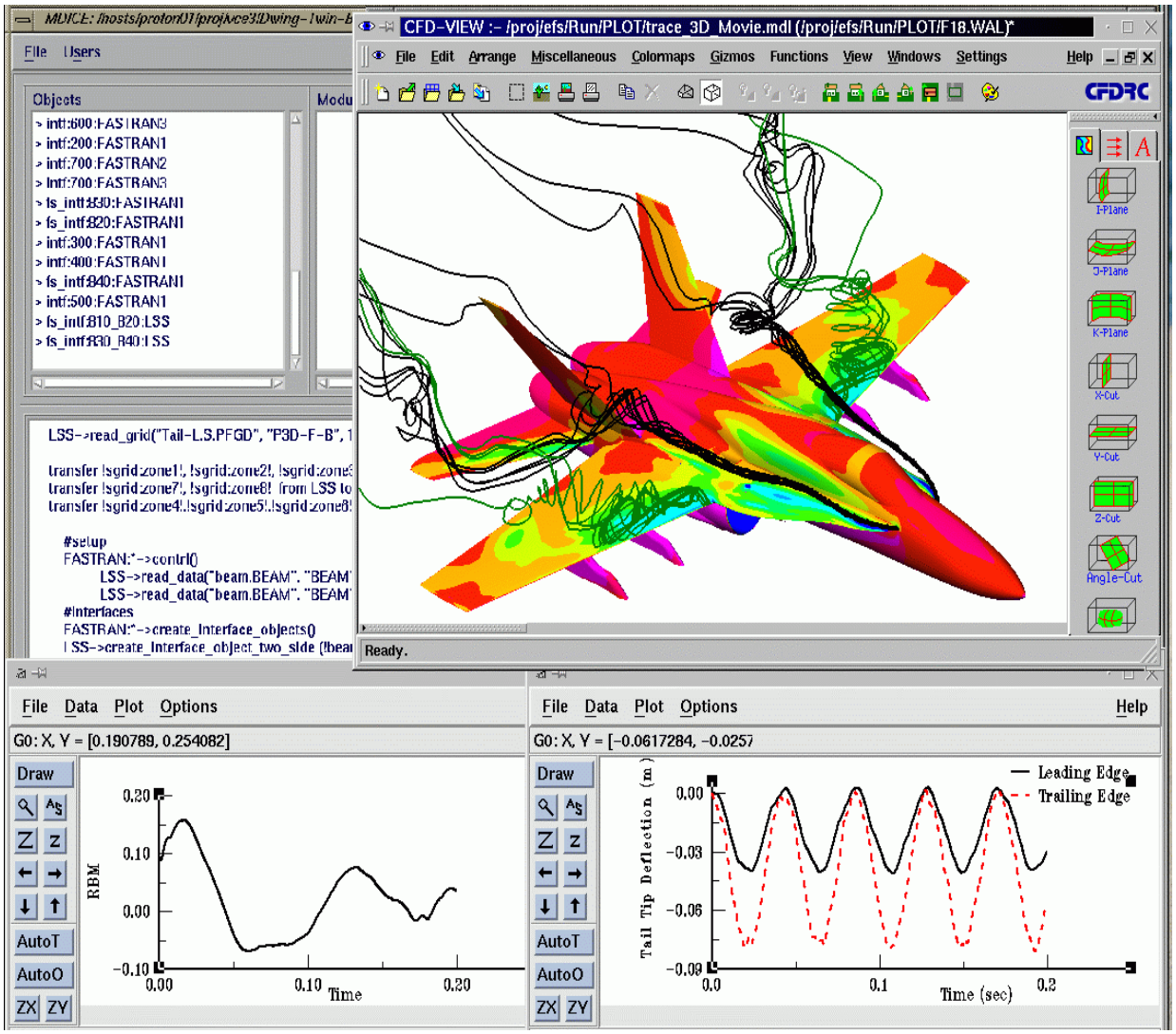

Figure 2. The Simulation Panel of the MDICE Showing the Aeroelastic Vertical Tail Buffeting of F/A-18 Fighter Aircraft; α=30.3^o, M=0.243, Re=11x10^6

4. PREDICTION AND VALIDATION OF F/A-18 TAIL BUFFETING

4.1 Introduction

In this section, MDICE is used to predict the vertical tail buffeting of F/A-18 aircraft at typical flight conditions. The problem is solved using two steps. The first step is to solve for the fluid dynamics flow field over rigid configuration. The initial conditions in this step are the undisturbed freestream flow. This step is computed to develop physical initial conditions around the configuration model. The second step is to solve for the aerodynamics and aeroelastic fields of the flexible configuration. In this step, the vertical tail is allowed to move and interact with the flow. The initial condition of this step is the solution at the end of the first step.

The flight conditions considered herein are corresponding to flight conditions of NASA F/A-18 High Alpha Research Vehicle (HARV). The aircraft is pitched over wide range of angles of attack ($\alpha = 25°$ to 40^o) at Mach number of 0.243 and a Reynolds number of 11×10^6. The inlet mass flow rate of the engine is 63 lbm/sec per engine, which is corresponding to the maximum power condition. Strong coupling between the fluid and structure is considered in this paper. Strong coupling occurs when the inertial effect of the motion of the solid is fed back into the fluid.

4.2 F/A-18 Geometry Modeling

The geometry of the full F/A-18 aircraft is modeled using a structured body-fitted grid system with one-to-one grid connectivity. The grid is generated using the geometry-modeling package CFD-GEOM of CFD Research Corporation. The surface grid of the F/A-18 aircraft is shown in Figure 3. The surface grid consists of the forebody, LEX, wing, vertical and horizontal tails, engine diffuser, inlet boundary layer diverter plate, exit vent, and pylon. The vertical tail rudder and the leading-edge flaps of the wing and horizontal tail are all set at zero angles.

The grid is a multiblock H-H grid consisting of 53 structured blocks utilizing 2.56 million cells (2.68 million grid points). The global grid extends five wing chords upstream and downstream of the aircraft, and eight wing chords normal to the aircraft. The grid is clustered near the apex and the leading edge of the wing LEX in order to produce robust and well-defined leading-edge vortices. The grid is very flexible and can be used with several fluid dynamics modules since the grid does not possess any Chimera, overlapping or high-order grid connectivity. Figure 4 shows the grid on a cross plane just ahead of the vertical tails, and Figure 5 shows the grid system on the symmetry plane. The grid around the vertical tail enables moving the grid points due to tail motion without regard to any grid discontinuity. If Chimera grid was used, an extensive cutting of holes in the grid would be necessary every iteration due to the motion of the tail.

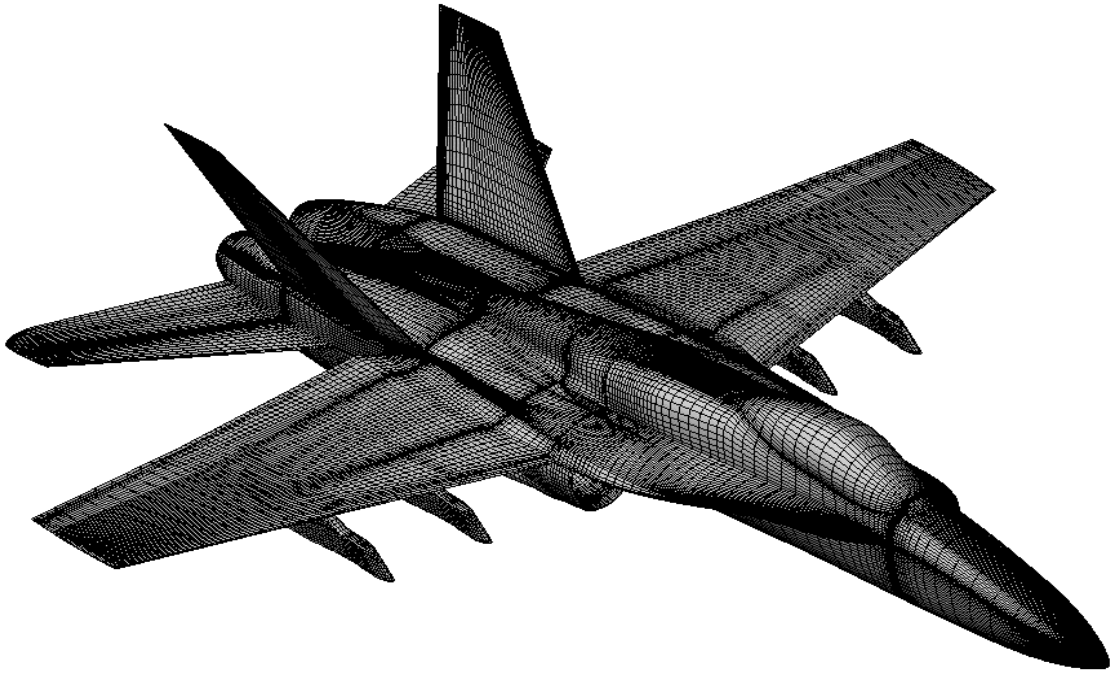

Figure 3. Surface Grid of the F/A-18 Aircraft

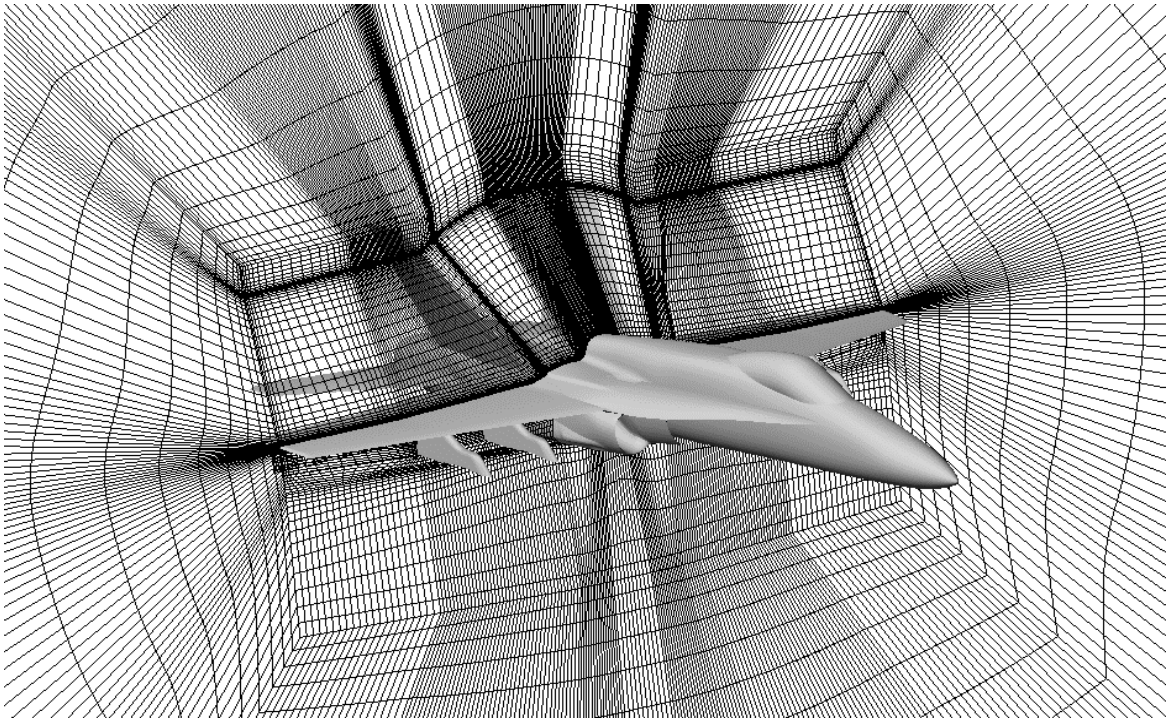

Figure 4. Front View of the Grid in a Cross Plane Around the Fuselage and Wing

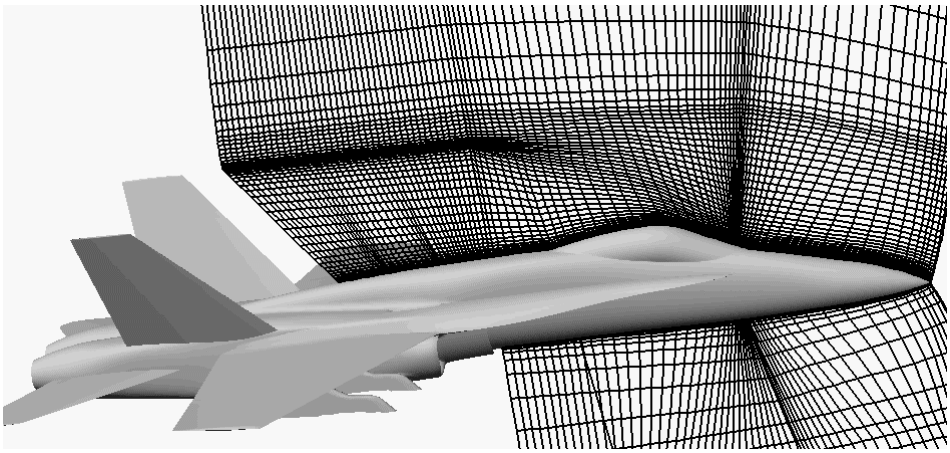

Figure 5. The Grid System on the Symmetry Plane

For the structure dynamics analysis, the vertical tail of the F/A-18 aircraft is modeled using second-order shell elements. The CFD and CSD surface grids of the vertical tail are shown in Figure 6. The CFD and CSD grids are not identical, and the forces and deflections are interpolated between the two grids using the conservative/consistent interfacing module outlined in the previous section. A total of 1,840 grid cells defined the CFD surface grid of the tail, while 576 grid cells defined the CSD surface grid of the tail. The material of the vertical tail is assumed to be aluminum and isotropic. The Young's modulus of elasticity is 6.896×10^{10} N/m^2, the density is 2765 kg/m^3, and the Poisson's ratio is 0.33.

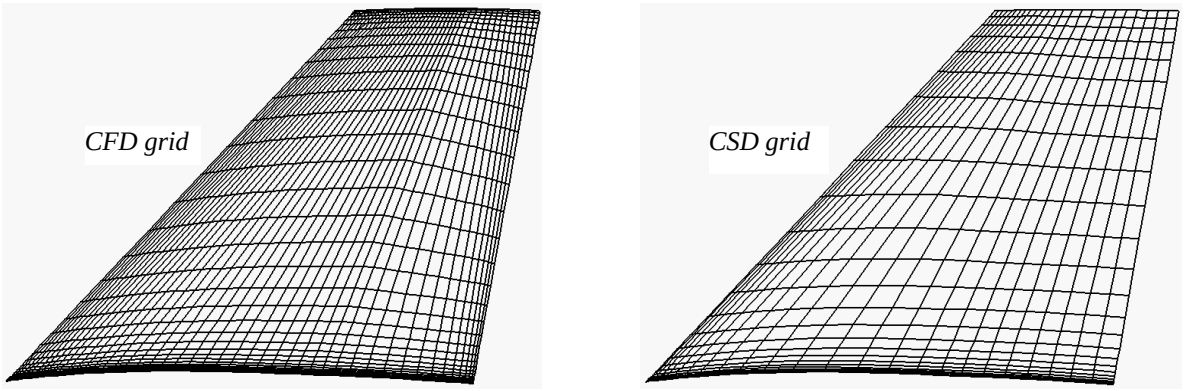

Figure 6. Surface Grid of the Vertical Tail

Initially, the method of modal analysis is used to compute the structural modes of the vertical tails. The first few natural frequencies of the vertical tail are given in Table 1.

Table 1. Natural Frequencies of the Vertical Tail of the Current F/A-18 Model

Structural modes of the vertical tail	**Natural frequencies of the current F/A-18 model**	**Natural frequencies of the F/A-18 aircraft**
First bending	20 Hz	15.5 Hz
First torsion	60 Hz	45 Hz
Second bending	69 Hz	61 Hz

The natural frequencies of the current model are not the exact frequencies of the F/A-18 aircraft. This is because the vertical tail in the current model is assumed as one-block structure, where the details of the tails construction are ignored. The rudder is also not modeled in this work. However, the material properties of the tail structure may be easily adjusted to yield the frequencies of the vertical tail of the F/A-18 aircraft. The first bending and torsion modes and the second bending mode of the vertical tail are shown in Figure 7.

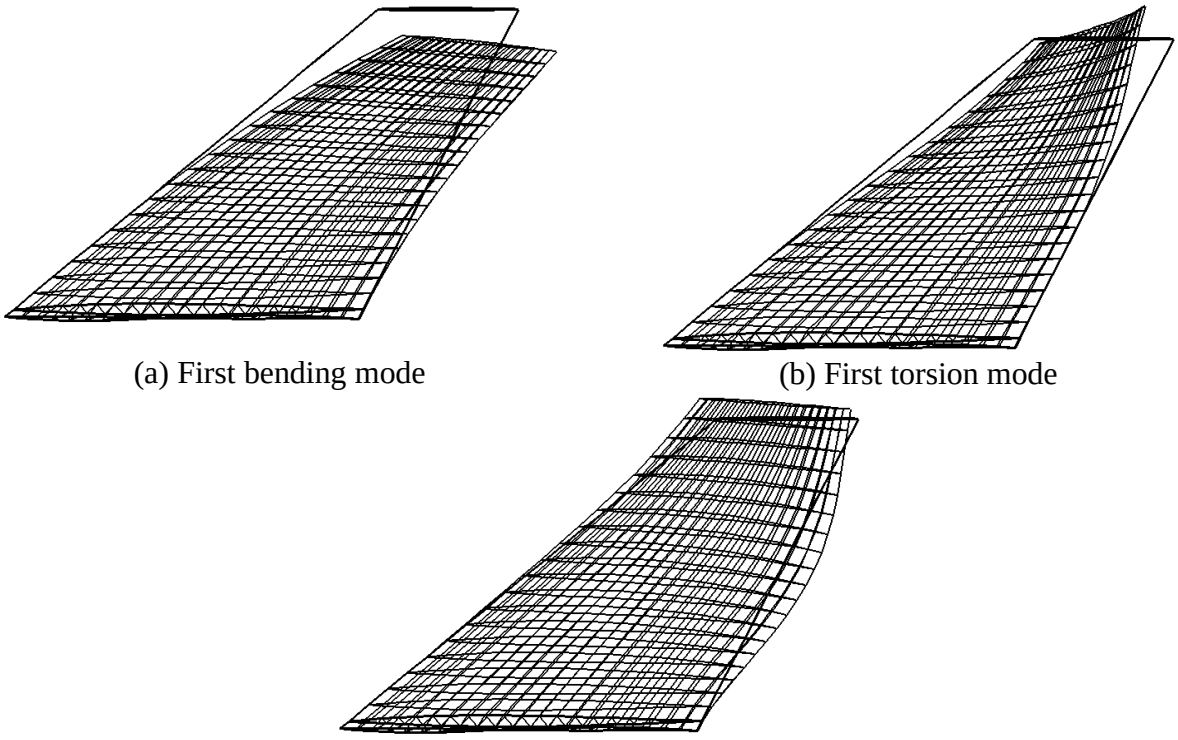

(a) First bending mode

(b) First torsion mode

(c) Second bending mode

Figure 7. The First Three Structural Modes of the Vertical Tail

4.3 Flow Field Characteristics

The flow field at high angles of attack is characterized by highly unsteady spiral flow, massive three-dimensional separation, and unsteady vortex breakdown location. This imposes different levels of pressure gradients upon the vertical tails. The total pressure contours on crossflow planes at different longitudinal locations on the F/A-18 aircraft at 30° angle of attack are shown in Figure 8. The oncoming flow initially attaches to the lower surface of the LEX, and then moves toward the leading edge. The flow separates from the sharp leading edge of the LEX, forming a free-shear layer. The spanwise pressure gradient on the upper surface of the LEX causes the shear layer to move inward and roll up into a concentrated spiral flow to form the primary vortex. The flow moving around the vortex is swept downward and reattaches on the upper surface of the LEX. The attached flow then moves outward underneath the primary vortex toward the leading edge. The pressure gradient induced by the primary vortex causes the attached flow to separate forming a smaller secondary vortex that is rotated in the opposite direction to that of the primary vortex. As the flow travels downstream, the primary vortices gain strength and move upward and to the outward direction. As the flow moves downstream of the

wing apex, another vortex starts to roll up in the same way as the LEX vortex. This is the primary vortex of the wing. Figure 8 shows that the vortical flow of the LEX and the wing vortex cores are merging together before they reach the vertical tail. The two vortices are trailing downstream, and the vortex cores start to vanish, an indication of loss in the total pressure and axial momentum. Later, the vortex cores break down before they reach to the vertical tail. Another vortex is generated at the tip of the wing that trails downstream away from the vertical tail. As the vortical flow crosses the leading edge of the vertical tail, a smaller vortex develops at the root of the tail underneath the primary LEX vortex. The tail vortex exists totally at the outer surface of the vertical tail, and it is rotating in the opposite direction to that of the primary LEX vortex.

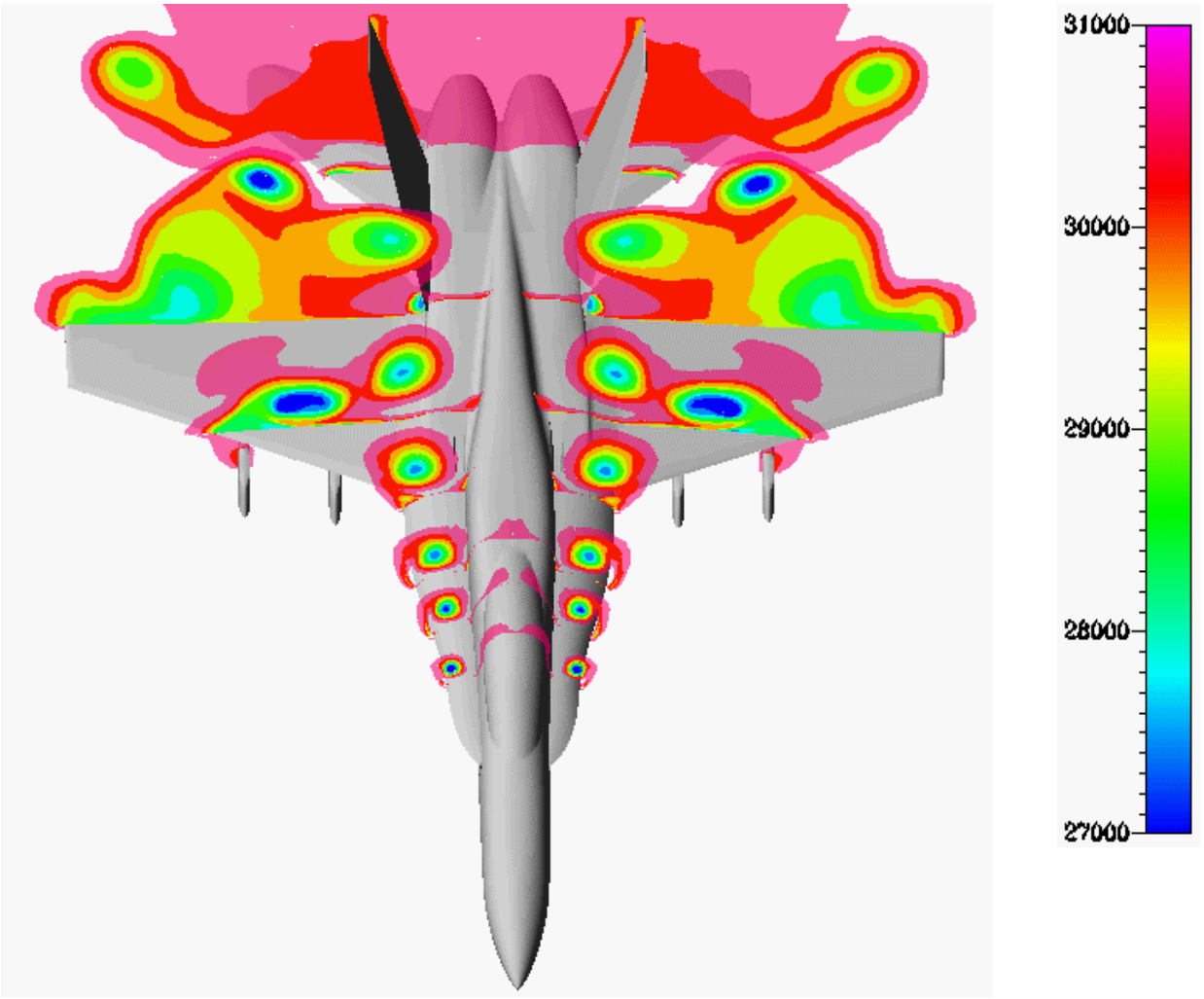

Figure 8. Total Pressure Contours on Crossflow Planes at Different Longitudinal Stations

The total pressure contours on a ray-cutting plane passing through the core of the LEX vortex is shown in Figure 9. Figure 9 shows the upward motion of the LEX vortex core and the loss of the total pressure of the vortex as it trails downstream. Figure 9 also shows the breakdown of the vortex upstream of the vertical tail.

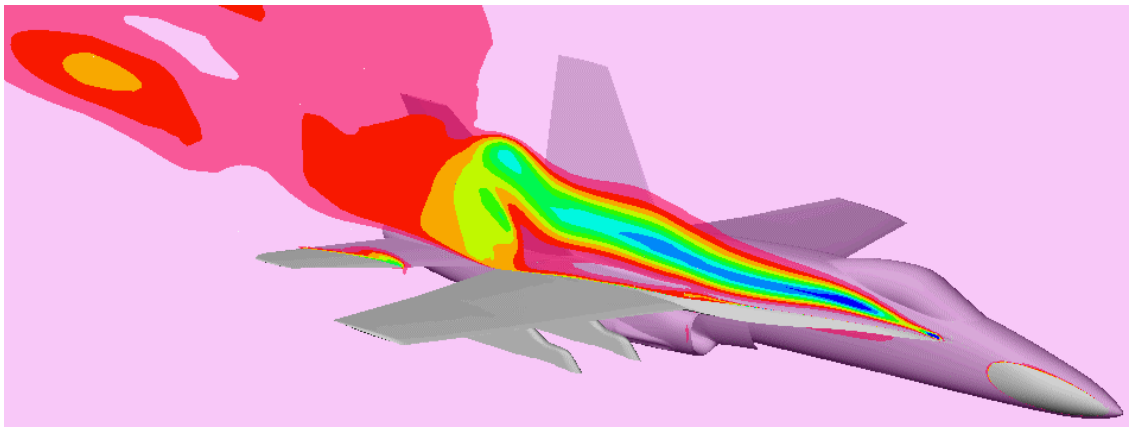

Figure 9. Total Pressure Contours on a Ray-cutting Plane Passing Through the LEX Vortex

The contour plots of the negative pressure coefficient ($-C_p$) on the inboard and outboard surfaces of the vertical tail at $\alpha = 30^o$ after 0.1 seconds are shown in Figure 10. The contour plots at the tail tip indicate that the net force is directed inboard, while at the tail root and midspan area, the net force is directed outboard. When the differential pressure at the leading edge of the tail is compared to the differential pressure at the trailing edge, the results indicate that the vertical tail is also subject to torsional loads. The torsional loads at the tail tip are directed in the counter-clock-wise (CCW) direction, looking to the right tail from top. At the tail root, the torsional loads are directed into the opposite direction.

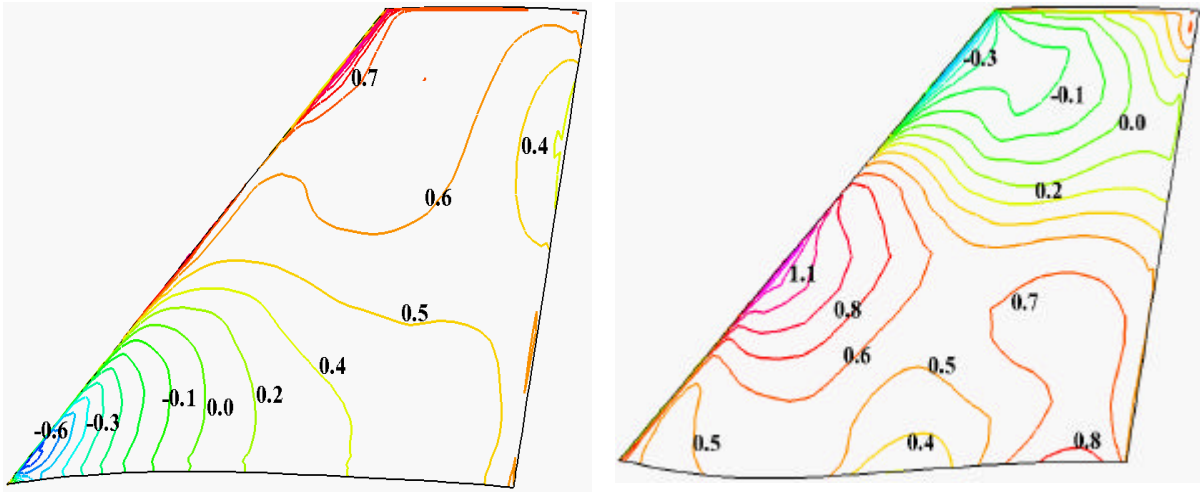

(a) Inboard surface (b) Outboard surface

Figure 10. Contour Lines of Pressure Coefficient, $-C_P$

The surface pressure coefficient on the upper and lower surfaces of the LEX at different fuselage stations (FS) at $\alpha = 30^o$ are shown in Figure 11. The results are compared with HARV flight test data (Fisher et al. 1990) at three different FS. The spanwise coordinate is normalized by the span of the LEX at every fuselage station such that the normalized coordinate is 0.0 at the leading edge of the LEX and 1.0 at the intersection with the fuselage. Two suction peaks are shown in the pressure distribution. The suction peaks correspond to the core of the primary and secondary

LEX vortices, respectively. The pressure peaks and the positions of the vortex core of the primary vortex are accurately captured at all stations. However, the pressure peak of the secondary vortex at the aft position is over estimated. Figure 11 also shows the outboard motion of the core of the leading-edge vortices as the flow travels downstream. This is indicated form the outboard spanwise motion of the primary suction peak.

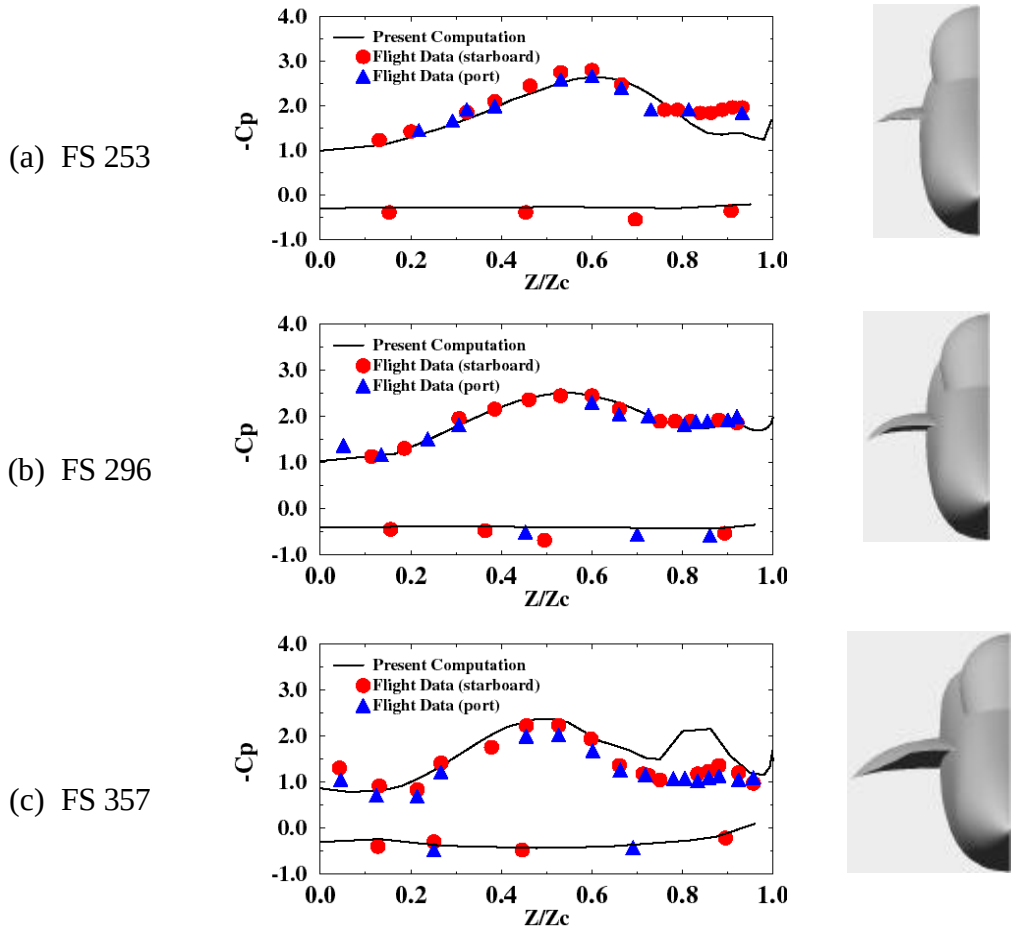

Figure 11. Surface Pressure Coefficient Over the LEX, Compared with the Flight Data of Fisher et al. *(1990)*

The total pressure contours on the crossflow plane at the leading edge of the wing root (x = 9.5m) are shown in Figure 12. Two vortices are shown in Figure 12. The inboard vortex corresponds to the LEX vortex. The outboard vortex corresponds to the wing vortex. At $\alpha = 25°$ and 30°, the core of the LEX vortex can be easily seen. At $\alpha = 35°$, the vortex core started to disappear due to vortex diffusion. The vortex core is no longer visible at $\alpha = 40°$, which shows that the onset of vortex breakdown moved upstream of the leading edge of the wing root. The total pressure contours on crossflow plane at the leading edge of the vertical tail root (x = 11m) are shown in Figure 13. The core of the LEX vortex can be only seen at $\alpha = 25°$. The core of the LEX vortex disappears at higher angles of attack due to the upstream motion of the vortex breakdown flow. The core of the LEX and wing vortices can be seen outboard of the vertical tail at all angles of attack.

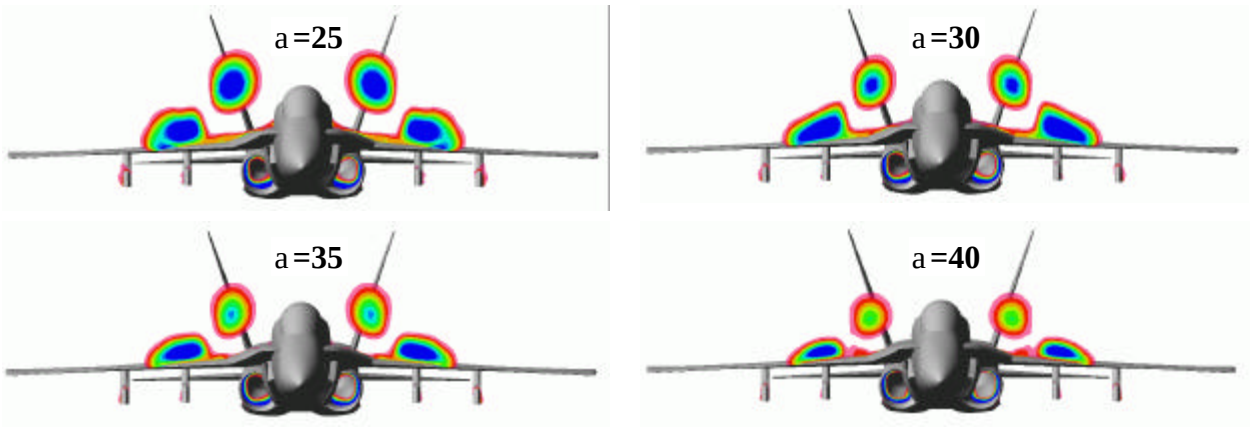

Figure 12. Total Pressure Contours on Crossflow Plane at the Wing Root Leading Edge

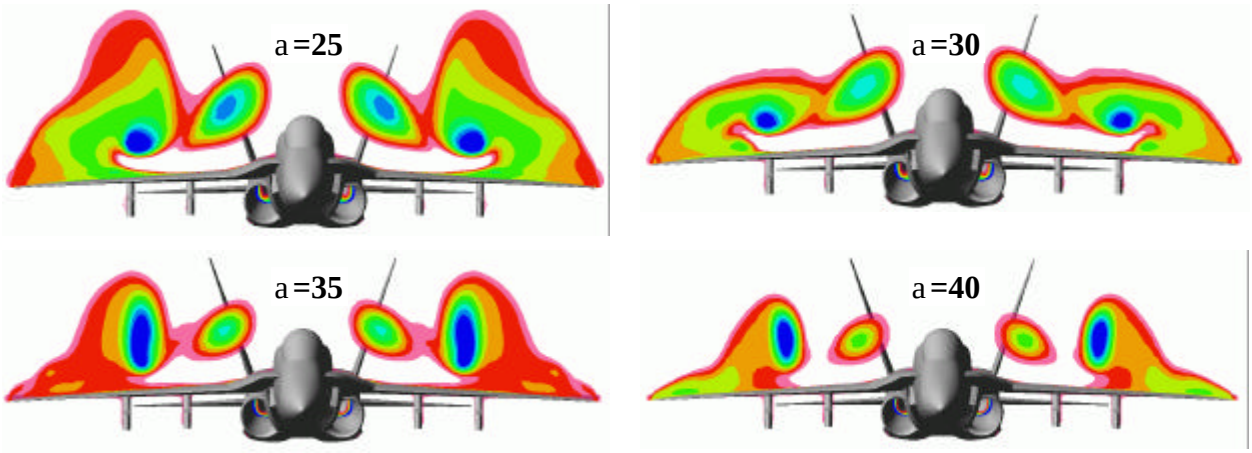

Figure 13. Total Pressure Contours on Crossflow Plane at the Tail Root Leading Edge

Three-dimensional, front view and side view snapshots of the F/A-18 aircraft and the instantaneous streamlines of the LEX and wing vortices at four different angles of attack are shown in Figures 14 and 15. The figures also show the surface static pressure on the aircraft surfaces. As the leading-edge vortex travels downstream, the core of the vortex makes an abrupt kink and forms a spiral vortex. The spiral vortex was also observed by Fisher et al. (1990) in flight tests of the F-18 HARV vehicle. The spiral vortex persists for several turns (especially at lower angles of attack) before breaking up. The sense of the spiral vortex is opposite to the direction of rotation of the leading-edge vortex. The sense of spiral vortex may have to be opposite to the direction of rotation of the main vortex in order to generate stagnant vortex core, a phenomenon that accompanies vortex breakdown, see Jumper et al. (1993). At an angle of attack of 25°, the LEX and wing vortices break down just ahead of the vertical tail. As the angle of attack increases, the onset of vortex breakdown moves upstream and upward, and the vortex breakdown flow becomes larger in size. The vertical tail is emerged in the vortex breakdown flow at all angles of attack. The figure also shows that at higher angles of attack, the inboard space between the vertical tails entrains more vortical flow. The contour plots over the vertical tail shows that pressure gradient develops on the surfaces of the tail. The pressure gradient increases with the increase of angle of attack.

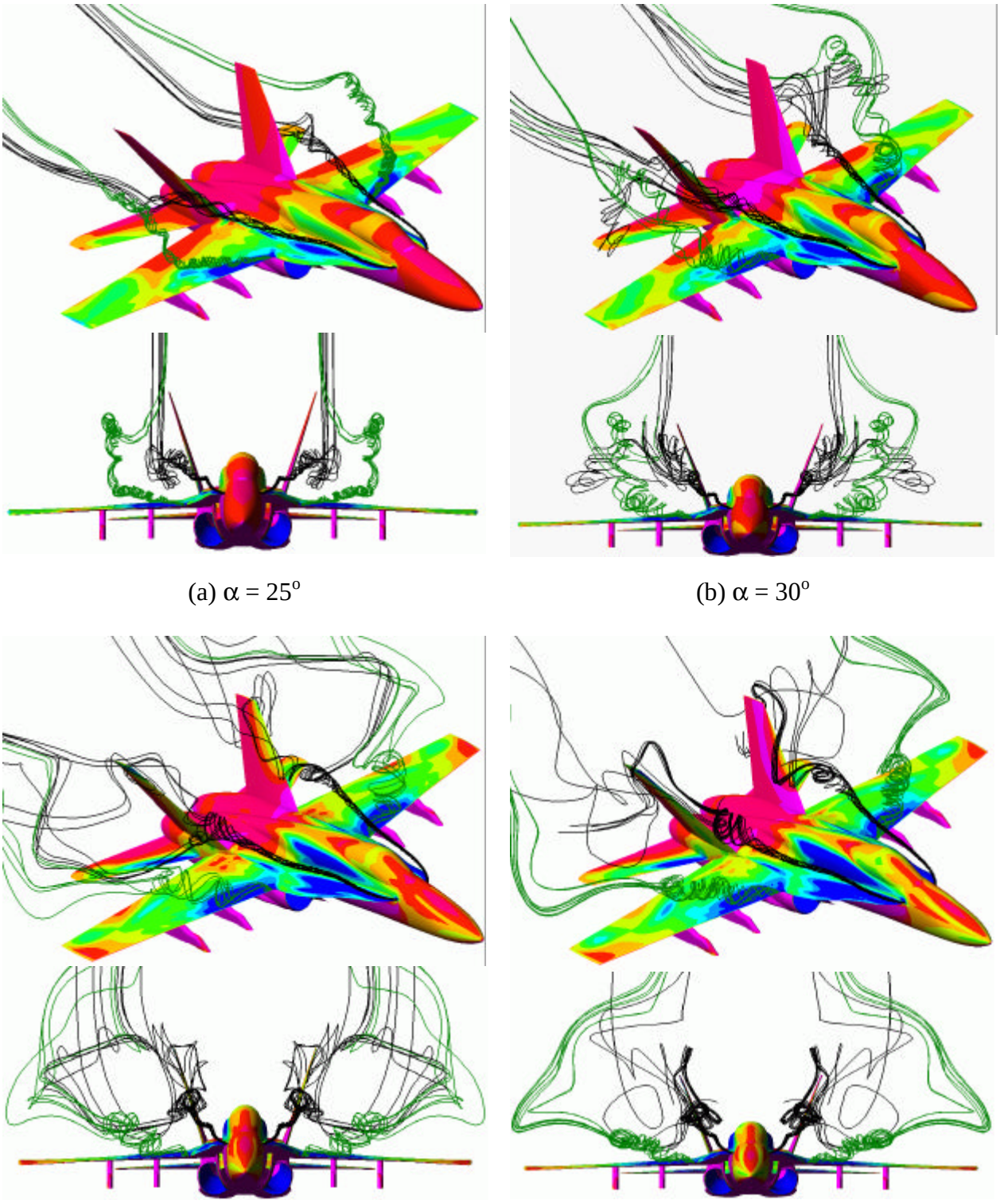

(a) $\alpha = 25^{o}$ (b) $\alpha = 30^{o}$

(c) $\alpha = 35^{o}$ (d) $\alpha = 40^{o}$

Figure 14. Three-dimensional View and Front View Snapshots of the F/A-18 Aircraft Showing the Instantaneous Streamlines of the LEX and the Wing Leading Edge

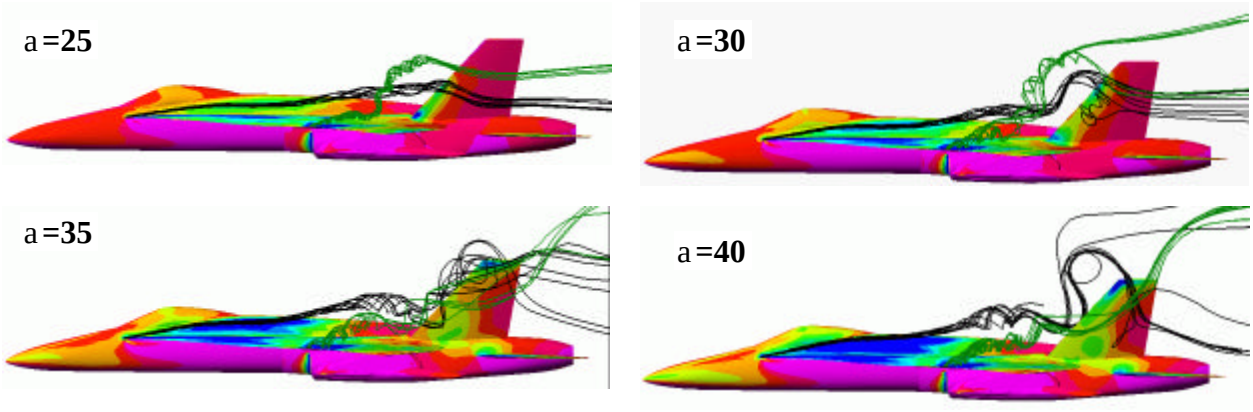

Figure 15. Side View Snapshots of the F/A-18 Aircraft Showing the Instantaneous Streamlines

4.4 Root Bending Moment of the Vertical Tail

In order to analyze the unsteady pressure and differential pressure across the tail, the unsteady pressure is monitored on both sides of the vertical tail at 16 selected locations. The locations of the points are selected to match most of the locations of previous experimental and flight test data (Meyn et al., 1994). The locations of the monitor points on the vertical tail are shown in Figure 16.

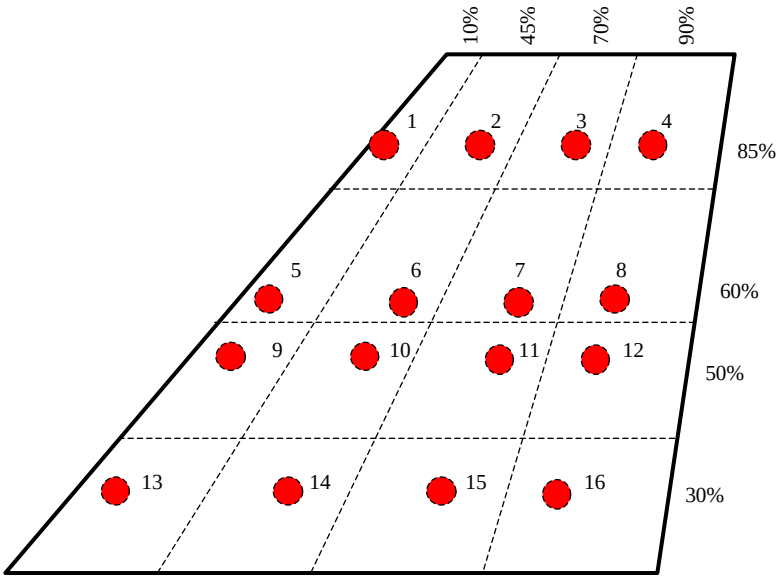

Figure 16. Pressure Monitor Transducer Locations on the Vertical Tail

The differential pressure on the vertical tail is integrated to yield the root bending moment (RBM). The RBM is computed using differential pressure from the 16 transducer locations on the vertical tail, similar to what was done in the experimental and flight test data of Pettit et al. (1994), Meyn et al. (1994) and James and Meyn (1994). The surface pressure surrounding the pressure transducer was assumed to be constant. The loads were assumed to act on the centroid of each area surrounding the transducers. The moment arm is measured from each cell centroid to the tail root. The time histories of the tail root bending moment coefficient, C_{rbm}, at different

angles of attack are shown in Figure 17. Figure 17 shows unsteady, large-amplitude oscillatory loads at all angles of attack. The amplitude and the mean value of the RBM are maximum in the range of 30° to 40° angles of attack. This is when the vortex breakdown moves upstream of the vertical tail. The history of RBM at lower angles of attack (not shown) did not show this large amplitude of the unsteady loads. Therefore, vortex breakdown phenomenon appears as the most predominant source of vertical tail buffeting of fighter aircraft. Positive RBM indicates moment that is directed outboard. Therefore, at an angle of attack of 25°, the RBM is mainly directed inboard. At higher angles of attack the RBM is directed outboard.

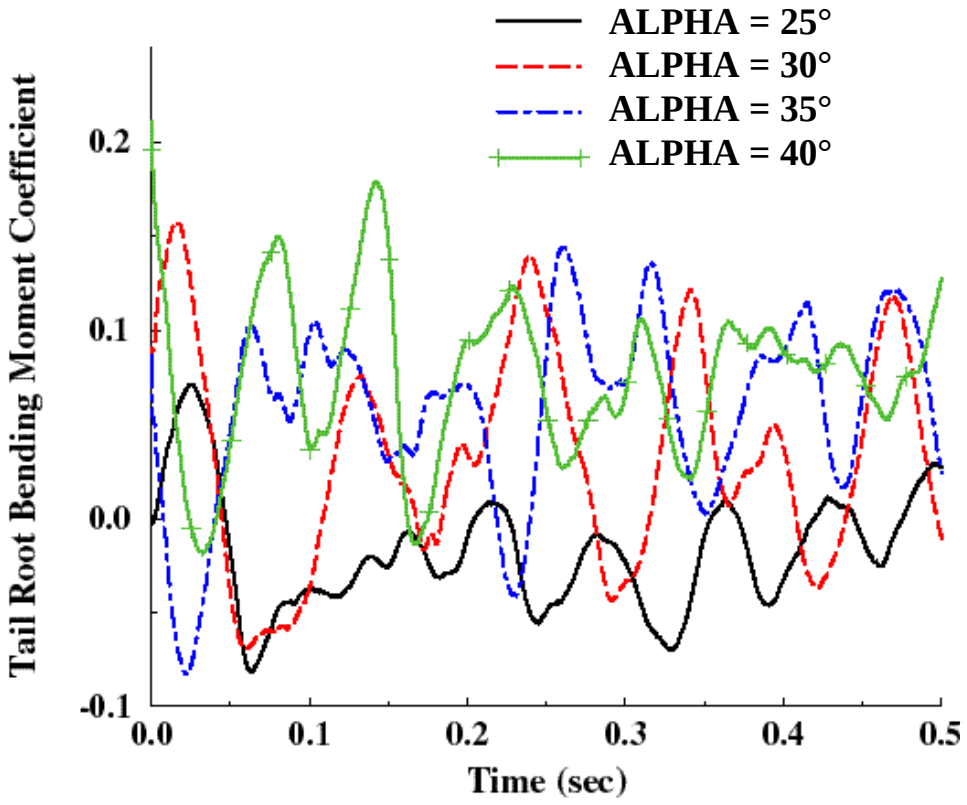

Figure 17. The Root Bending Moment Coefficient of the Vertical Tail

The root-mean-square (RMS) of the tail root bending moment coefficient is shown in Figure 18. The results are compared with the full-scale wind tunnel data of Pettit et al. (1994) and James and Meyn (1994). The experimental data were obtained using different sensor densities and slightly different model setup. Pettit et al. (1994) used a 6×6 transducer array, while James and Meyn (1994) used a 6×8 transducer array. James and Meyn (1994) showed that the density of the transducers array affects the integration of the buffet loads on the vertical tail. The results compare well with the experimental data over a wide range of angles of attack. The maximum root bending moment occurs around the 30° angle of attack. That is when the vortex breakdown is completely ahead of the leading edge of the vertical tail. At higher angles of attack, the root bending moment decreases due to the diffusion of the vortex breakdown flow before it impinges upon the vertical tail. At low angles of attack ($\alpha < 25°$), there is still a substantial amount of buffet. This buffet occurs even when the onset of vortex breakdown is downstream the vertical tail. This observation suggests that the vortex breakdown may not be the only source of vertical

tail buffeting of fighter aircraft. This was also observed experimentally by Gursul and Xie (1999). Several unsteady phenomena may contribute to the tail buffeting at lower angles of attack, such as vortex shedding, wakes from different parts of the aircraft, unsteady flow separation from the leading edge of the vertical tail (as observed in Figure 8), and adverse feedback from the unsteady location of the onset of vortex breakdown.

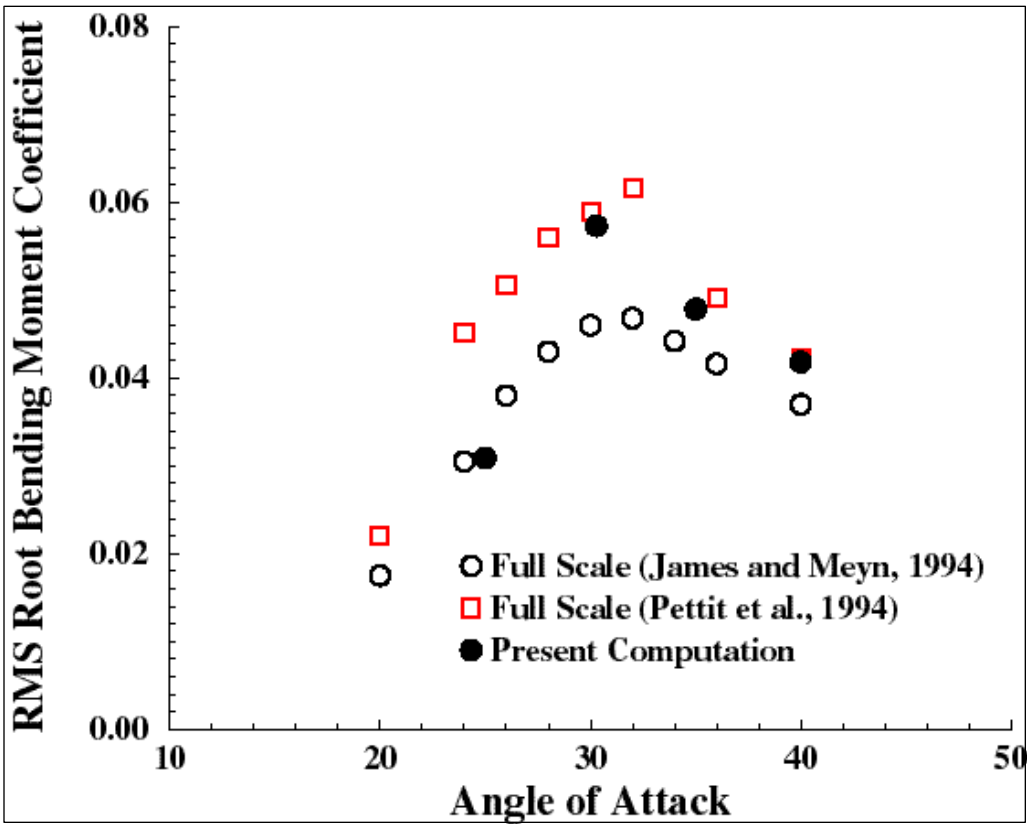

Figure 18. RMS of the Tail Root Bending Moment Coefficient

4.5 Unsteady Pressures on the Vertical Tail

Several publications have reported experimental and flight test data at the 45 percent chord and 60 percent span point on the vertical tail. This would ensure that results from different sources of tests and flight data had a common point for comparison. Thus, the unsteady pressure history at this point was monitored and analyzed for comparison. The time histories of the inboard, outboard, and differential unsteady pressure coefficients at the 45 percent chord and 60 percent span point are shown in Figure 19. Figure 19 indicates that the inboard surface of the tail experienced larger amplitude of fluctuation than the outboard surface, except at 25° angle of attack. This indicates that the inboard surface of the vertical tail has more significant contribution in the unsteadiness of the problem than the outboard surface.

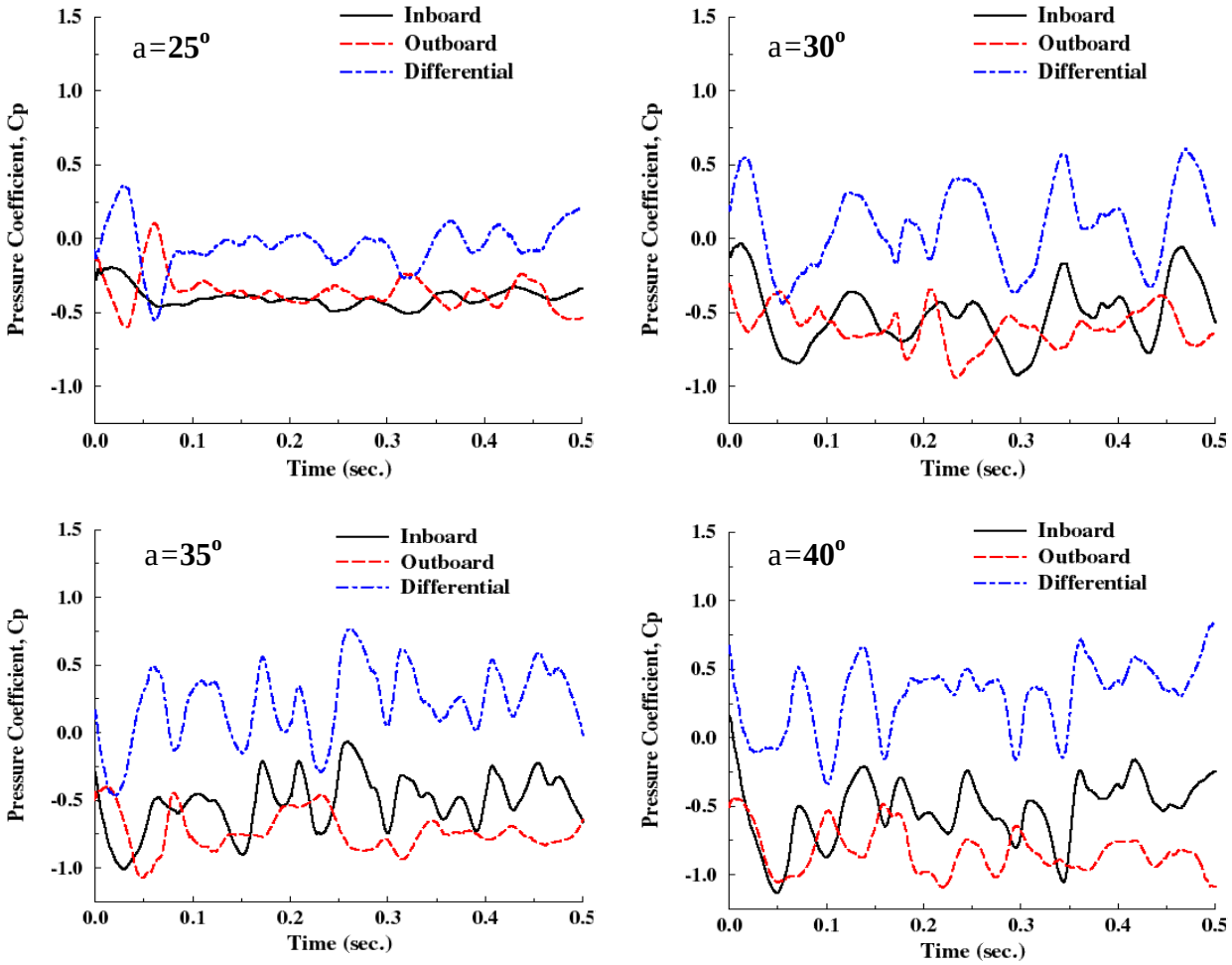

Figure 19. The Time Histories of Unsteady Pressure Coefficients on Vertical Tail at 45 Percent Chord and 60 Percent Span

The RMS of inboard, outboard, and differential pressure coefficients are shown in Figure 20. The results are compared with flight test data, full-scale, and the 16-percent-scale wind tunnel data of Meyn et al. (1994). The results compared well with the experimental and flight test data over wide range of angles of attack. The RMS pressure of the inboard surface is larger than the RMS pressure of the outboard surface, which emphasized the previous conclusion that the inboard surface of the vertical tail has more significant contribution in the unsteadiness of the buffet problem. In addition, the results indicated that the RMS of the outboard pressure is less sensitive to the angle of attack than the inboard pressure. This is probably because of the location of the vortical flow with respect to the tail. Initially, most of the vortical flow exists at the outer surface of the tail. As the angle of attack increases, the vortex breakdown flow moves inboard, imposing different levels of unsteady pressures on the inboard surface of the tail. Analysis of the differential pressure at the 16 transducer locations revealed that the leading edge of the vertical tail experiences the largest RMS pressures, while the trailing edge of the vertical tail experiences the lowest RMS pressures. The RMS of the differential pressure at the root of the vertical tail is larger than the RMS differential pressure at the tail tip. This observation applies to all angles of attack considered.

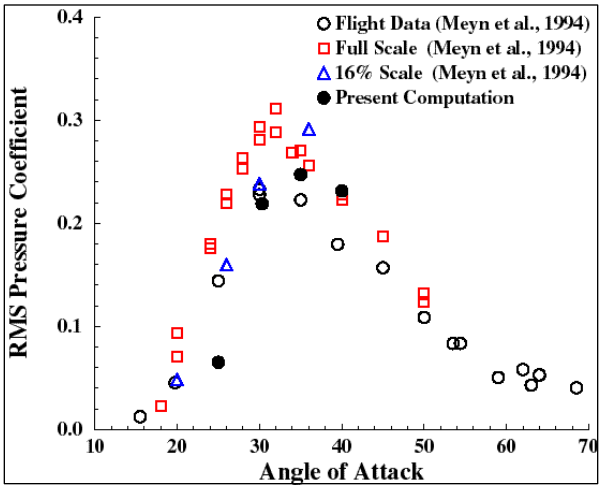

(a) Inboard surface pressure

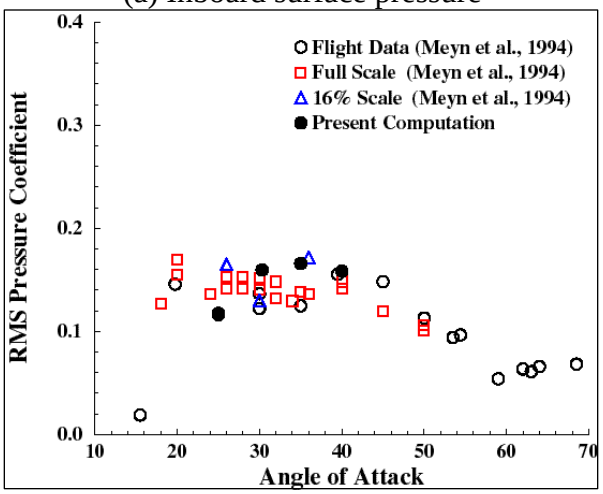

(b) Outboard surface pressure

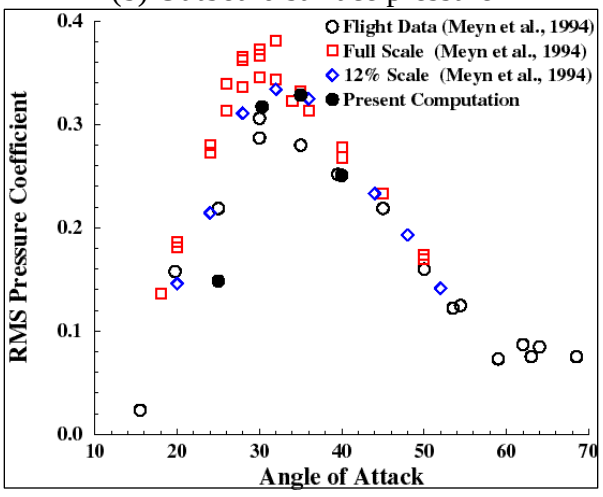

(c) Differential pressure

Figure 20. RMS Pressure Coefficient at 45 Percent Chord and 60 Percent Span

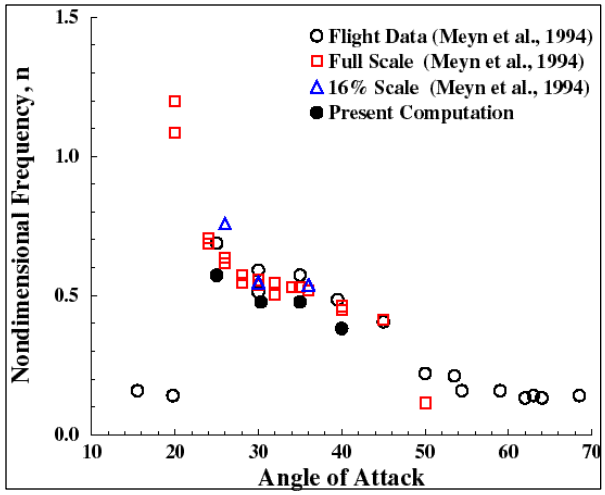

(a) Inboard surface pressure

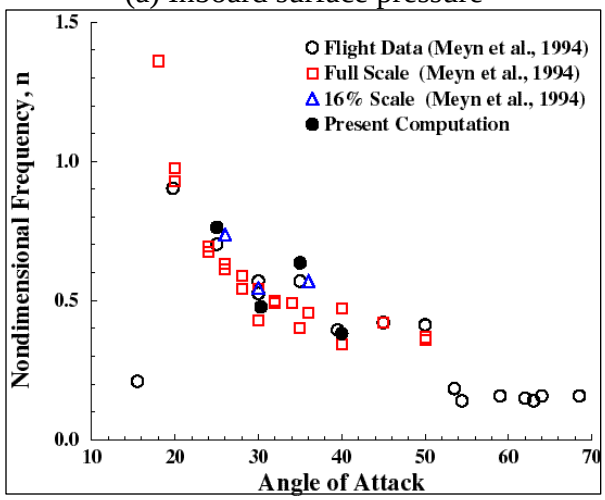

(b) Outboard surface pressure

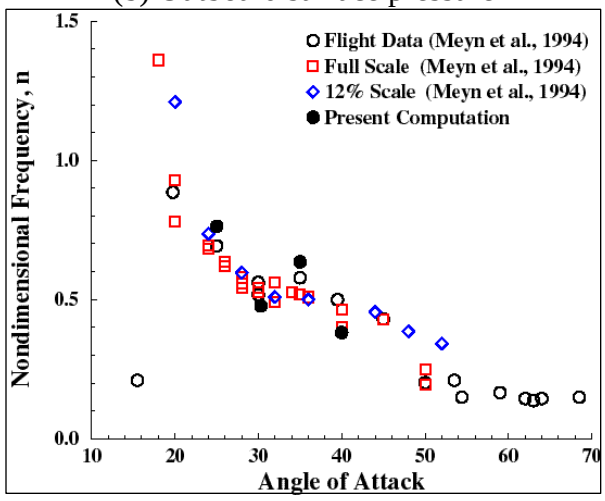

(c) Differential pressure

Figure 21. Predominant Frequencies of Buffet Pressure at 45 Percent Chord and 60 Percent Span

The power spectral density (PSD) of the signal of the unsteady pressure coefficients was computed using MATLAB® toolbox. The buffet pressure spectra are normalized by the freestream dynamic pressure, and it is presented as $\sqrt{nF(n)}$, where *F(n)* is the buffet excitation PSD and *n* is the nondimensional frequency. The PSD is computed based on a time span of 0.5 seconds. The length of the time record is fairly sufficient since there are no abrupt changes in the signal and the vertical tail response is nearly periodic (see section 4.6). The predominant frequencies of the buffet pressure peaks are shown in Figure 21 for the inboard pressure, outboard pressure, and differential pressure coefficients. The pressure frequencies compared quite well with the experimental and flight test data over the angle of attack range. In general, the peaks of the buffet excitation shift into lower frequencies as the angle of attack increases. This shift of the frequency at high angles of attack has been observed by several researchers using different models, e.g., Washburn et al. (1993), Pettit et al. (1994), and Meyn et al. (1994).

The PSD peak of the excitation spectra of the differential pressure coefficient is compared with the experimental data in Figure 22. The peak power of the differential pressure compared quite well with the experimental data over the angle of attack range. The maximum buffet excitation occurs between the 30° to 35° range of angles of attack. A large increase in the peak of the buffet differential pressure occurs at 25° angle of attack, an indication that the vortex breakdown flows moved ahead of the leading edge of the vertical tail.

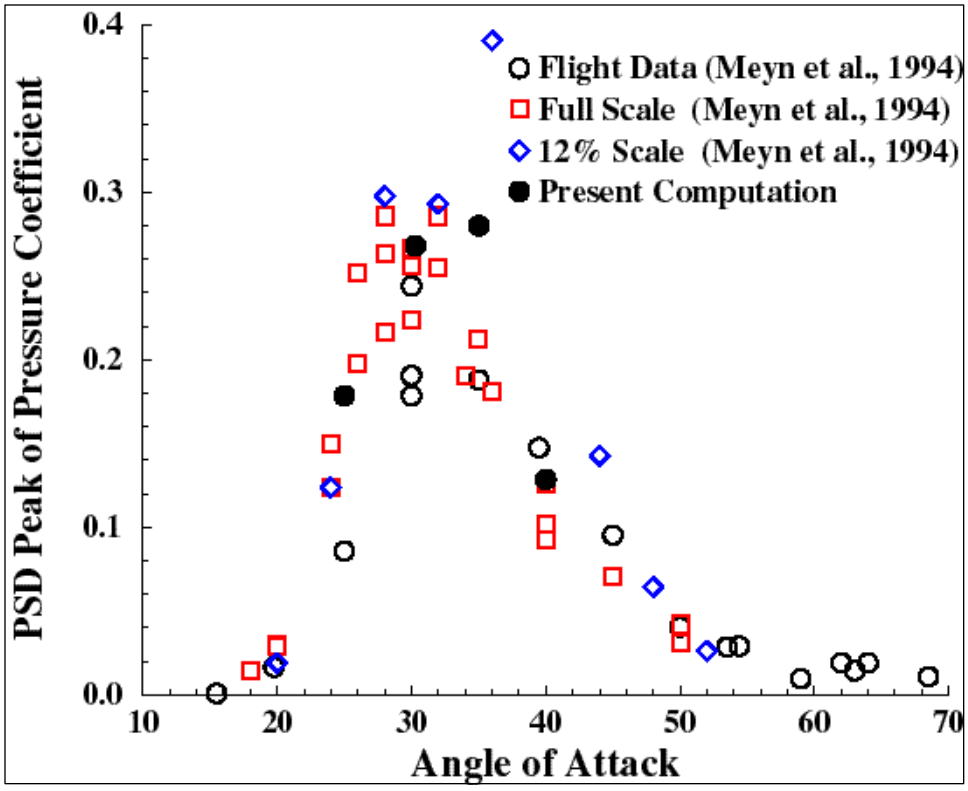

Figure 22. PSD Peak of Differential Pressure Coefficient at 45 Percent Chord and 60 Percent Span Point

4.6 Aeroelastic Deformation of the Vertical Tail

The aeroelastic deformations and accelerations are monitored at the leading and trailing edges of the tail tip. The time histories of the tail tip normal deflections are shown in Figure 23 for the case of angle of attack of 30^{o}. Figure 23 shows the oscillatory nature of the deflection around a slightly negative mean toward the outboard direction. This is because most of the vortical flow exists at the outboard of the vortical tails, as shown in Figures 8 and 14. The vortical flow produces suction pressures, which tends to move the tail surface toward the outboard direction. The trailing edge of the tail experiences higher amplitude of deflections than that of the leading edge. This indicates that the vertical tail exhibits torsional response, in addition to the primary bending response. This observation is consistent with the torsional loads observed upon the vertical tail.

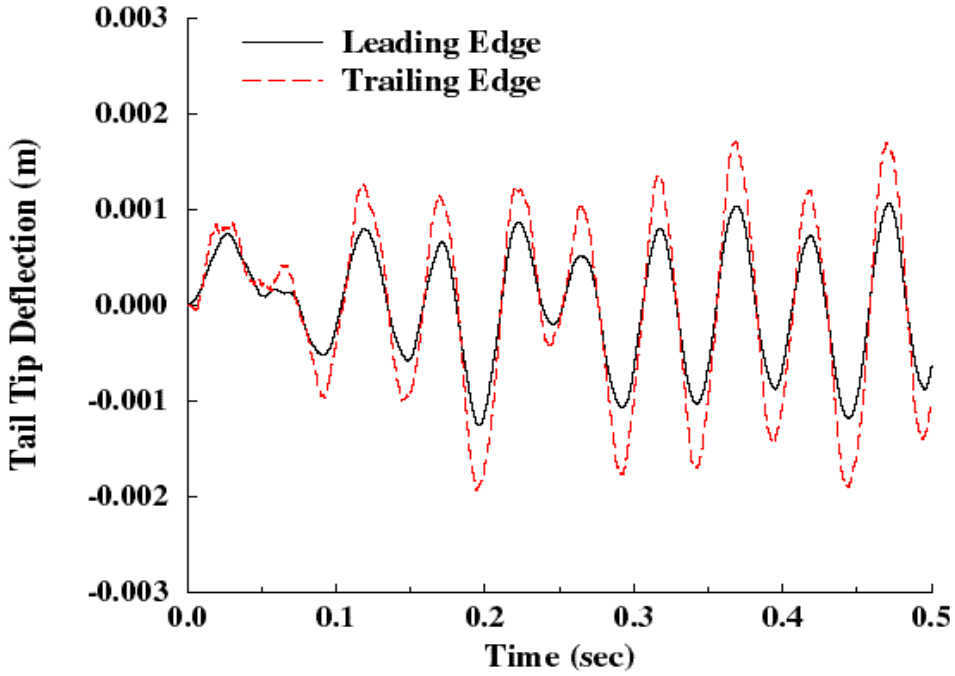

Figure 23. The Time History of the Normal Deflection of the Vertical Tail Tip

The PSD of the tail tip acceleration is shown in Figure 24 for the leading-edge and trailing-edge points. The power spectral density of the accelerations is computed in the non-dimensional form *Z(n)*, where $Z(n) = PSD(\ddot{Z}) \cdot (U_{\infty}/\overline{C})$. The figure shows that the acceleration power at the trailing-edge point is larger than that at the leading-edge point. The predominant nondimensional frequency of the tail tip acceleration is 1.0 in agreement with the experimental value reported by Pettit et al. (1994). The first two peaks occur around the nondimensional frequencies of 1 and 3, corresponding to the first bending and torsion modes. The first peak is significantly higher than the second peak, which indicates the dominance of the first bending mode. A third peak occurs at the second bending mode but with a smaller level than the peaks at the first two modes, which indicates that the contribution of the second bending mode is not significant at these conditions.

The distributions of the tail deflections along the span of the leading edge of the vertical tail at different time instances are shown in Figure 25. As shown from Figure 25, the first bending

mode is dominant in the deflections of the vertical tail. A snapshot of the deformed vertical tail of the F/A-18 aircraft after 0.11 seconds is shown in Figure 26. This snapshot is corresponding to the point of maximum deflection in the second cycle of response. In Figure 26, the deformation is magnified four times for the sake of clarity. As shown in Figure 26, the vertical tail is responding mainly in the first bending mode. The tail also exhibits torsional deflections in the CCW direction looking upstream.

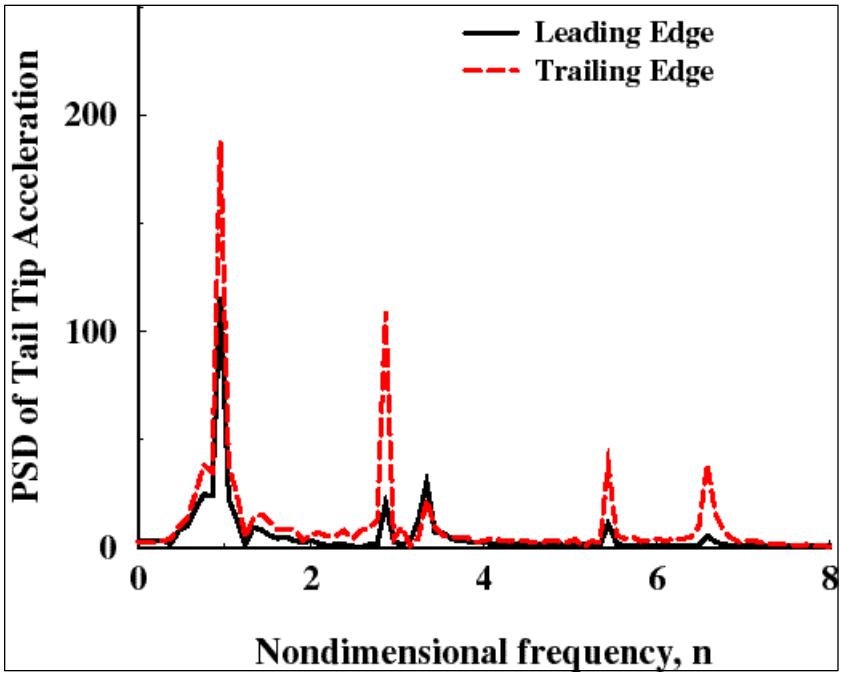

Figure 24. PSD of the Tail Tip Accelerations

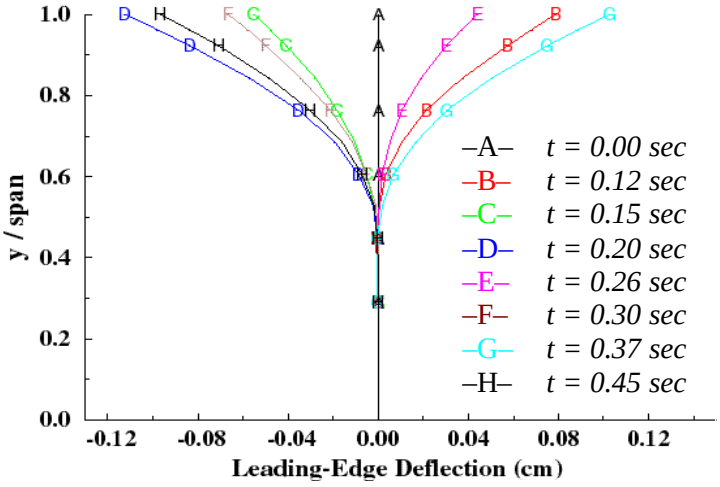

Figure 25. Deflection Distribution Along the Leading Edge of the Tail

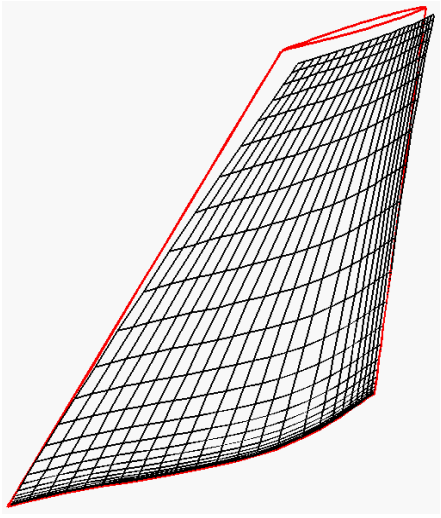

Figure 26. The Deformed Vertical Tail After 0.11 Seconds

4.7 Conclusion

The MDICE Environment was successfully used and validated for the prediction of vertical tail buffeting of F/A18 aircraft. The results indicated that the inboard surface of the vertical tail has more significant contribution in the unsteadiness of the problem than the outboard surface does. The outboard surface pressure of the vertical tail is less sensitive to the angle of attack than to the pressure on the inboard surface. The buffet excitation peaks shift to lower frequencies as the angle of attack increases. The vertical tail of the F/A-18 aircraft is responding mainly in the first bending and torsional modes. The vertical tail is oscillating mainly toward the outboard direction. The computational results were compared, and they are in close agreement with flight and experimental data over the angle of attack range.

5. CONTROL OF F/A-18 TAIL BUFFETING BY VORTICAL BLOWING

5.1 Introduction

In this section, a numerical investigation for the control of vertical tail buffeting of full F/A-18 aircraft using tangential vortical blowing (TVB) is presented. A high-momentum fluid is injected from the upper surface of the LEX of the wing. The fluid is injected tangential to the LEX surface and parallel to the LEX vortex. The injection is aimed at restructuring the vortical flow of the F/A-18 aircraft in order to produce stronger vortices and alleviate the vertical tail buffeting.

The blowing jet tube is assumed over the LEX of the wing, as shown in Figure 27. The physical blowing device is not modeled in this investigation. Only the effect of the blowing jet is considered. The jet is assumed at the footprint of the leading-edge vortex at a longitudinal section defined by the intersection between the wing and the LEX. The jet cross-sectional area is 2.93 in^2. The jet is directed to blow in a direction tangent to the LEX upper surface and parallel to the wing leading-edge vortices.

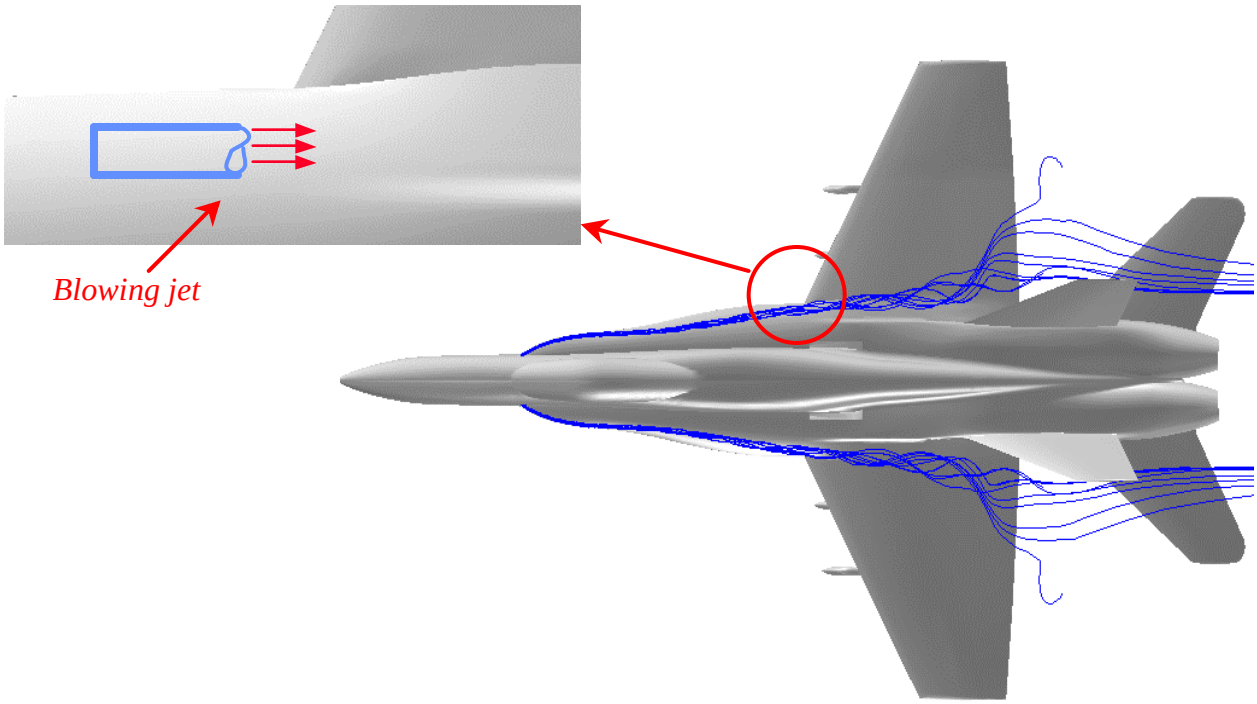

Figure 27. Schematic View Showing the Blowing Jet Over the LEX of the Wing

The jet is simulated numerically by defining a permeable boundary, corresponding to the jet slot, where inlet-flow boundary conditions are implemented. At the jet-exit boundary, the flow density is assumed constant and equals to five times the free-stream density. The pressure is extrapolated from the flow field, and the temperature is assumed fixed at the freestream value. The blowing strength of the jet is prespecified, and the jet exit velocity is computed from the equation of the blowing strength as follows:

$$C_m = \left(m_j V_j\right) / \left(q_\infty S\right), \tag{16}$$

where C_m is the blowing strength, m_j is the jet mass flow rate, V_j is the jet exit velocity, q_∞ is the free-stream dynamic pressure, and S is the wing surface area. The effects of several blowing strength values in the range of 0.01 through 0.05 are investigated.

5.2 Effects of Vortical Blowing on Aerodynamics Flow Field

The effects of TVB on the vortical flow over the F/A-18 aircraft are shown in Figures 28 and 29. The figures show three-dimensional, front, and side view snapshots of the instantaneous streamlines over the aircraft for the no-blowing case and for the case of a blowing strength of 0.04. The figures also show the surface static pressure over the aircraft surfaces. The figures clearly show that the leading-edge vortices break down upstream of the vertical tails and that the tails are emerged in the vortex breakdown flow. In the no-blowing case, the vortical flow exists mainly outboard of the vertical tail. In the blowing case, the vortical flow moves toward the inboard space between the vertical tails. In this case, the tail cuts almost through the center of the vortical flow, which should balance the unsteady differential loads across the tail surfaces.

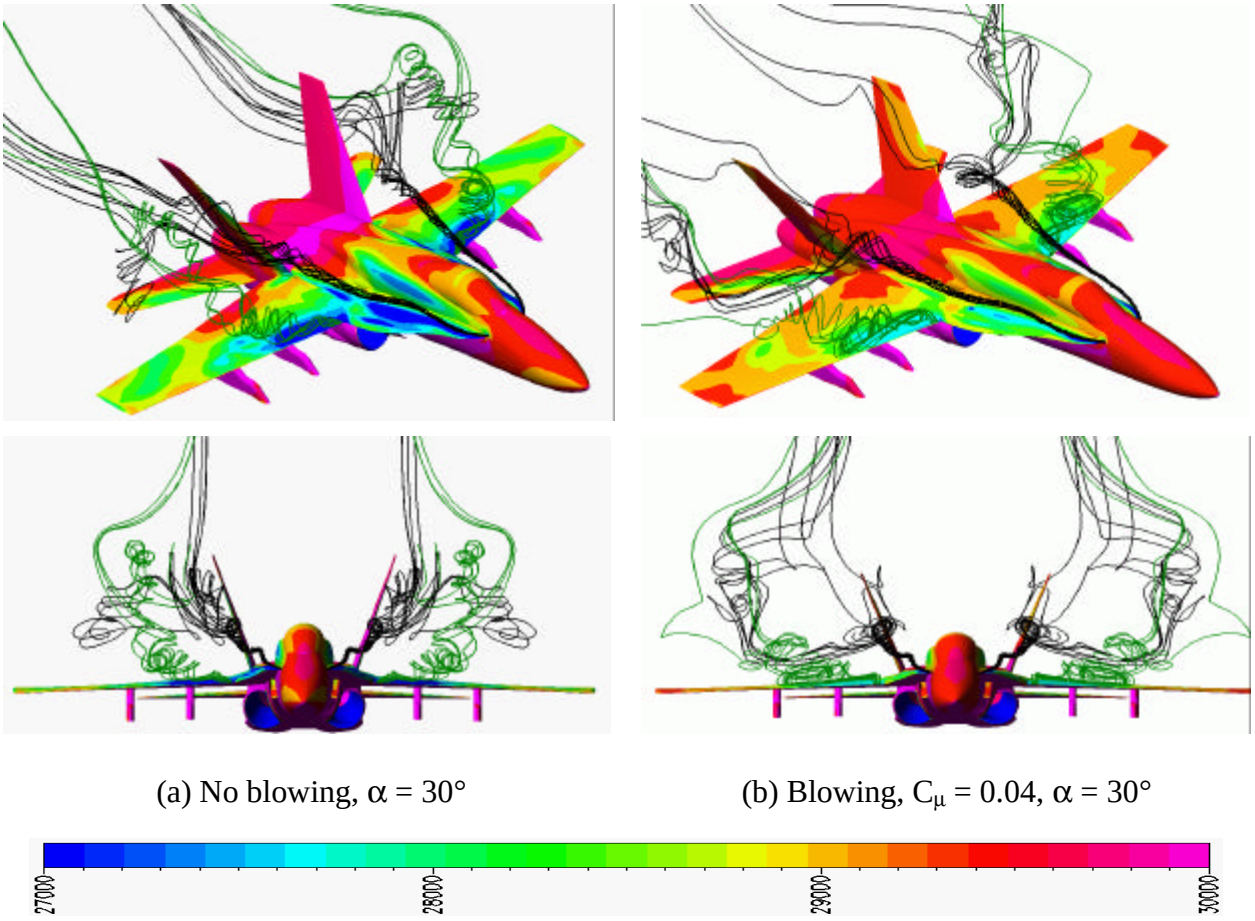

(a) No blowing, $\alpha = 30°$ (b) Blowing, $C_\mu = 0.04$, $\alpha = 30°$

Figure 28. Three-dimensional View and Front View Snapshots of the F/A-18 Aircraft Showing the Instantaneous Streamlines of the LEX and the Wing Leading Edge

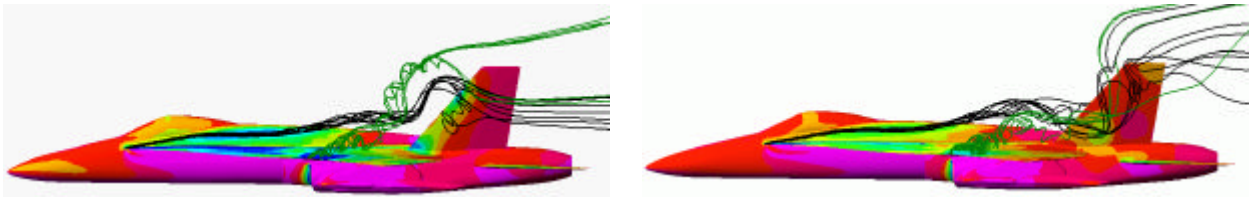

(a) No blowing, $\alpha = 30°$ (b) Blowing, $C_\mu = 0.04$, $\alpha = 30°$

Figure 29. Side View Snapshots of the F/A-18 Aircraft Showing the Instantaneous Streamlines of the LEX and the Wing Leading Edge

5.3 Effects of Vortical Blowing on Unsteady Pressures

The effects of blowing strength on the history of the unsteady differential pressure coefficient and the RMS of the differential pressure are shown in Figures 30 and 31, respectively. The figures show that TVB can effectively be used to reduce the differential pressures (loads) across the vertical tail. This is obviously due to the inboard motion of the vortical flow, which balanced the unsteady pressure across the vertical tail, as observed from Figure 28. The vortical blowing reduced the RMS of the differential pressure by up to 24 percent. The smallest amplitude and RMS of the differential pressure occurred at blowing strength of 0.04. The behavior of the RMS of the pressure with respect to the blowing strength suggests that steady blowing might not be the optimum control methodology. Unsteady blowing or active flow control, using feedback signal from the responses, might have more potential in reducing the unsteady differential pressures and consequently alleviate the tail buffet.

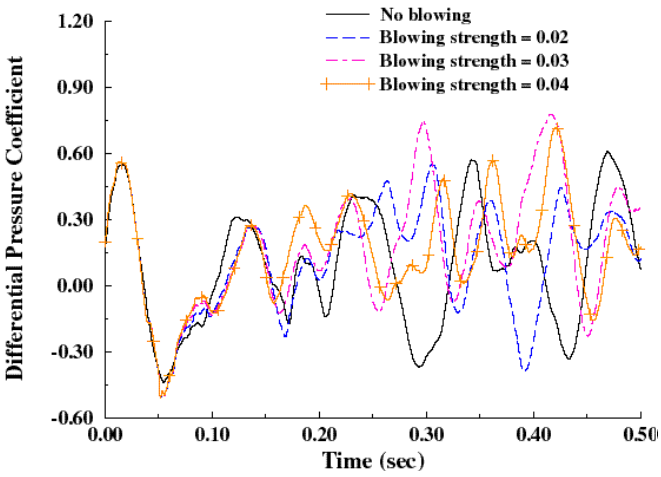

Figure 30. The Time History of the Differential Pressure Coefficient at the 45 Percent Chord, 60 Percent Span Point

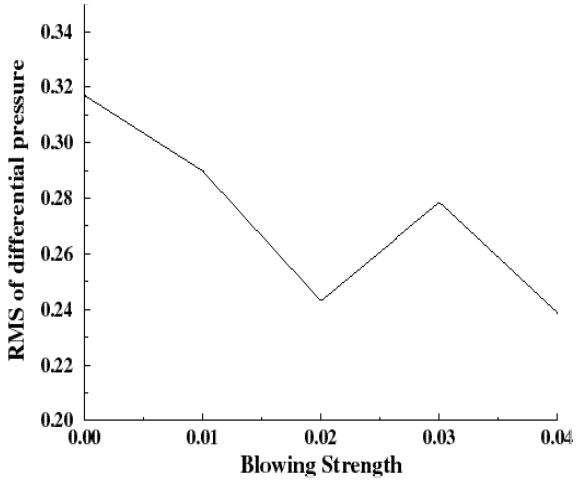

Figure 31. Effect of Blowing Strength on the RMS of Differential Pressure Coefficient

The buffet excitation spectra of the inboard, outboard, and differential pressure coefficient at 45 percent chord and 60 percent span are shown in Figure 32. Figure 32 shows that the vortical blowing has balanced the buffet excitation on the inboard and outboard surfaces of the vertical

tail. This balance led to much lower buffet excitation of the differential pressure than the no-blowing case.

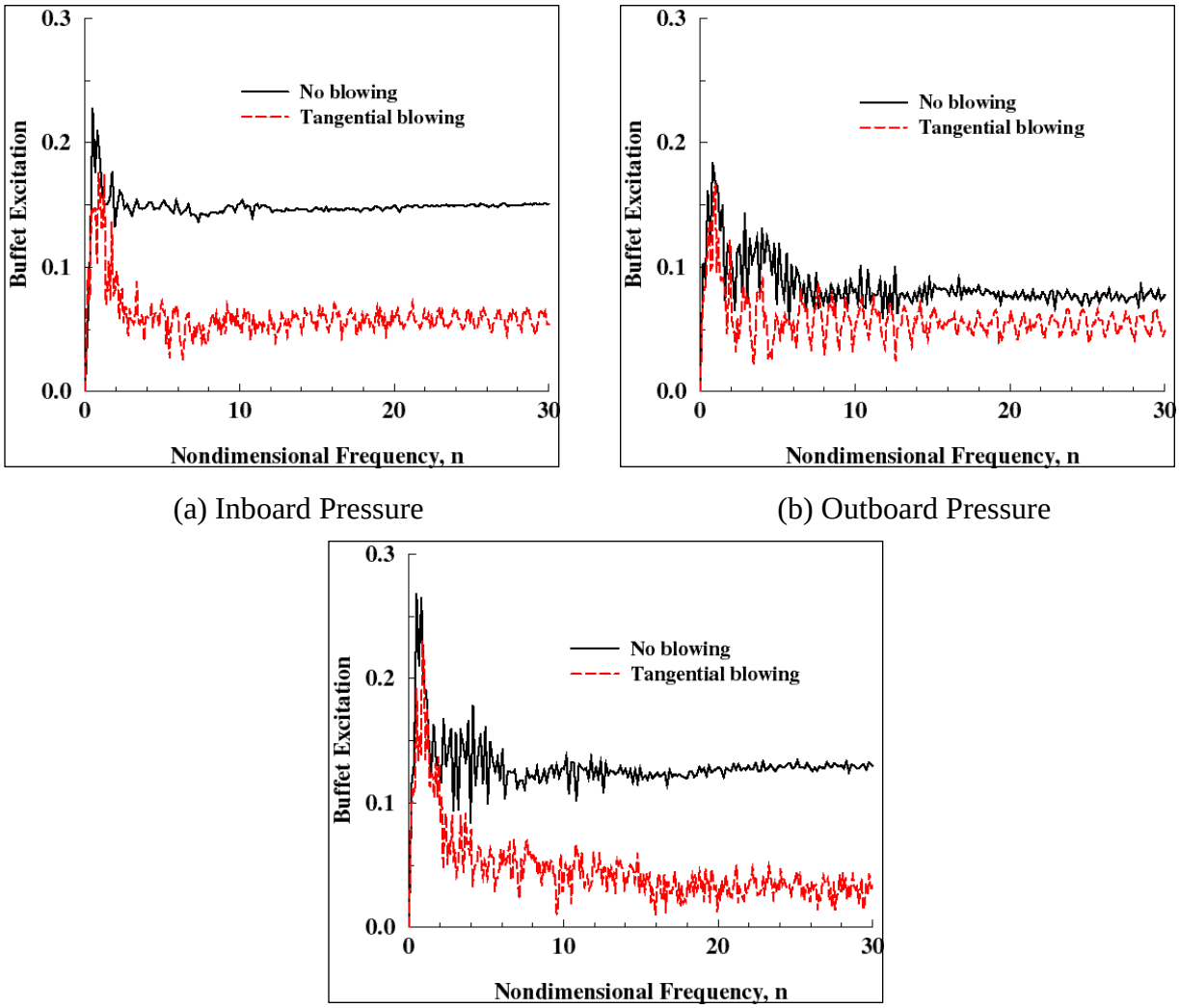

(a) Inboard Pressure

(b) Outboard Pressure

(c) Differential Pressure

Figure 32. Buffet Excitation Spectra of the Inboard, Outboard, and Differential Pressure Coefficient at 45 Percent Chord and 60 Percent Span Point

5.4 Effects of Vortical Blowing on Root Bending Moment

The effects of vortical blowing strength on the history of the root bending moment coefficient and the RMS of the RBM are shown in Figures 33 and 34, respectively. Positive root bending moment indicates moment that is directed outboard. The figures show very interesting behavior. Some values of blowing strength are energizing the vortical flow more than other values of blowing strength, and therefore they lead to lower amplitude and RMS of root bending moment. The vortical blowing reduced the RMS of root bending moment coefficient by up to 13 percent. In the cases considered herein, the cases of blowing strength of 0.2 and 0.4 produced the smallest

amplitude and RMS of RBM. As indicated earlier, more study is needed to optimize the blowing strength based on feedback signal from the responses.

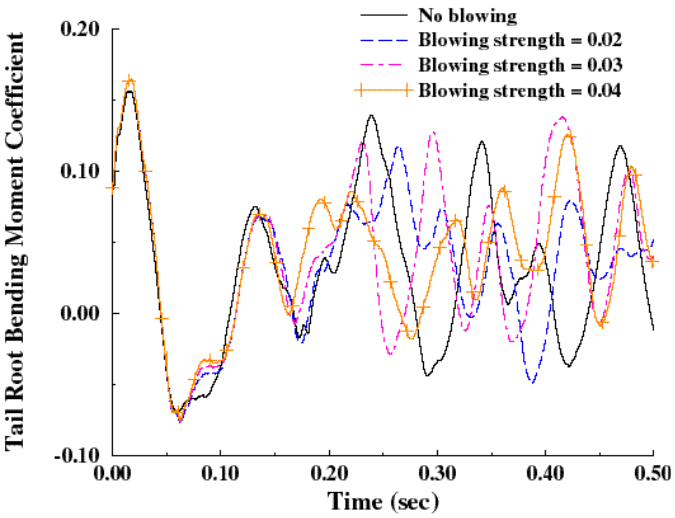

Figure 33. The Time History of the Differential Pressure Coefficient at the 45 Percent Chord, 60 Percent Span Point

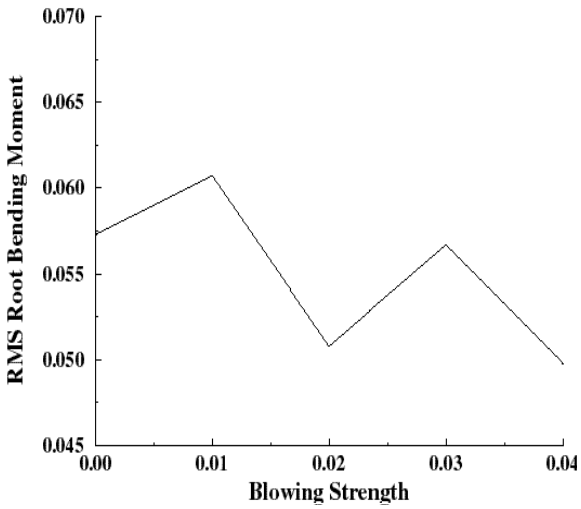

Figure 34. Effect of Blowing Strength on the RMS of Root Bending Moment Coefficient

The effect of TVB on the PSD of the root bending moment is shown in Figure 35. Figure 35 shows that the TVB resulted in about a 23 percent reduction in the peak of the root bending moment. The peaks also shift into slightly higher frequencies.

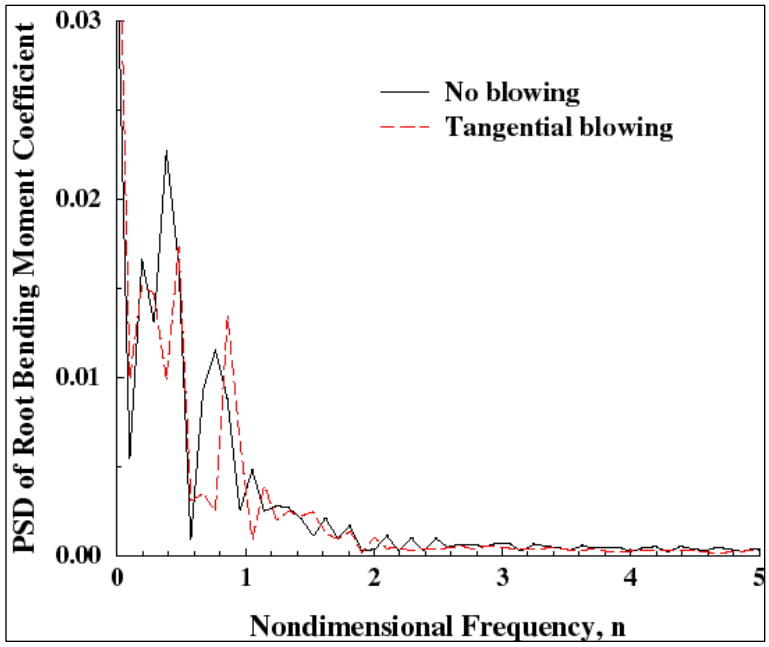

Figure 35. PSD of Vertical Tail Root Bending Moment Coefficient, C_m = 0.04

5.5 Effects of Vortical Blowing on Aeroelastic Responses

The effects of vortical blowing on the time histories of the tail tip deflections are shown in Figure 36. Figure 36 shows the oscillatory nature of the deflection. The vortical blowing produced slight increase in the amplitude of deflection at both the leading edge and trailing edge of the vertical tail. However, the frequency did not change.

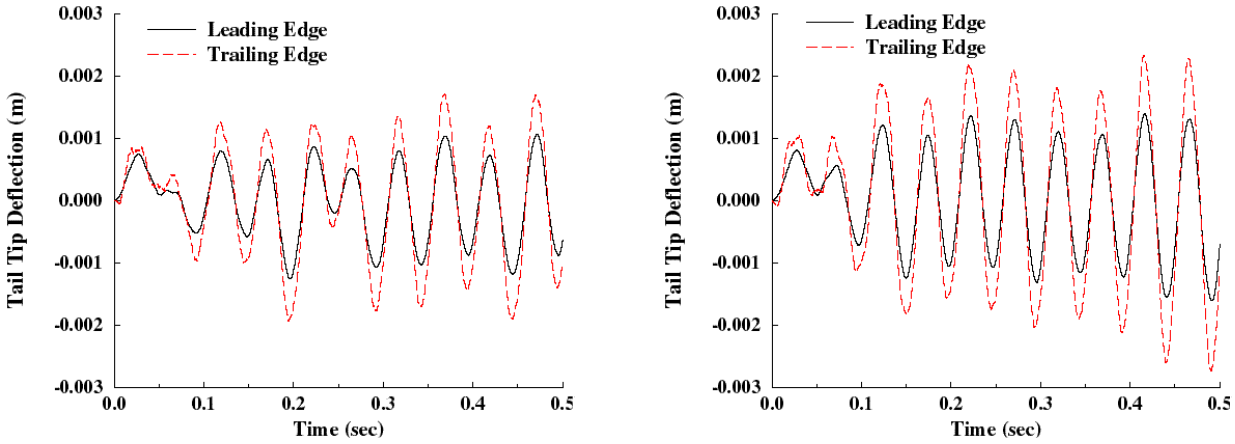

(a) No blowing (b) Blowing, C_μ=0.04

Figure 36. Effect of Blowing on the Time Histories of Tail Tip Deflections

The PSD of the accelerations is computed in the nondimensional form *Z(n)*, where

$$Z(n) = PSD(\ddot{Z}) \cdot (U_\infty / \overline{C}) \tag{17}$$

The effects of vortical blowing on the PSD of the tail tip accelerations are shown in Figure 37. For both cases, Figure 37 shows that the acceleration power at the trailing-edge point is larger than that at the leading-edge point. Figure 37 also shows that the vortical blowing increases the acceleration power at both the first bending and torsion modes. However, it reduces the acceleration power at the second bending mode.

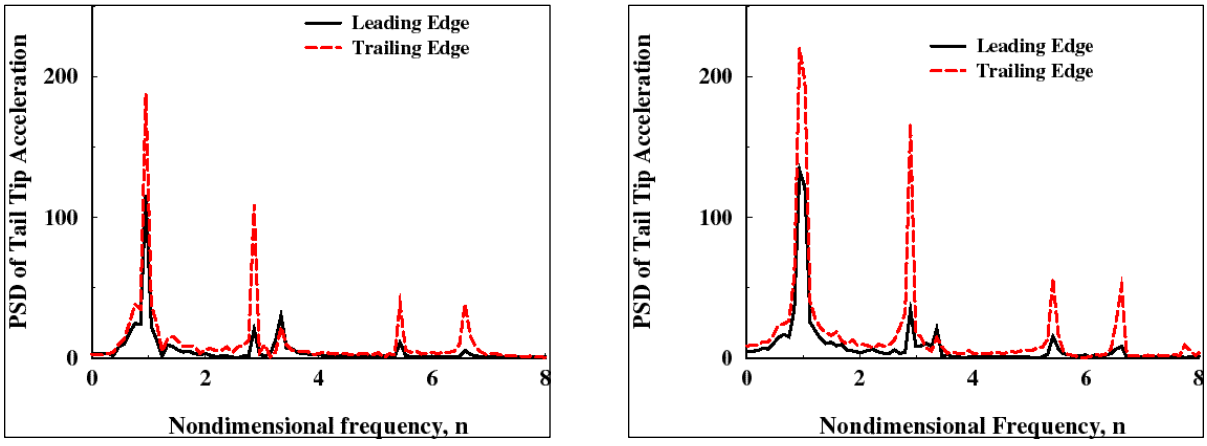

(a) No blowing (b) Blowing, C_μ=0.04

Figure 37. Effect of Vortical Blowing on the PSD of the Tail Tip Accelerations

5.6 Conclusion

A multidisciplinary computational study for the effect of TVB on alleviating the vertical tail buffet of F/A-18 aircraft is conducted. A blowing jet is used over the LEX of the wing to inject high-momentum fluid into the vortical flow over the aircraft. The vortical blowing moved the cores of the LEX vortices toward the inboard direction, which balanced the unsteady pressure on both sides of the vertical tail. This balance resulted in much lower buffet excitation than the no-blowing case. In the range of the blowing strength considered in this investigation, the vortical blowing reduced the RMS of the unsteady differential pressure by up to 24 percent, and reduced the RMS of the RBM by up to 13 percent. The PSD of the RBM was also reduced by up to 23 percent. The response of the vertical tail was dominated by the first bending mode. The vortical blowing increases the acceleration power at the first bending and torsion modes. However, it reduces the acceleration power at the second bending mode.

6. TAIL BUFFETING ALLEVIATION VIA LEX FENCES

6.1 Introduction

The LEX fence represents the other flow control avenue for alleviating the vertical tail buffeting of fighter aircraft. The basic configuration of the F/A-18 aircraft is modified to include streamwise fences. The grid system and size of the modified configuration is the same as that of the basic configuration for fair comparison. The fences were originally designed using trial-and-error procedure. The fences are placed over the upper surface of the wing LEX, near the intersection with the leading edge of the wing. The fence has a trapezoidal shape with edge angles of 30^{o}. The taper ratio of the LEX fence is 0.7 and the thickness of the fence is assumed 0.8 *in*. Figure 38 shows the surface geometry of the modified configuration and the dimensions of the LEX fence. The fences are placed along the path of the primary LEX vortex in order to restructure the vortical flow over the aircraft. It is believed that as the LEX vortex passes over the fence, the vortex separated into two counter-rotating vortices. The two vortices trail downstream and provide some aerodynamic damping on the vertical tail.

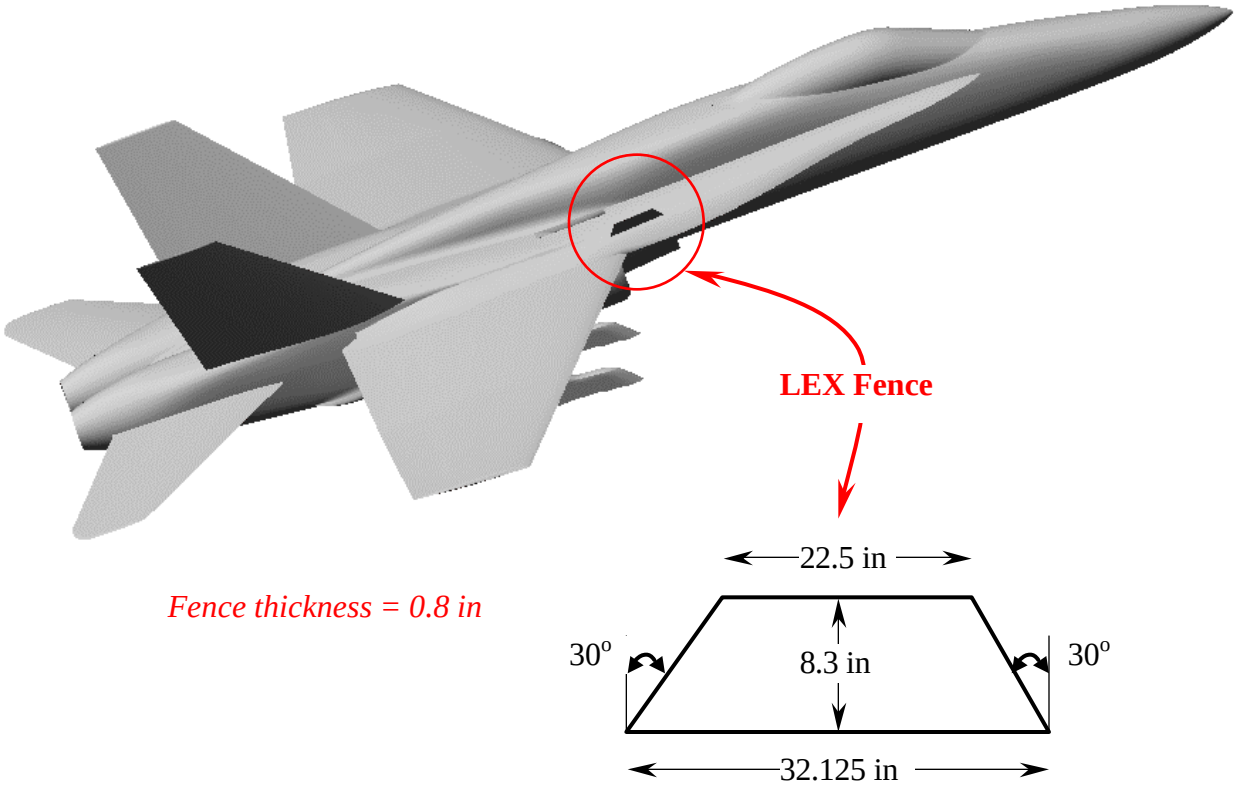

Figure 38. The Modified F/A-18 Configuration and Fence Dimensions

6.2 Effects of LEX Fence on Aerodynamic Flow Field

The effects of the LEX fence on the aerodynamics flow field around the F/A-18 aircraft are shown in Figures 39 and 40. Figure 39 shows three-dimensional and front view snapshots of the F/A-18 aircraft and the instantaneous streamlines of the LEX and wing vortices at $\alpha = 30^{o}$. The figure clearly shows that the fence forced the vortical flow to move inward toward the vertical tail. This inward motion would balance the loads on both sides of the vertical tail in contrast to the fences-off model. In the fences-off model, the vortices were totally outboard the vertical tails. Also shown in the figure, the fences delayed the vortex breakdown location.

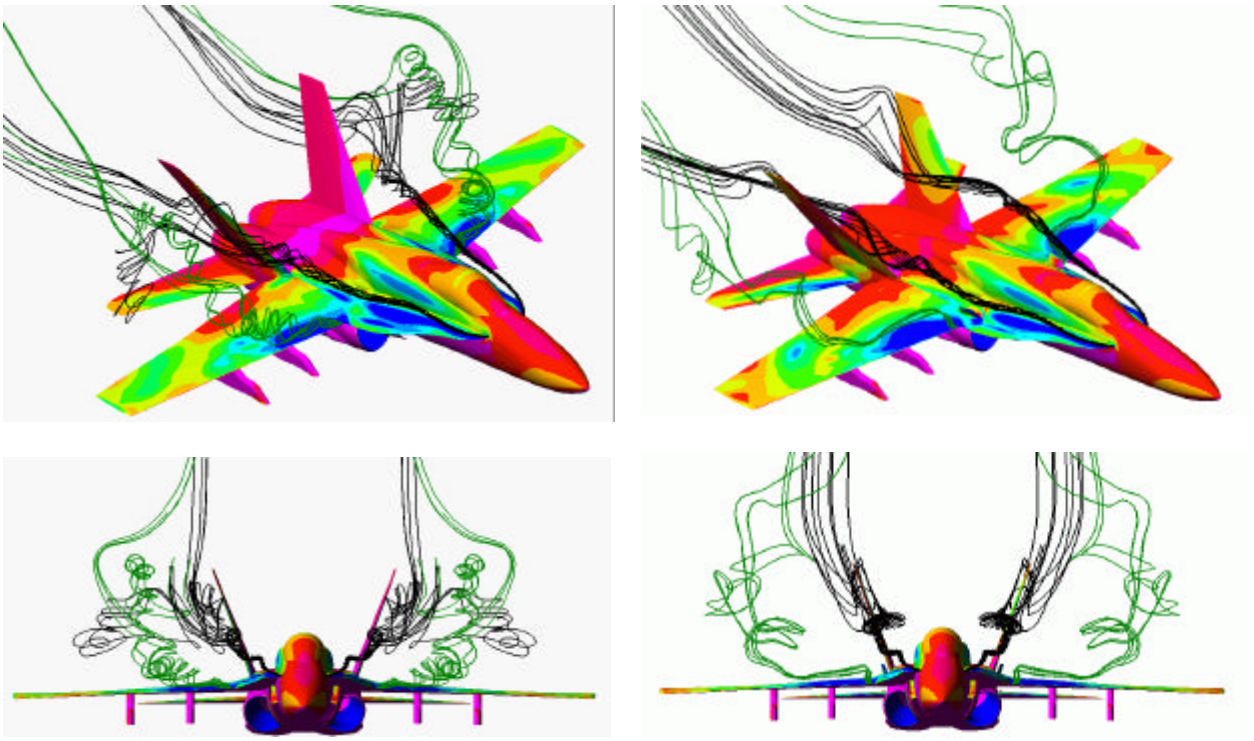

(a) Fences off ($\alpha = 30°$) (b) Fences on ($\alpha = 30°$)

Figure 39. Three-dimensional and Front Views of the F/A-18 Aircraft Showing the Instantaneous Streamlines of the LEX and the Wing Leading Edge

The total pressure contours on crossflow planes over the F/A-18 aircraft at different longitudinal locations are shown in Figure 40. Figure 40 shows that as the vortical flow crosses the fences, the LEX vortex splits into two co-rotating vortices. Once the vortices pass the fences, they start to move in a spiral path over each other. Thereafter, they merge together, producing a larger vortex. This means that the energy of the vortex is spread over a larger region than that of the basic configuration. The vortex split and merge increases the axial momentum of the LEX vortex, which results in a delay in the vortex breakdown location, as shown in Figure 39.

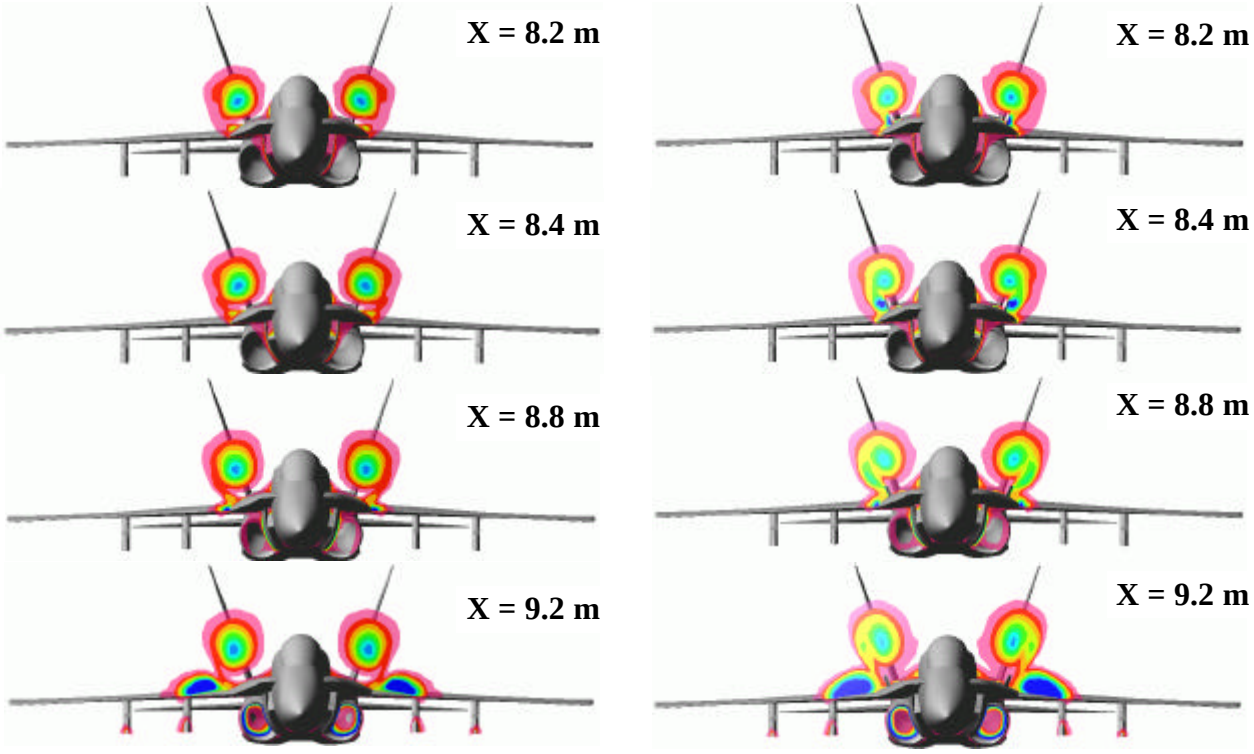

(a) Fences off ($\alpha = 30^o$) (b) Fences on ($\alpha = 30^o$)

Figure 40. Total Pressure Contours on Crossflow Planes Over the F/A-18 Aircraft

6.3 Effects of LEX Fence on the Aeroelastic Characteristics

The effects of the LEX fence on the RMS of inboard, outboard, and differential pressure coefficients are shown in Figure 41. Figure 41 shows the fences-off and fences-on results. The results are compared with flight test data and full-scale, 16-percent-scale, and 6-percent-scale wind tunnel data (see Meyn et al. 1994). The results compared well with the experimental and flight data for both the fences-off and fences-on configurations. The results clearly show that the LEX fence reduces the RMS pressure on the inboard surface of the tail. This, in turn, resulted in reducing the differential pressure on the vertical tail. For both configurations, the RMS pressure of the inboard surface is larger than that of the outboard surface. The RMS pressure of the outboard surface is less sensitive to the angle of attack. The results indicate that the fences-off configuration experiences the maximum peaks around the 30^o angle of attack. For the fences-on configuration, the maximum peaks occur around the 35^o angle of attack. This shows that the LEX fence shifts the onset of maximum tail buffet to higher angles of attack, in agreement with the experimental data of James and Meyn (1994).

The buffet excitation spectra of the F/A-18 vertical tail are computed over the angle of attack range. The predominant frequencies of the buffet pressure peaks are shown in Figure 42 for the inboard, outboard, and differential pressures. The results compared well with the flight and experimental data for both the fences-off and fences-on configurations. For both configurations, the buffet excitation peaks shift into lower frequencies as the angle of attack increases.

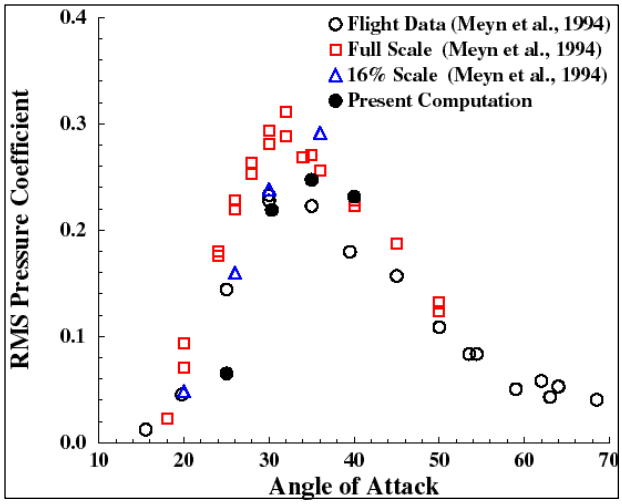

(a) Inboard Pressure, no LEX Fence

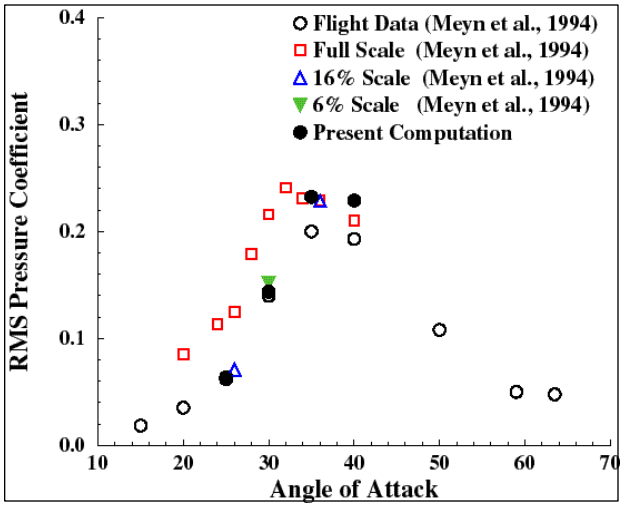

(a) Inboard Pressure, with LEX Fence

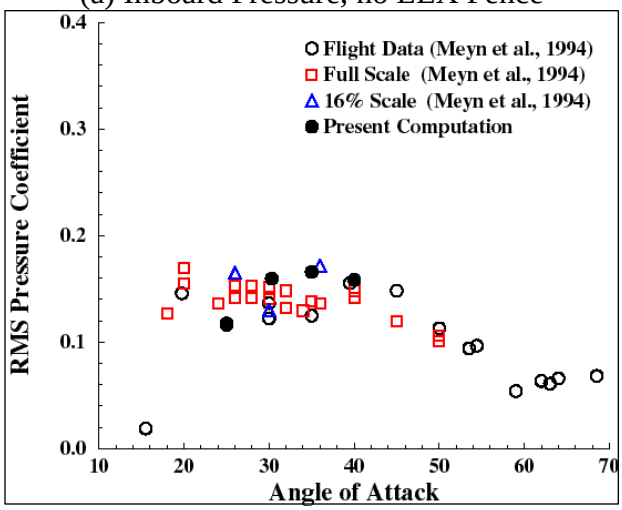

(b) Outboard Pressure, no LEX Fence

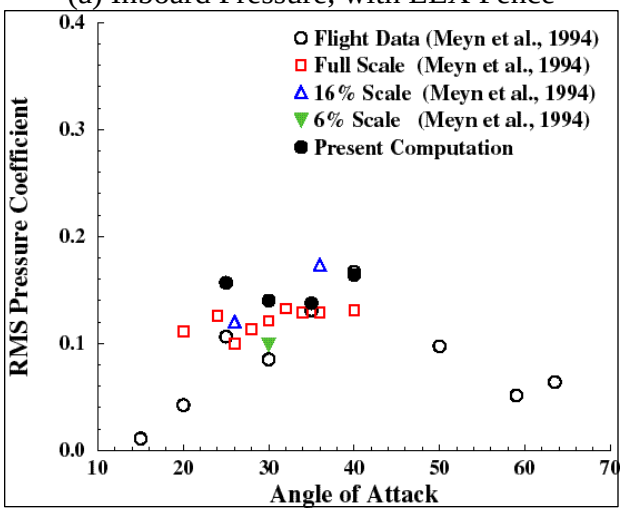

(b) Outboard Pressure, with LEX Fence

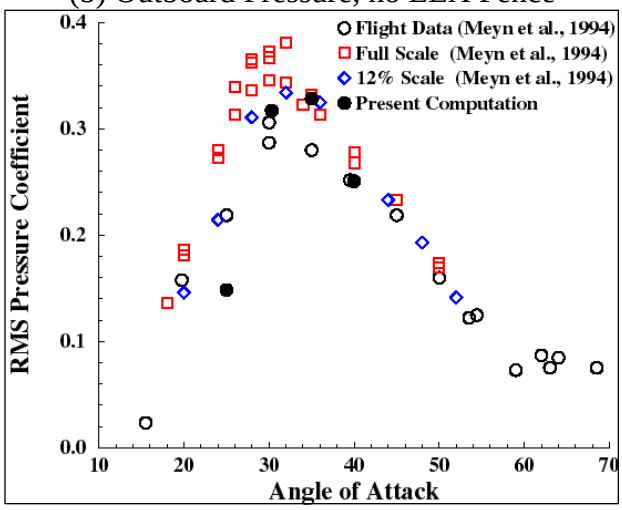

(c) Differential Pressure, no LEX Fence

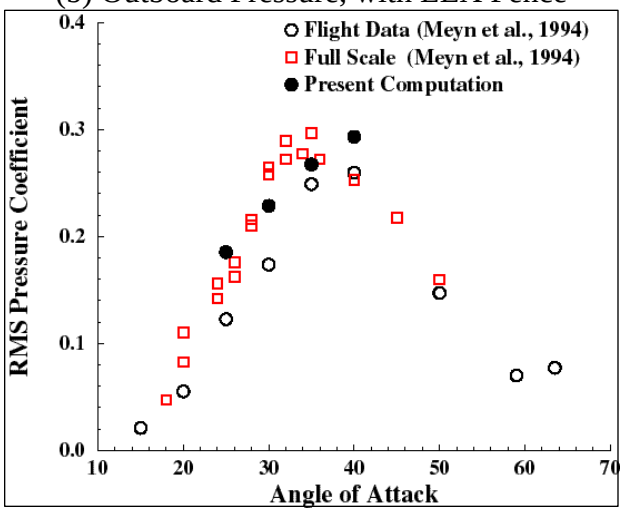

(c) Differential Pressure, with LEX Fence

Figure 41. RMS Pressure Coefficient at 45 Percent Chord and 60 Percent Span of the Tail

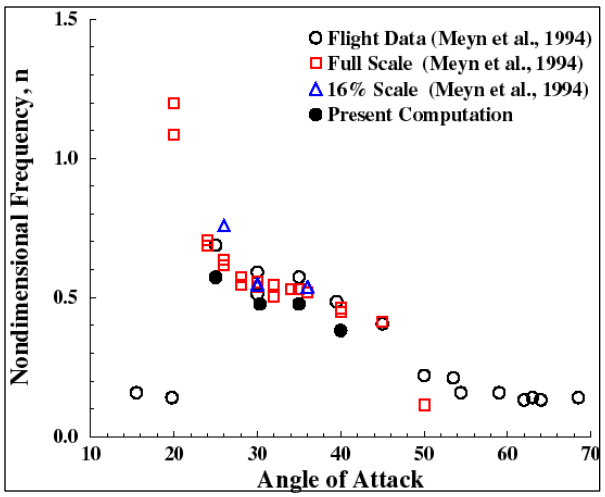

(a) Inboard Pressure, no LEX Fence

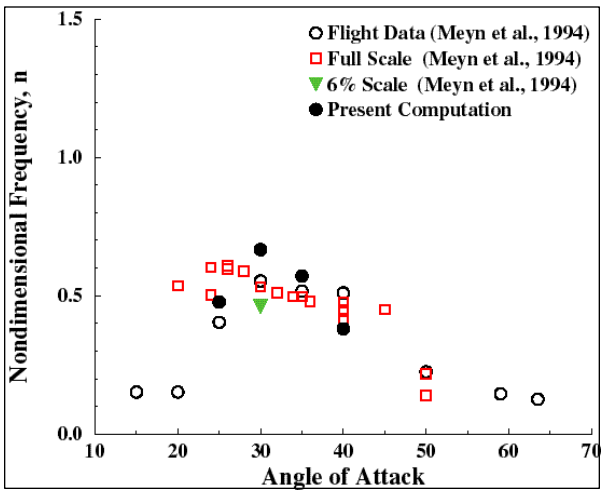

(a) Inboard Pressure, with LEX Fence

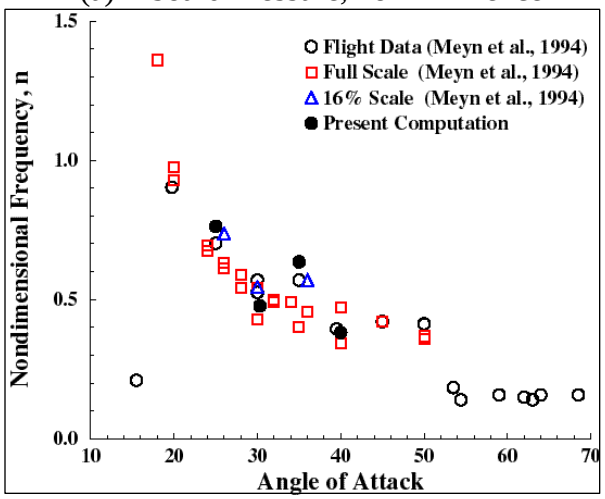

(b) Outboard Pressure, no LEX Fence

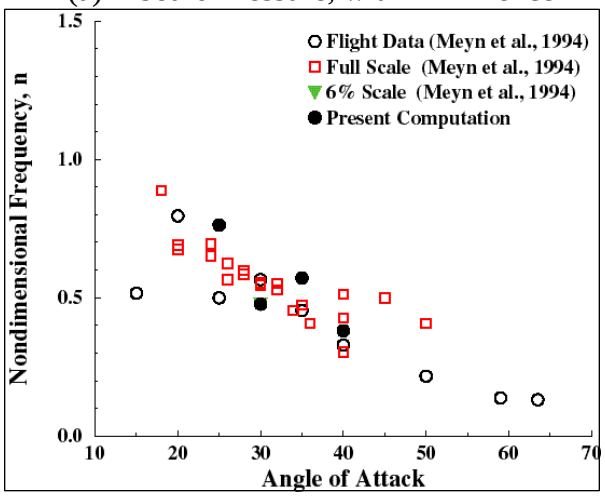

(b) Outboard Pressure, with LEX Fence

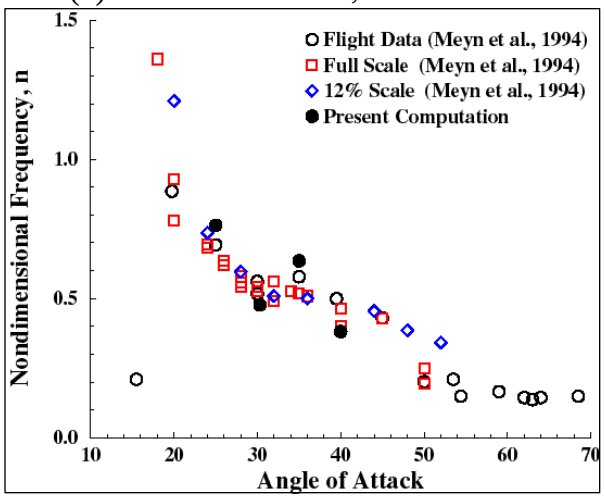

(c) Differential Pressure, no LEX Fence

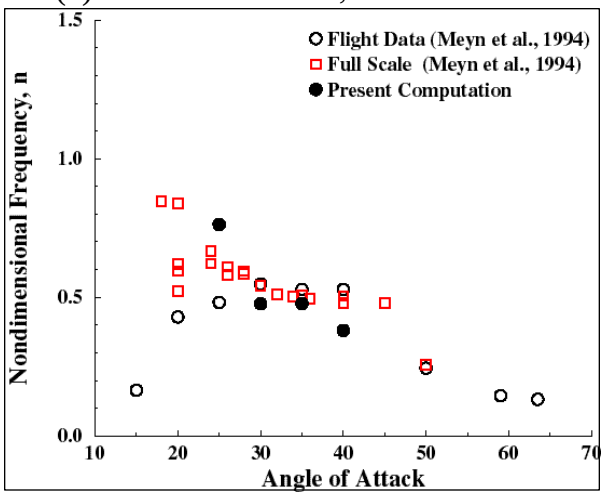

(c) Differential Pressure, with LEX Fence

Figure 42. Predominant Frequencies of the Buffet Pressure Peaks

The peaks of the power spectra of the differential pressure coefficient are compared with the flight data and experimental data for the fences-off and fences-on configurations in Figure 43. The figure clearly shows that the LEX fence reduces the peak power of the differential pressure. This is the main effect of the LEX fence. The figure also shows that the maximum buffet power shift into higher angle of attack with the use of LEX fence. The computed results compared well with the flight and experimental data for both configurations.

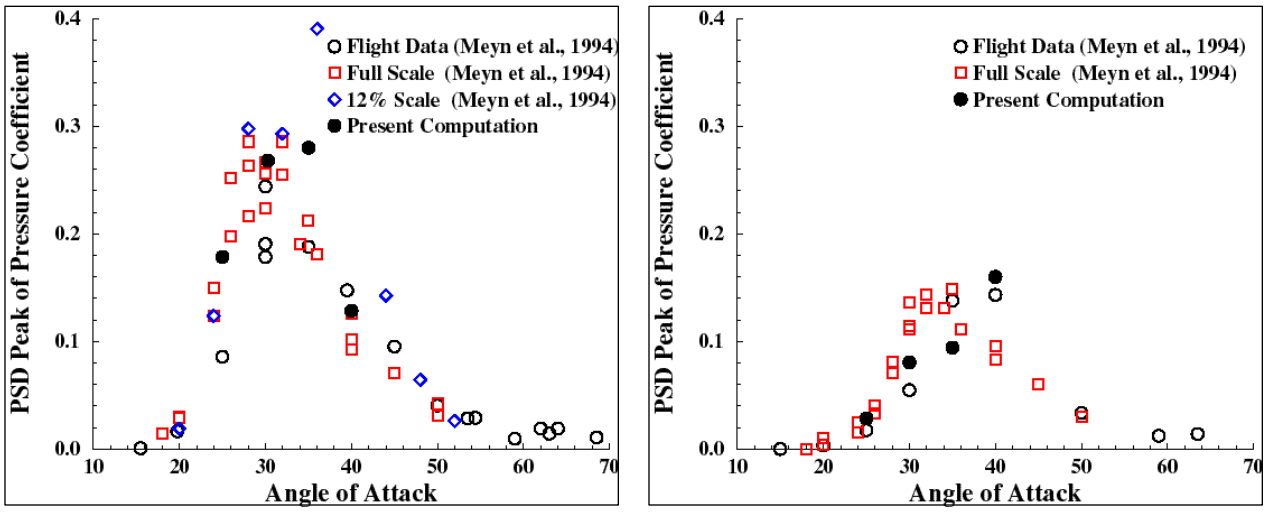

(a) no LEX Fence (b) with LEX Fence

Figure 43. PSD Peak of Differential Pressure Coefficient at 45 Percent Chord and 60 Percent Span

The RMS of the tail root bending moment coefficient for the fences-off and fences-on configurations is shown in Figure 44. The results compare well with the experimental data over the angle of attack range for both configurations. The LEX fence configuration produced maximum root bending moment (RBM) at an angle of attack of 35^{o} in contrast to the basic configuration where maximum RBM occurs at an angle of attack of 30^{o}. This emphasizes the conclusion that the LEX fences shift the maximum buffet conditions into higher angles of attack. Figures 41-44 show an interesting characteristic of the F/A-18 aircraft with LEX fences. The RMS of buffet pressure, peaks of power spectral density of buffet pressure, and the RBM at an angle of attack of 40^{o} are all higher than those of the basic configuration. This shows that the effectiveness of the LEX fences reduce at higher angles of attack. This conclusion is in agreement with the experimental observations of Shah (1991) and the flight test observations of Lee et al. (1990).

The time histories of the normal deflection at the leading edge and trailing edge of the vertical tail tip are shown in Figure 45. Figure 45 shows the results for both the fences-off and fences-on configurations at 30^{o} angle of attack. The figure clearly shows that the fences reduced the amplitude of deflection at both edges. The different levels of deflection between the leading edge and trailing edge of the vertical tail are indication of the torsional deformation of the vertical tail.

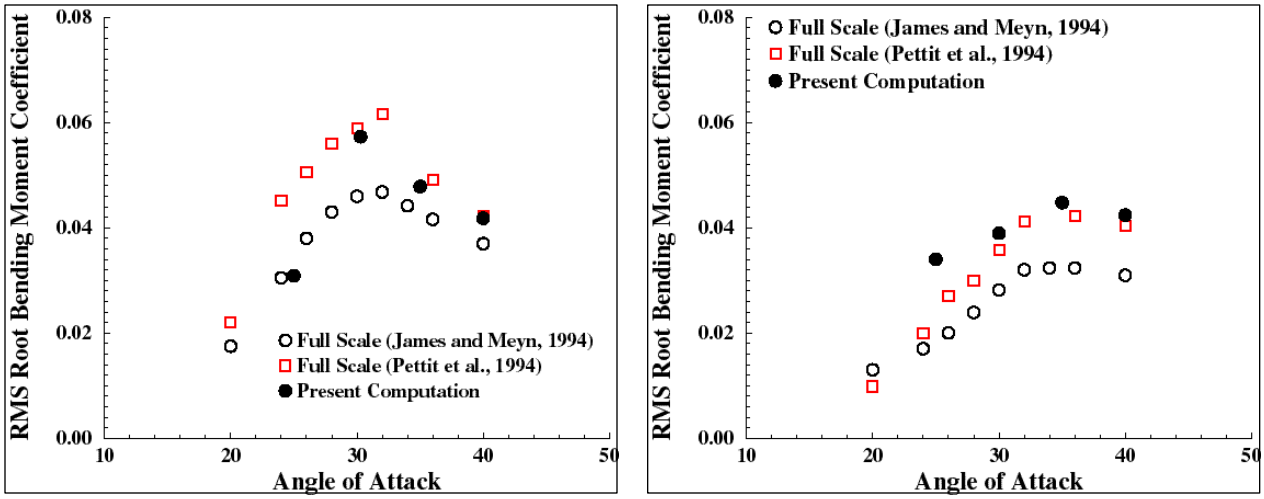

(a) no LEX Fence (b) with LEX Fence

Figure 44. RMS of the Tail Root Bending Moment Coefficient

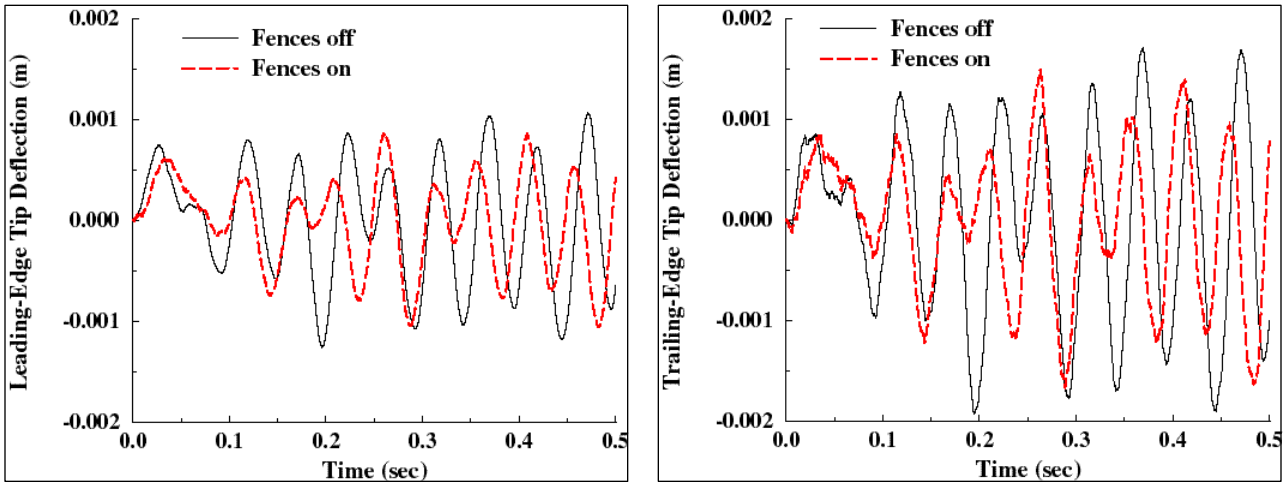

Figure 45. Normal Deflection of the Leading Edge and Trailing Edge of the Vertical Tail Tip

The PSD of the tail tip acceleration of the vertical tail is shown in Figure 46 for the leading edge and trailing edge points. Figure 46 shows that the use of LEX fences reduces the acceleration powers at both the leading and trailing edge points. At the leading edge point, the acceleration power reduced by about 38 percent at the first bending mode, 24 percent at the first torsion mode, and 18 percent at the second bending mode. At the trailing edge point, the acceleration power reduced by about 36 percent at the first bending mode, 7 percent at the first torsion mode, and 24 percent at the second bending mode. Figure 46 also shows that the trailing edge of the vertical tail experiences higher acceleration power than the leading edge.

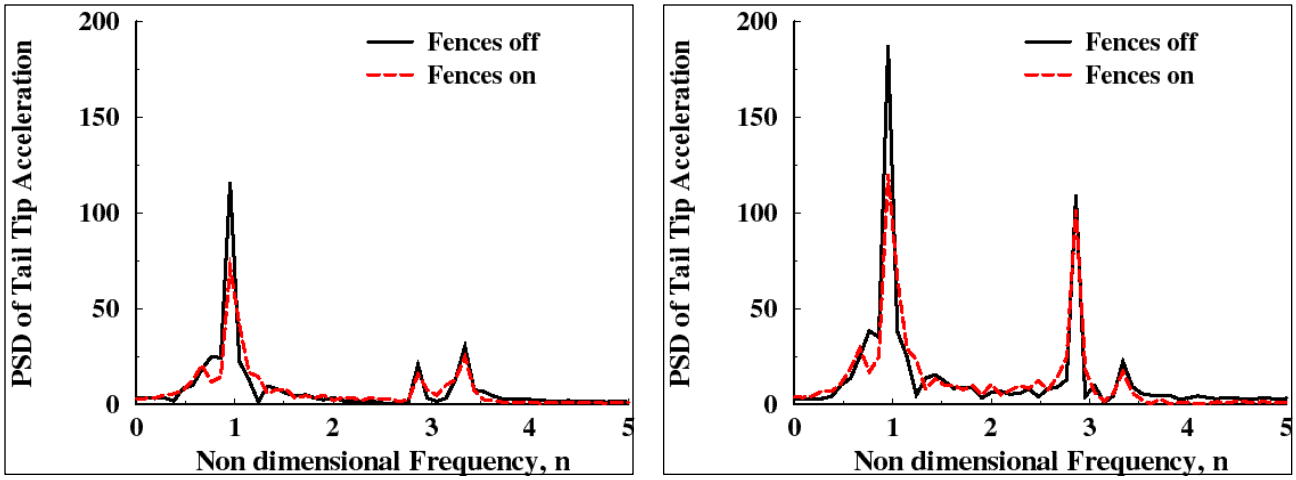

(a) Leading Edge (b) Trailing Edge

Figure 46. PSD of the Vertical Tail Tip Acceleration

6.4 Conclusion

A multidisciplinary computational investigation of tail buffeting alleviation using LEX fence is conducted and presented. The computational results are compared with several flight and experimental data over wide range of high angles of attack. The results show that the LEX fences are effective in reducing the RMS of differential pressure and root bending moment of the vertical tail. The LEX fence shifts the power peak of the buffet pressure, root-mean-square of the buffet pressure, and the root bending moment into higher angle of attack, which is the main objective of the LEX fence. The LEX fences were also effective in reducing the amplitude of deflections of the vertical tail. The acceleration powers of the vertical tail tip were reduced by up to 38 percent at 30^{o} angle of attack. However, the effectiveness of the LEX fences for buffet alleviation reduced for very high angles of attack.

7. ACTIVE STRUCTURAL CONTROL OF TAIL BUFFETING

7.1 Introduction

Multidisciplinary capabilities for active strengthening of the vertical tail structure for tail buffeting alleviation have been developed and integrated with the MDICE environment. The details of the capabilities and demonstration results are presented in this part of the study. Active strengthening of the vertical tail is achieved by attaching a series of piezoelectric (PZT) actuators to the tail structure. The use of the PZT actuators for active structure control and buffet alleviation has been the main focus of the Actively Controlled Response of Buffet-Affected Tails (ACROBAT) program at NASA Langley research center (see Moses 1998). The use of smart materials, such as piezoceramics, gives an actuation system that is independent from the flight control system (in contrast to the method of active rudder). It also has the ability of structural actuation over larger frequency band. The method of active rudder, in contrast, is restricted to the frequency band of the rudder (Moses 1997).

The PZT actuators were distributed over the inboard and outboard surfaces of the vertical tail, as shown in Figure 47. The PZT patches near the root of the tail are out-of-phase to increase control authority in the first bending mode. The PZT patches near the tail tip are in-phase in order to increase control authority in the torsional mode. Each set of PZT actuators on both sides of the tail is being commanded by a control law to strain in opposite directions simultaneously to enable the vertical tail to bend.

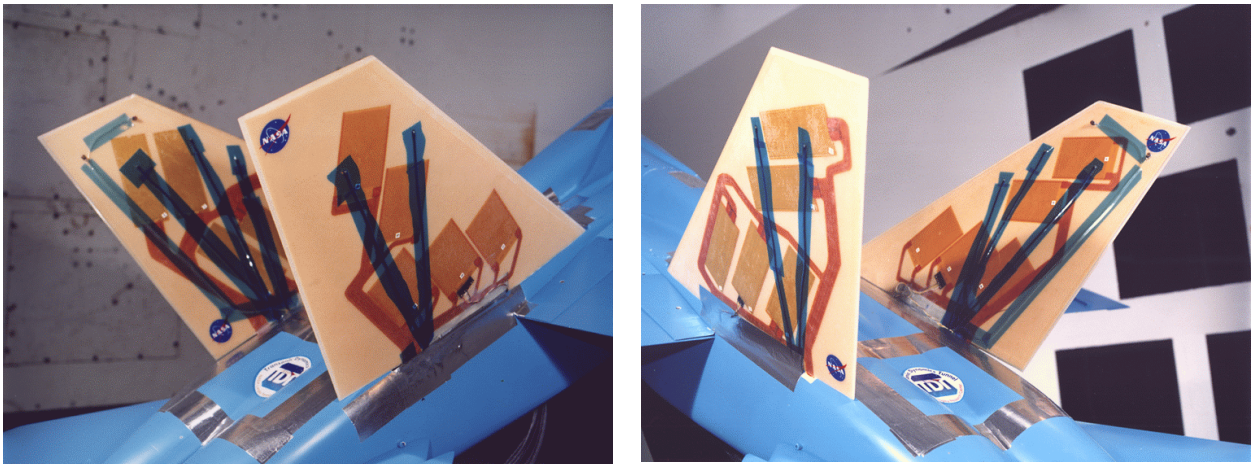

Figure 47. F/A-18 Vertical Tail with Embedded Actuators
(Images are Courtesy of NASA Langley)

7.2 Finite-Element Implementation of PZT Actuators

Piezoelectricity (Greek for pressure electricity) is a property of materials that generate an electrical charge when the materials are subject to material strain, and conversely, piezoelectric materials deform when they are subject to an electrical field. A piezoceramic is therefore capable of acting as either a sensor or actuator. Piezoceramics can be used for control of vibrations by staking them where excessive vibrations occur. The strain of the structure is fed into a controller

that injects voltage into the PZT patches. The mechanical response of the PZT patches due to the input voltage injects vibrations into the structure, which is equivalent and opposite to the initially detected one such that the net vibration becomes minimum. Piezoelectric materials combine the constitutive equations of solids and dielectric materials into one coupled equation. The linear piezoelectric constitutive law (*in Strain-Charge form*) is given by

$$\{S\} = [s_E]\{T\} + [d]^T \{E\} \tag{18}$$

$$\{D\} = [d]\{T\} + [e_T]\{E\}, \tag{19}$$

where $[s_E]$ is the compliance matrix, $[d]$ is piezoelectric coupling matrix, $[e_T]$ is the dielectric constant matrix (permittivity components), $\{S\}$ is the strain vector, $\{T\}$ is the stress vector, $\{D\}$ is the charge density vector, and $\{E\}$ is the electric field vector.

Equation (18) is the sensor equation, which relates the charge developed in the piezoelectric material due to the stresses or strains. Equation (19) is the actuator equation, which relates the applied electric field to the strain developed in the material.

The electric field components, E_k, are related to the electrostatic potential f by the relations:

$$E_k = -\nabla_k j \qquad k = 1, 2, 3 \tag{20}$$

Comparing the equations of motion of the piezoceramics (Equations 18 and 19) with the standard solid equations, where $d_{ki} = 0$, the difference in the finite-element implementation lies at the following:

1. Solving for an additional variable, the electrostatic potential f.
2. Modify the constitutive equation of the structure by adding the term $d_{ki}E_k$. The additional term equals to zero for standard structure patches, and equals nonzero for the patches of piezoelectric material.

When the variational principle is applied to both the piezoelectric equations and the equations of the solid structure, the linear dynamic equations of the coupled system reduce to the following system of equations:

$$\begin{bmatrix} M_{uu} & 0 \\ 0 & 0 \end{bmatrix} \begin{Bmatrix} \ddot{u} \\ \ddot{j} \end{Bmatrix} + \begin{bmatrix} K_{uu} & K_{uj} \\ Kju & -K_{jj} \end{bmatrix} \begin{Bmatrix} u \\ j \end{Bmatrix} = \begin{Bmatrix} F \\ G \end{Bmatrix}, \tag{21}$$

where u, f, F, and G are the global nodal displacement, electric potential, force, and applied charge vectors, respectively. M_{uu} and K_{uu} are the standard mass and stiffness matrices of the original structure. K_{uf} represents the coupled stiffness between electrical field and elastic strain, and K_{ff} represents the stiffness matrix of the piezoelectric material. The stiffness matrices are given as follows:

$$\left[K_{uj}\right]_{el} = \int_{V_{el}} B_u^T e B_j \, dV \tag{22}$$

$$\left[K_{jj}\right]_{el} = \int_{V_{el}} B_j^T e B_j \, dV \tag{23}$$

$$B_u = \left[L_u \quad N_u\right] \qquad B_j = \left[\nabla N_j\right], \tag{24}$$

where N_u and N_f are the shape function matrices for the displacement and electric fields.

If augmented entities are defined for the global displacement field, mass matrix, stiffness matrix, and applied forces as follows:

$$\tilde{u} = \begin{Bmatrix} u \\ j \end{Bmatrix}, \qquad \tilde{M} = \begin{bmatrix} M_{uu} & o \\ o & o \end{bmatrix}, \qquad \tilde{K} = \begin{bmatrix} K_{uu} & K_{uj} \\ K_{ju} & -K_{jj} \end{bmatrix}, \qquad \tilde{F} = \begin{Bmatrix} F \\ G \end{Bmatrix}, \tag{25}$$

then, Equation (24) may be written as

$$M\ddot{\tilde{u}} + \tilde{K}\tilde{u} = \tilde{F}, \tag{26}$$

which is the same equation that any finite-element module is solving. In this case, the modifications of the solid finite-element module become as follows:

1. Introduce additional nodal dependent variable f.
2. Modify mass and stiffness matrix accordingly.

7.3 The Aeroservoelastic Model

An aeroservoelastic model of the F/A-18 vertical tail has been modeled to simulate the effectiveness of the PZT for buffet alleviation. The material properties of the vertical tail structure has been adjusted to produce the same natural frequencies of the 1/6th model of the F/A-18 aircraft that have been tested at NASA Langley under the ACROBAT program. The natural frequencies of this model are given in Table 2.

Table 2. Natural Frequencies of the Aeroservoelastic Model of F/A-18 Vertical Tail

Structural Modes	Natural Frequencies
First bending	44 Hz
First torsion	134 Hz
Second bending	157 Hz

The inboard and outboard surfaces of the aeroservoelastic model of the F/A-18 vertical tail are shown in Figure 48. A total of five PZT actuators are shown on every side of the vertical tail. The root PZT actuators (3 per side) were strategically located near the tail root to alleviate the buffeting in the first bending mode (see Moses et al. 2001). The tip PZT actuators (2 per side) were located near the tail tip to alleviate the buffeting in the first torsion mode. The two stacks of actuators on both sides of the tail are set in an opposite phase to each other to generate bending and torsion. In other words, when one side of the tail is contracting the other side of the tail is expanding to generate either bending or torsion. The acceleration at a near-tip point (75 percent span and 80 percent chord) is recorded and used as the input signal of the control law. An alternative aeroservoelastic model of the F/A-18 vertical tail is shown in Figure 49. In this model, smaller-size PZT patches (48 per side) were distributed over the inboard and outboard surfaces of the vertical tail model. The two models have been used in this study.

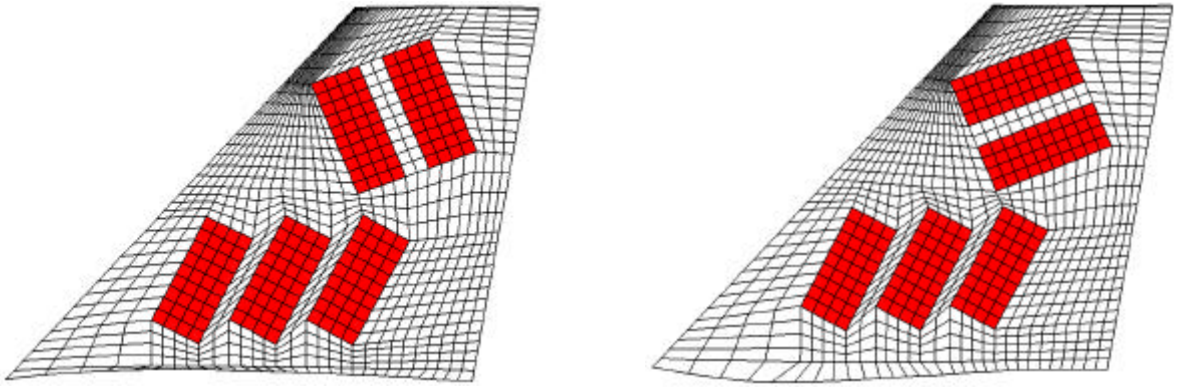

(a) Inboard surface (b) Outboard surface

Figure 48. Aeroservoelastic Model of the F/A-18 Vertical Tail

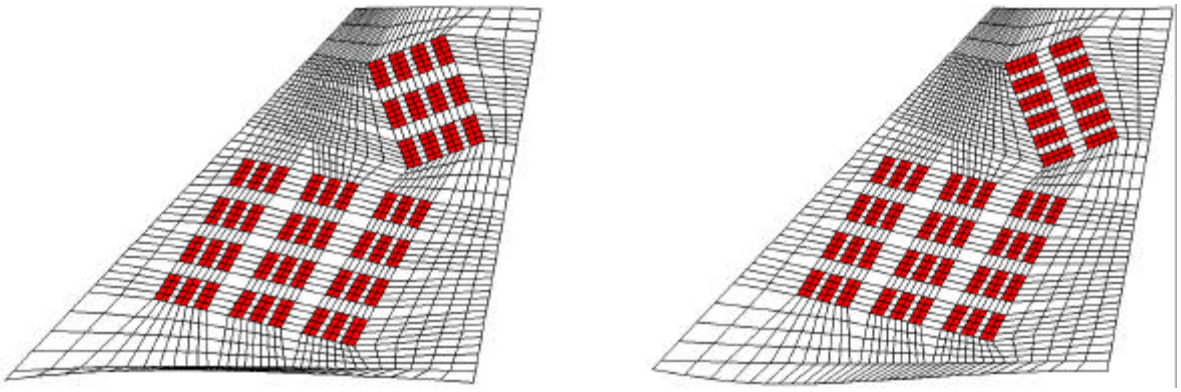

(a) Inboard surface *(b) Outboard surface*

Figure 49. An Alternative Aeroservoelastic Model of the F/A-18 Vertical Tail

The ceramic PZT patches used in the current study are assumed to act similarly to the Active Fiber Composites (AFC), see Moses et al. (2001). The PZT fibers (PZT-5A) of the AFC are transversely aligned in order to sense and actuate in-plane stresses and strains for structural actuation. The material properties of the PZT patches are given in Table 3.

Table 3. Summary of Material Properties of the PZT Patches

Density	ρ	3790 Kg/m^3
Compliance matrix elements	s_{11}^E s_{13}^E s_{33}^E	60 E-12 m^2/N -11 E-12 m^2/N 40 E-12 m^2/N
Piezoelectric constant	d_{33} d_{31}	374 E-12 m/V -48 E-12 m/V
Relative permittivity	K_{33}	495

7.4 The Control Law

The block diagram of the active control system used for tail buffet alleviation is shown in Figure 50. The control law is single-input/single-output and utilizes the tail tip acceleration as the sensor to alleviate the buffeting response.

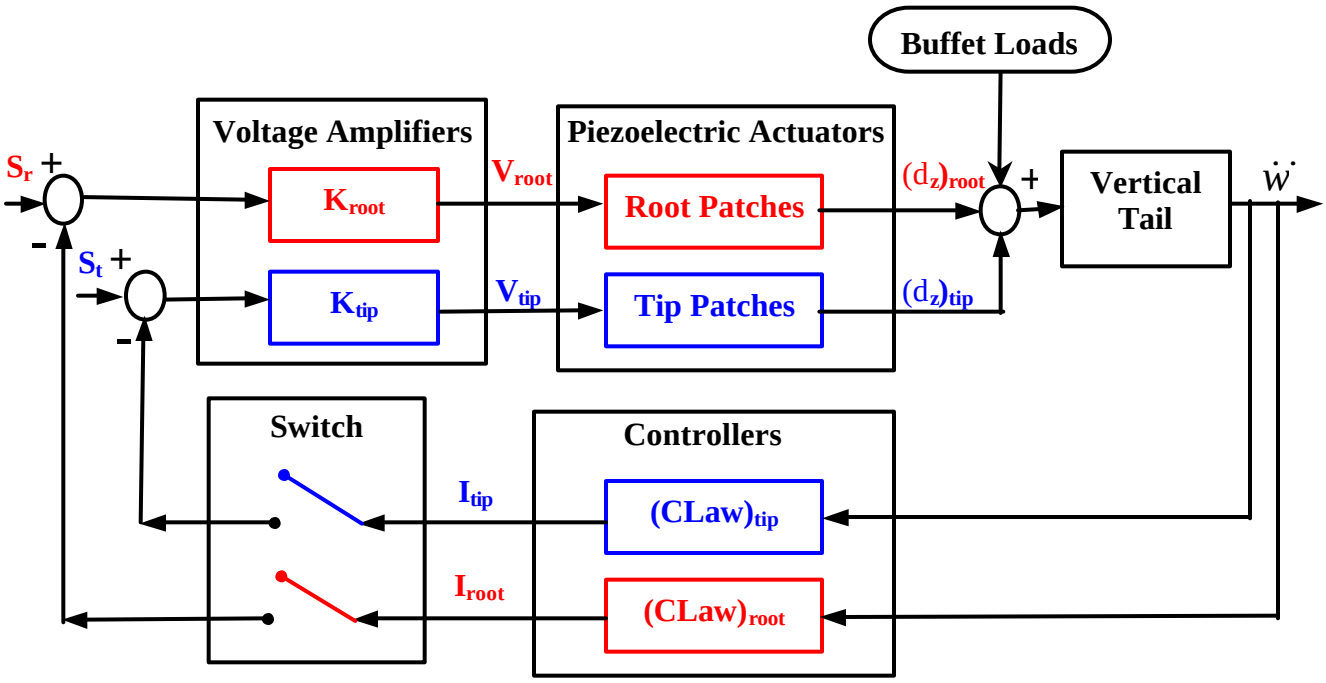

Figure 50. Active Control System Diagram for the Tail Buffet Alleviation

The measured acceleration of the vertical tail is fed through the controller into two control laws, $(CLaw)_{tip}$ and $(CLaw)_{root}$ of the tip and root PZT patches, respectively. Each of the control laws has different control law gain, which is used to set the peak magnitude of the control law to unity. A switch is used to close or open the control loop of either the tip or the root control law.

The output of the controllers, I_{tip} and I_{root}, is sent to a summing junction where it may be combined with other signals for system identification. The signal is then sent into voltage amplifiers with gains of K_{tip} and K_{root}. The voltage amplifiers are used to increase the magnitude of the voltage signal, which is used to drive the PZT actuators. The signal of the PZT actuators is fed back into the vertical tail with the other input signal of the aerodynamics buffet loads.

System identification of the vertical tail with the PZT patches is conducted in order to design a suitable control law for the F/A-18 tails. The frequency responses of the tail tip accelerations due to voltage command of the PZT actuators at zero airspeed are shown in Figure 51. The acceleration peak in Figure 51a is at the first bending mode around 44 Hz. The first acceleration peak in Figure 51b is at the first torsion mode around 134 Hz, and the second peak is at the second bending mode around 157 Hz. Figure 51 shows that the root PZT actuators alone are capable of producing about 28 g's of response in the first bending mode per 1000 volts of excitation. The tip PZT actuators alone are capable of producing about 55 g's of response in the first torsion mode per unit 1000 volts of excitation.

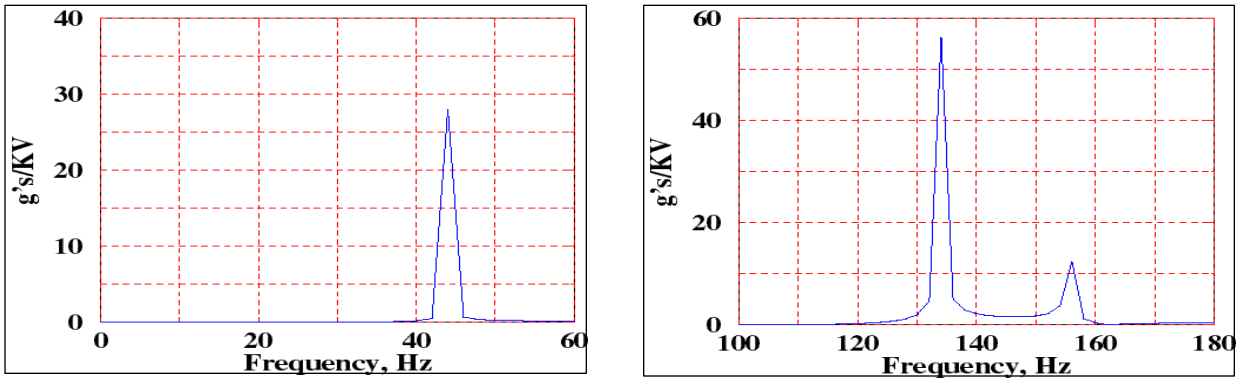

(a) First bending mode (b) First torsion mode

Figure 51. Frequency Response of the Tip Accelerations with Respect to Command Voltages of the Root and Tip PZT Actuators, Zero Air Speed, Open Loop

Using the frequency response results of Figure 51, two control laws were designed for the root and tip PZT actuators to control tail buffeting in the first bending and first torsion modes. Since these modes were well separated, single-input/single-output controllers were assumed enough. Low pass and band pass filtering are used in the root and tip control laws, respectively, so that the other modes are not excited when feedback is turned on as well as to concentrate the amplifier energy near the modal frequencies of interest (Moses et al. 2001).

The frequency response of the control laws are shown in Figures 52 and 53 for the root and tip PZT actuators, respectively. The peak magnitude of the control law is placed near the frequency of the first natural frequency of the tail. The peak value was purposely set to unity so that adjustments to the magnitude could be made via the gain block *K*. The phase of the control law near the first natural frequency is set to –90° to augment structural damping.

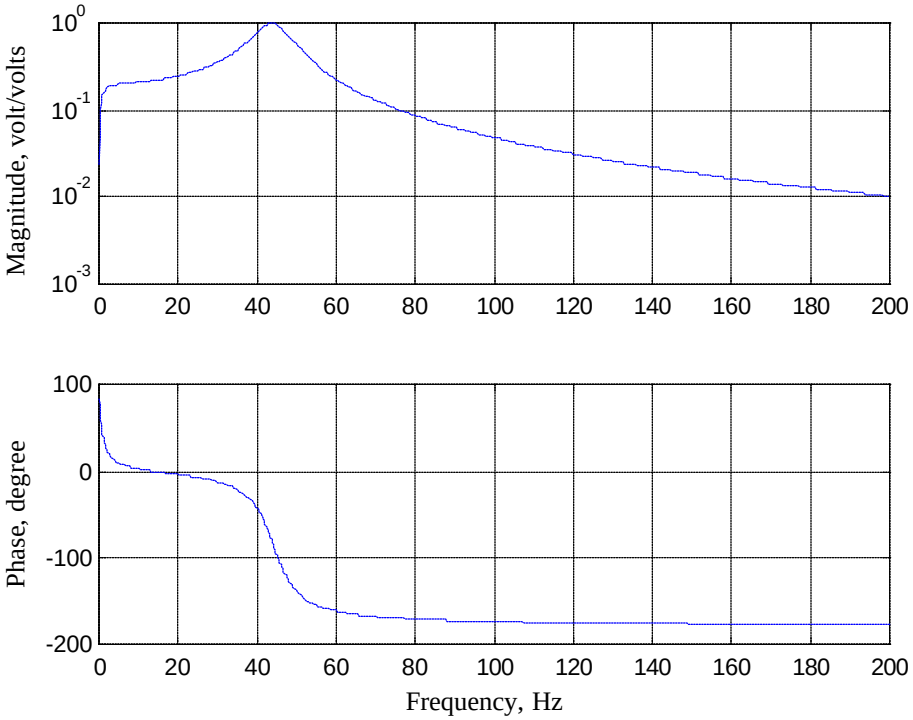

Figure 52. The Frequency Response of the Control Law for the Root PZT Actuators

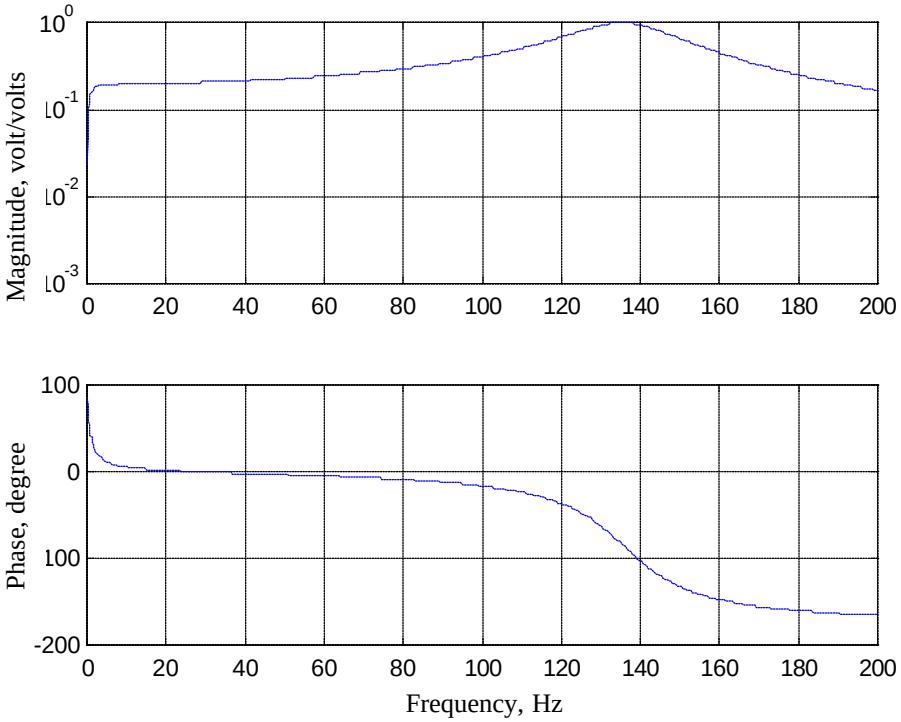

Figure 53. The Frequency Response of the Control Law for the Tip PZT Actuators

7.5 Buffeting Alleviation

The effectiveness of the PZT actuators for buffet alleviation is investigated at 30^{o} angle of attack, which is corresponding to one of the maximum buffet conditions as seen in the previous sections. The PSD of tail tip acceleration near the first bending and first torsion modes are shown in Figure 54. The time histories of the input signal to the root piezoelectric actuators and to the tip piezoelectric actuators (in volts) are shown in Figure 55.

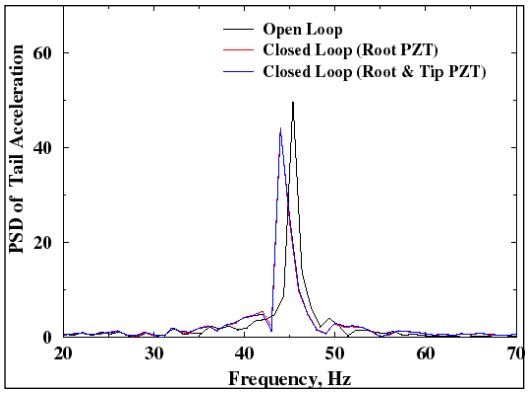

(a) Acceleration power at first bending mode

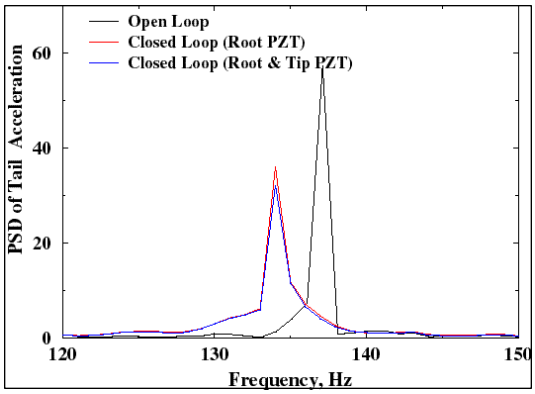

(b) Acceleration power at first torsion mode

Figure 54. PSD of Tip Acceleration for Open Loop and Closed Loop Controllers

When closed loop controller is used for the root PZT actuators only, the peak acceleration in the first bending mode is reduced by about 11 percent and the peak acceleration in the first torsion mode is reduced by about 37 percent. When closed loop controllers are used for both the root and tip PZT actuators, the peak acceleration in the first bending mode is reduced by about 12 percent and the peak acceleration in the first torsion mode is reduced by about 44 percent. The slight shift in the frequencies of the acceleration peaks is caused by the control law and can be eliminated by adjusting the phase of the control law at these regions of the spectra. The other aeroservoelastic model showing in Figure 49 produced the same results if the total area of the PZT patches is equivalent to the model presented in Figure 48.

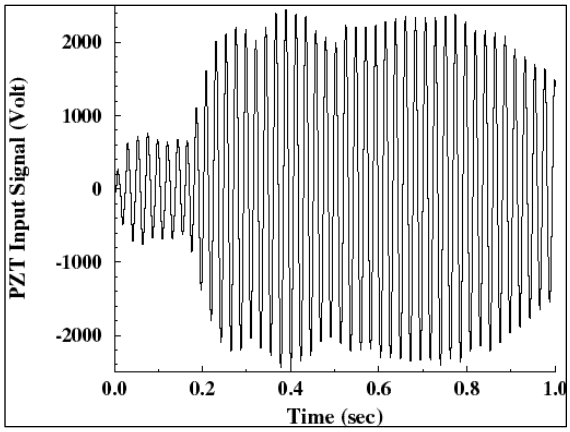

(a) Root PZT Actuators

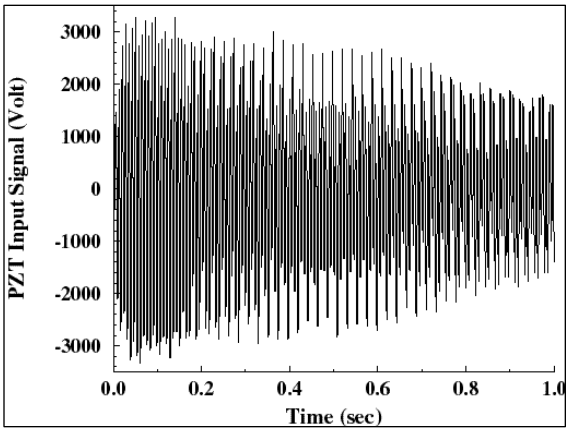

(b) Tip PZT Actuators

Figure 55. The Time Histories of the Input Signal to the PZT Actuators

The time histories of tail tip normal deflection of the vertical tail for the cases of open loop and closed loop controllers are shown in Figure 56. The closed loop controller slightly reduced the amplitude of the tip deflection.

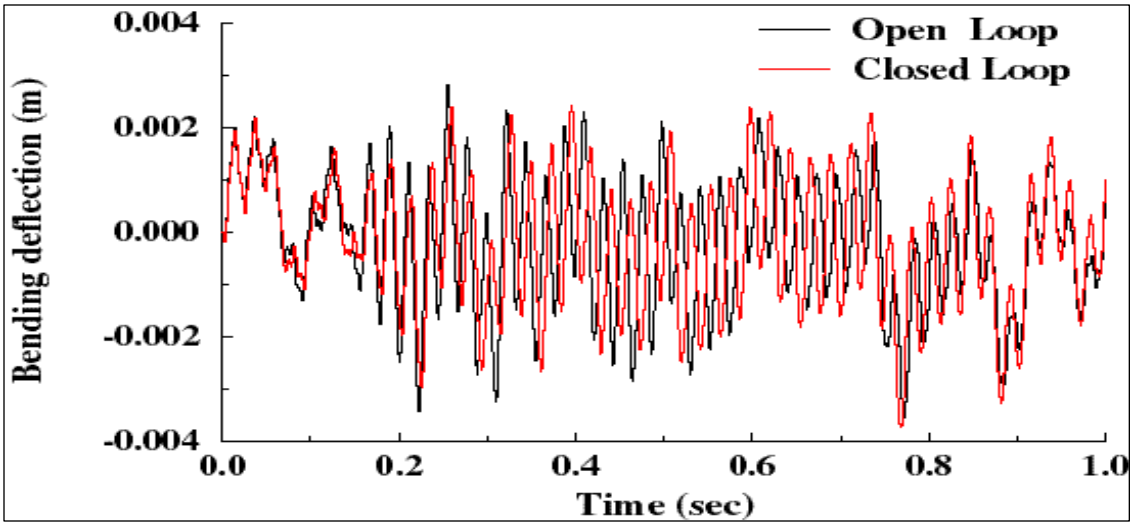

Figure 56. Tip Bending Deflection of the Vertical Tail

7.6 Conclusion

Multidisciplinary capabilities for active control of structures have been developed and integrated into MDICE environment. A multidisciplinary aeroservoelastic simulation of buffet alleviation of F/A-18 vertical tail using PZT actuators was successfully conducted and presented. Several sets of PZT actuators were strategically located over the inboard and outboard surfaces of the vertical tail to alleviate the tail buffeting in the first bending and torsion modes. The PZT actuators reduced the acceleration peaks by up to 12 percent in the first bending mode and up to 44 percent in the first torsion mode.

8. CONCLUDING REMARKS

A high-fidelity multidisciplinary analysis tool for the prediction and control of tail buffeting and related aeroelastic phenomena has been developed and extensively validated. The analysis tool has been used for the prediction and control of F/A-18 vertical tail buffeting. High-fidelity modules have been integrated into MDICE. The aerodynamic flow field around the F/A-18 aircraft is computed using the Reynolds-averaged full Navier-Stokes equations. The structure dynamics response of the vertical tail is predicted using direct finite-element analysis. The interface between the fluid and structure is applied using conservative/consistent interfacing methodology. The motion of the computational grid due to the deflection of the vertical tail is computed using transfinite interpolation module. Finite-element implementation of the electrodynamics of smart materials has been developed for the purpose of active strengthening of the flexible structures. Several control laws have been developed and integrated with MDICE and used for active structure control of tail buffeting. The developed environment represents a unique and effective way for aeroelastic and aeroservoelastic analysis of fighter aircraft. This project has successfully accomplished three main objectives:

- Development of high-fidelity multidisciplinary aeroelastic capability for the accurate prediction of twin-tail buffet of fighter aircraft.
- Development of analysis capabilities for the passive and active flow control methods for buffet alleviation.
- Development of analysis capabilities for the active structure control for buffet alleviation.

The specific accomplishments and conclusions of this study along with recommendations for future research work are discussed below.

8.1 Accomplishments and Conclusions

- ***Development of a Unique High-Fidelity Multidisciplinary Analysis Capabilities***
  A state-of-the-art high fidelity multidisciplinary analysis capability has been successfully developed. The analysis capability may be used for early prediction of aeroelastic problems, such as tail buffeting, of fighter aircraft before the actual design stage. This in turn could save millions of dollars every year for inspections, repairs, and premature replacement.

- ***Prediction and Validation of F/A-18 Vertical Tail Buffeting***
  The vertical tail buffeting of the F/A-18 aircraft has been predicted and validated over a wide range of typical flight conditions. The computed results agree well with several flight and experimental data. The results indicated that the inboard surface of the vertical tail has more significant contribution in the unsteadiness of the problem than the outboard surface. The outboard surface pressure of the vertical tail is less sensitive to the angle of attack than the pressure on the inboard surface. The buffet excitation peaks shift to lower frequencies as the angle of attack increases. The vertical tail of the F/A-18 aircraft is responding mainly in the first bending and torsional modes. The vertical tail is oscillating mainly toward the outboard direction. The computational results were compared and they are in close agreement with flight and experimental data over the angle of attack range.

- ***Control Vertical Tail Buffeting using Vortical Blowing***
  A high-momentum fluid is injected from the top of the wing LEX into the vortical flow of the aircraft. The vortical blowing moved the cores of the LEX vortices toward the inboard direction, which balanced the unsteady pressure on both sides of the vertical tail. This balance resulted in much lower buffet excitation than the no-blowing case. In the range of the blowing strength considered in this investigation, the vortical blowing reduced the RMS of the unsteady differential pressure by up to 24 percent, and reduced the RMS of the root bending moment by up to 13 percent. The PSD of the root bending moment was also reduced by up to 23 percent. The response of the vertical tail was dominated by the first bending mode. The vortical blowing increases the acceleration power at the first bending and torsion modes. However, it reduces the acceleration power at the second bending mode.

- ***Control Vertical Tail Buffeting Using LEX Fences***
  Streamwise fences were placed over the LEX of the wing at strategic places as to disperse the energy of the vortical flow before reaching the vertical tail. The results show that the LEX fences are effective in reducing the RMS of differential pressure and root bending moment of the vertical tail. The LEX fence shifted the power peak of the buffet pressure into a higher angle of attack, preserving the main essence of the LEX fence. The LEX fences were also effective in reducing the amplitude of deflections of the vertical tail.

- ***Active Structure Control of the Vertical Tail Buffeting***
  Active structure control of the vertical tail buffeting has been achieved using stacks of PZT actuators. The PZT patches were distributed over the inboard and outboard surfaces of the vertical tail to increase control authority in the first bending and torsion modes. The PZT actuators reduced the acceleration peaks by up to 12 percent in the first bending mode and up to 44 percent in the first torsion mode.

8.2 Lesson Learned

The mutual interaction between the fluid and structure in the tail buffet phenomenon is very strong. Engineers cannot afford to neglect this time-dependent interaction or simplify it using one-way interaction. The time-dependent interaction is being ignored when engineers decide to solve for the aerodynamics flow field separately to obtain time-dependent histories of loads. The loads are then used to obtain time history of structural responses. The inertial effects of the structural flexibility is being ignored when the deformed shape of the tail is not fed back into the flow field every time step. In this case, the fluid dynamics solver solves for the flow field around the configuration assuming the flexible surface is in its original location, which is not true since the flexible surface has moved into different location every time step affecting the whole flow field. This case exists even if the boundary conditions of the flexible bodies are modified to account for the velocity and acceleration of the deformed surfaces. The inertial effects will still be ignored since the flow field will not feel the inertial motion of the structure. Neglecting the time-dependent interaction between the fluid and structure will reduce the accuracy of the buffet analysis. For example, compare the accuracy of the results of Rizk et al. (1992), where the inertial effects have been ignored, to the results of this study. Neglecting the inertial effects in Rizk et al. (1992) simulations has reduced the accuracy of their results.

8.3 Recommendations for Future Research

The work of this project resulted in a reliable and viable analysis tool for the prediction and control of tail buffeting and related aeroelastic phenomena of fighter aircraft. The following recommendations are suggested for future research:

- ***Buffet Prediction of High-Performance Fighters***

  - Prediction of buffet of high-performance aircraft (e.g., JSF, F22, F15, etc.).
  - Characteristics of buffet over a wide range of high angles of attack.
  - Predict the effects of different structural models of the vertical tail (reflecting hardware configurations, materials, etc) on the buffet problem.

- ***Active Structure Control***
  Finite-element modeling of the piezoelectric actuators has been developed and tightly coupled with the finite element module of the tail structure. This computational capability needs to be generalized for generic configurations and demonstrated on specific problems of interest (e.g., JSF, F22, etc.). There are several issues which need to be further investigated:

  - Arbitrary interfaces between the PZT patches and the tail structure.
  - Optimum locations of the PZT patches.
  - Size and quantity of the PZT patches.
  - Orientations of the PZT patches.
  - Optimum control law for buffet alleviation.
  - Simulation of the effectiveness of new PZT materials for buffet alleviation.

- ***Active Rudder Control***
  Experimental tests have shown that the F18 vertical tail rudder may be used to control the vertical tail buffet in the first bending mode. The use of active rudder may reduce the weight of the vertical tail by eliminating the weight of the PZT patches. The current capability can be used to investigate the following:

  - Optimum control law for active rudder.
  - Size and dimensions of the active rudder (the whole rudder may or may not be used).
  - Characteristic limits of active rudder frequencies and amplitudes.

  A successful demonstration may produce a more optimal design before wind tunnel and flight tests take place and will reduce design cycle time and cost.

- ***Prediction of Buffet During Dynamic Maneuvers***
  With the advent of aircraft equipped with thrust vectoring and advanced flight control systems, poststall departure can now be effectively controlled, making aggressive maneuvering at elevated angle of attack a reality. The dynamic maneuvers could include dynamic pitching-up motion from 0° up to 90° in a very short period of time, dynamic rolling motion, and coupled pitching-rolling-yawing dynamic motions. The next generation of combat aircraft, such as the Joint Strike Fighter (JSF) will be required to fly different

complex types of maneuvers routinely. Thus, it is imperative that the designers of the new generation of combat aircraft have the ability to model the highly complex flow physics of high angle of attack and complex fluid-structure interaction at these angles. This is of prime importance to ensure the safety of the aircraft and pilot during these rigorous dynamic maneuvers.

8.4 Publications

During the course of this project, several journal articles and refereed papers were presented and published. The list of relevant publications is given below.

8.4.1 Journal Articles

1. Sheta, E. F., Harrand, V. J., and Huttsell, L. J., "Active Vortical Flow Control for Alleviation of Twin-Tail Buffet of Generic Fighter Aircraft," *Journal of Fluids and Structures*, Academic Press, Vol. 15, No. 6, August 2001, pp. 769-789.
2. Sheta, E. F. and Huttsell, L. J., "Characteristics of F/A-18 Vertical Tail Buffeting," *Journal of Fluids and Structures*, Academic Press, Accepted for Publications, June 2002.
3. Sheta, E. F., "A Multidisciplinary Analysis of Tail Buffeting Alleviation using Streamwise Fences," *Journal of Vibration and Control*, Accepted for publications, March 2002.

8.4.2 Refereed Papers

1. Sheta, E. F. and Huttsell, L. J., "Control of F/A-18 Vertical Tail Buffeting by Vortical Blowing," AIAA 2002-0948, 40th AIAA Aerospace Sciences Meeting and Exhibit, Reno, NV, January 14-17, 2002.
2. Sheta, E. F. and Huttsell, L. J., "Numerical Analysis of F/A-18 Vertical Tail Buffeting," AIAA 2001-1664, 42nd AIAA/ASME/ASCE/AHS/ASC Structures, Structural Dynamics and Materials Conference, Seattle, WA, April 2-5, 2001.
3. Sheta, E. F., Stacey, S. G., and Huttsell, L. J., "Characteristics of vertical tail buffet of F/A-18 aircraft," AIAA 2001-0710, 39th AIAA Aerospace Sciences Meeting and Exhibit, Reno, NV, January 8-11, 2001.
4. Sheta, E. F., "Control of Twin-Tail Buffet Responses using Normal Leading-Edge Blowing," AIAA 2000-4227, 18th AIAA Applied Aerodynamic Conference, Denver, CO, August 14-17, 2000.
5. Sheta, E. F., "Effect of Stream-Wise Fences on Twin-Tail Buffet Responses," AIAA 2000-4410, 18th AIAA Applied Aerodynamic Conference, Denver, CO, August 14-17, 2000.
6. Sheta, E. F., Harrand, V. J., and Huttsell, L. J., "Active Vortical Flow Control for Alleviation of Twin-Tail Buffet of Generic Fighter Aircraft," AIAA-2000-0906, 38th AIAA Aerospace Sciences Meeting and Exhibit, Reno, NV, January 10-13, 2000.
7. Sheta, E. F., Siegel, J. M., Golos, F. N., and Harrand, V. J., "Twin-Tail Buffet Simulation Using a Multidisciplinary Computing Environment," NASA/CP-1999-209136, CEAS/ AIAA/ICASE/NASA Langley International Forum in Aeroelasticity and Structural Dynamics, Williamsburg, Virginia, June 22-25, 1999.

9. REFERENCES

Anglin, E. L. and Satran, D., "Effects of Spanwise Blowing on Two Fighter Airplane Configurations," *Journal of Aircraft*, Vol. 17, pp. 883-889, 1980.

Bean, D. E. and Lee, B. H. K., "Correlation of Wind Tunnel and Flight Test Data for F/A-18 Vertical Tail Buffet," *AIAA Paper* 94-1400, 1994.

Brown, S. A., "Displacement Extrapolation for CFD and CSM Analysis," *AIAA Paper* 97-1090, 1997.

CFD Research Corporation, "CFD-ACE+ User Manual," CFDRC, Version 2.2, 1998.

Cole, S. R., Moss, S. W., and Dogget, R. V., Jr., "Some Buffet Response Characteristics of a Twin-Vertical-Tail Configuration," *NASA TM*-102749, 1990.

Fisher, D. F., Del Frate, J. H., and Richwine, D., "In-Flight Flow Visualization Characteristics of the NASA F-18 High Alpha Research Vehicle at High Angles of Attack," *NASA TM* 4193, 1990.

Gee, K., Murman, S., and Schiff, L., "Computational Analysis of F/A-18 Tail Buffet," *AIAA Paper* 95-3440-CP, 1995.

Gursul, I. and Xie W., "Buffeting Flows over Delta Wings," *AIAA Journal*, Vol. 37, pp. 58-65, 1999.

Hall, L. H., "Navier-Stokes/6-DOF Analysis of the JDAM Store Separation from the F/A-18C Aircraft," *AIAA Paper* 99-0121, 1999.

Harrand, V. J., Parthasarathy, V., Sheta E. F., Warren, C. W., and Underwood, M. L., "Development and Validation of Parallel Distributed Computing Environment For Aerostructural CFD Analysis," Final Report, Contract No. F33615-96-C-3002, Air Force Research Laboratory, Dayton, OH, 1999.

Hauch, R., Jacobs, J., Ravindra, K., and Dima, C., "Reduction of Vertical Tail Buffet Response Using Active Control," AIAA CP 95-1080, 1995.

James, K. D. and Meyn, L. A., "Dependence of Integrated Vertical-Tail Buffet Loads for F/A-18 on Sensor Density," *SAE Paper* 941140, 1994.

Jumper, E. J., Nelson, R. C., and Cheung, K., "A simple Criterion for vortex breakdown," *AIAA Paper* 93-0866, 1993.

Kandil, O. A., Massey, S. J., and Sheta, E. F., "Aerostructural Vortical Flow Interactions With Applications to F/A-18 and F-117 Tail Buffet," *NASA-CR*-203245, 1996. Also in *NASA/CP*-1998-207676, pp. 1375-1388, 1998.

Kandil, O. A., Sheta, E. F., and Massey, S. J., "Fluid/Structure Twin Tail Buffet Response Over A Wide Range of Angles of Attack," *AIAA Paper* 97-2261-CP, 1997.

Kingsley, G. M., Siegel, J. M., Harrand, V. J., Lawrence, C., and Luker, J., "Development of the Multi-Disciplinary Computing Environment (MDICE)," *AIAA Paper* 98-4738, 1998.

Lee, B. and Brown, D., "Wind Tunnel Studies of F/A-18 Tail Buffet," *AIAA Paper* 90-1432, 1990.

Lee, B., Brown, D., Zgela, M., and Poirel, D., "Wind Tunnel Investigation and Flight tests of Tail Buffet on the CF-18 Aircraft," *AGARD CP No.* 483, 1990.

Lee, B. and Valerio, N., "Vortical Flow Structure near the F/A-18 LEX at High Incidence," *Journal of Aircraft*. Vol. 31, pp. 1221-1223, 1994.

Meyn, L. A. and James, K. D., "Full Scale Wind Tunnel Studies of F/A-18 Tail Buffet," *AIAA Paper* 93-3519, 1993.

Meyn, L. A., James, K. D., and Green, R. J., "Correlation of F/A-18 Tail Buffet Results," High Alpha Projects and Technology Conference, Dryden Flight Research Center, July 1994.

Miller, L. S. and Gile, B. E., "Effects of Blowing on Delta Wing Vortices During Dynamic Pitching," *Journal of Aircraft*, Vol. 30, pp. 334-339, 1993.

Moses, R. W. and Pendleton, E., "A Comparison of Pressure Measurements Between a Full-Scale and a 1/6-Scale F/A-18 Twin Tail During Buffet," *NASA-TM*-110282, 1996.

Moses, R. W., "Vertical Tail Buffeting Alleviation Using Piezoelectric Actuators - Some Results of the Actively Controlled Response of Buffet-Affected Tails (ACROBAT) Program," *NASA TM* 110336, 1997.

Moses, R. W. and Huttsell, L. J., "Fin Buffeting Features of an Early F-22 Model," *AIAA Paper* 2000-1695, 2000.

Moses, R. W., Wiesman, C. D., Bent, A. A., and Pizzochero, A. E., "Evaluation of New Actuators in a Buffet Loads Environment," CEAS/AIAA/AIAE International Forum on Aeroelasticity and Structural Dynamics, Madrid, Spain, June 2001.

Rizk, Y., Guruswamy, G., and Gee, K., "Numerical Investigation of Tail Buffet on F-18 Aircraft," *AIAA Paper* 92-2673-CP, 1992a.

Rizk, Y., Guruswamy, G., and Gee, K., "Computational Study of F-18 Vortex Induced Tail Buffet," *AIAA Paper* 92-4699-CP, 1992b.

Pettit, C., Brown, D., and Pendleton, E., "Wind Tunnel Tests of Full-Scale F/A-18 Twin Tail Buffet: A Summary of Pressure and Response Measurements," *AIAA Paper* 94-3476, 1994.

Rao, D., Puram, C., and Shah, G., "Vortex Control for Tail Buffet Alleviation on a Twin-Tail Fighter Configuration," *Aerospace Technology Conference and Exposition*, Anaheim, CA, SAE Paper No. 892221, 1989.

Seginer, A. and Salomon, M., "Performance Augmentation of a 60-Degree Delta Aircraft Configuration by Spanwise Blowing," *Journal of Aircraft*, Vol. 23, pp. 801-807, 1986.

Sellers, W. L. III, Meyers, J. F., and Hepner, T. E., "LDV Survey Over a Fighter Model at Moderate to High Angle of Attack," *SAE Paper* 88-1448, 1988.

Shah, G.H., "Wind-Tunnel Investigation of Aerodynamic and Tail Buffet Characteristics of Leading-Edge Extension Modifications to the F/A-18," *AIAA Paper* 91-2889, 1991.

Sheta, E. F. and Kandil, O. A., "Effect of Configuration Pitching Motion on Twin-Tail Buffet Response," *AIAA Paper* 98-0520, 1998.

Sheta, E. F. and Kandil, O. A., "Effect of Dynamic Rolling Oscillations on Twin-Tail Buffet Response," *AIAA Paper* 99-0792, 1999.

Sheta, E. F., "Prediction and Control of Twin-Tail Buffet of Fighter Aircraft," AFRL-VA-WP-TR-2000-3011, Air Force Research Lab Technical Report, March 2000.

Sheta, E. F., "Effect of Stream-Wise Fences on Twin-Tail Buffet Responses," *AIAA Paper* 2000-4410, 2000.

Sheta, E. F., Harrand, V. J., and Huttsell, L. J., "Active Vortical Flow Control for Alleviation of Twin-Tail Buffet of Generic Fighter Aircraft," AIAA Paper 2000-0906, 38th SM, Reno, NV, 2000.

Sheta, E. F., Stacey, S. G., and Huttsell, L. J., "Characteristics of vertical tail buffet of F/A-18 aircraft," *AIAA Paper* 2001-0710, 2001.

Siegel, J. M., Jr., Parthasarathy, V., Kingsley, G. M., Dionne, P. J., Harrand, V. J., and Luker, J. J., "Application of A Multi-Disciplinary Computing Environment (MDICE) for Loosely Coupled Fluid-Structural Analysis," AIAA-98-4866, 7th AIAA/USAF/NASA/ISSMO Symposium of MDO, 1998.

Yang, H. Q. and Wang, Z. J., "Interaction of Shock Wave with a Flexible Structure," *AIAA Paper* 94-0362, 1994.

Washburn, A. E., Jenkins, L. N., and Ferman, M. A., “Experimental Investigation of Vortex-Fin Interaction,” *AIAA Paper* 93-0050, 1993.

Wentz, W. H., “Vortex-Fin Interaction on a Fighter Aircraft,” *AIAA Paper* 87-2474, 1987.